Università degli Studi di Trento

Facoltà di Scienze Matematiche Fisiche e Naturali

Dottorato di Ricerca in Fisica
XXIV Ciclo

Vibrational dynamics in strong glasses: the cases of densified v-SiO_2 and v-$SiSe_2$

Marco Zanatta

Tutore:

Prof. Aldo Fontana

2011

The whole universe is in a glass of wine.

R.P. Feynman

Contents

Introduction

Cumque compleveris legere librum istum,
ligabis ad eum lapidem
et proicies illum in medium Euphraten.
Liber Ieremiae, 51:61

Glasses are the most ancient materials created by Mankind. During the centuries the properties of glasses have been exploited for technological application, from the optical lens to the optic fibers up to the new generation of solid state memories by also including pharmaceutical and biological application. However, despite this widespread technological interest, the fundamental properties of glasses still have an enigmatic nature.

In this work we will face the problem of the vibrational properties of glasses focusing on the origin and nature of the boson peak (BP). This feature is an universal characteristic of glasses and a fingerprint of the presence of disorder. The boson peak appears in the vibrational density of states as an excess of modes over the Debye prediction. There are two main open questions about the boson peak: the first is the nature of the mode forming the peak; the second concerns the microscopic mechanisms originating this low frequency piling up.

Two samples have been chosen for this study. The first is permanently densified vitreous SiO_2. Permanent densification has been exploited to tune the glassy properties focusing on their evolution. Permanently densified vitreous silica has

been investigated by means of Raman and Brillouin light scattering as well as and inelastic X-ray scattering. On the other hand, the evolution of the structure has been monitored by looking to the diffraction pattern and by directly measuring the microscopic arrangement trough positron annihilation spectroscopy. The second sample is a silicon-selenium glass whose low sound velocity allows a detailed study of its dynamics by means of neutron inelastic scattering.

The first two chapters present a brief overview of the glassy state, reviewing its dynamical and structural properties and a basic outline of inelastic X-ray and neutron scattering theory. The third chapter is devoted to the study of the evolution of the boson peak in vitreous silica as a function of density, showing that its evolution cannot be explained only by means of the elastic medium transformation. The analysis on this sample is completed in the fourth chapter where positron lifetime spectroscopy data are presented and we detail a microscopic view of its structural evolution. In the fifth chapter a comparison between SiO− polycrystal and glass at the same density is presented. This strongly suggests an acoustic origin for the BP modes, highlighting the equivalence between boson peak in glasses and first Van Hove singularity in crystals. Finally, in the last chapter, we report on the neutron scattering study on the silicon-selenium glass $SiSe_2$. This system exhibits a crystal-like dynamics with evidence of the presence of two transverse acoustic excitations.

Acknowledgments

A. Fontana, S. Caponi, E. Moser, L. Orsingher, and F. Rossi

Dipartimento di Fisica, Università di Trento, CNR-IPCF UOS Roma, CNR-IOM Perugia

R.S. Brusa and S. Mariazzi

Dipartimento di Fisica, Università di Trento, CNISM and INFN

G. Baldi

Dipartimento di Fisica, Università di Parma and CNR-IMEM

C. Petrillo, and F. Sacchetti

Dipartimento di Fisica, Università di Perugia and CNR-IOM

G. Ruocco

Dipartimento di Fisica, Università di Roma "Sapienza"

C. Crupi, G. Carini, G. D'Angelo, and G. Tripodo

Dipartimento di Fisica, Università di Messina and CNR-IPCF Messina

C. Masciovecchio

ELETTRA, Trieste

M. Krisch, E. Borissenko, G. Monaco, B. Ruta, and R. Verbeni

European Synchrotron Radiation Facility, Grenoble

A. De Francesco, A. Laloni

Institut Laue Langevin and CNR-IOM, Grenoble

C. Hugenschmidt,G.G. Simeoni, and T. Unruh

Forschungs-Neutronenquelle Heinz Maier-Leibnitz (FRM II), Technische Universität München, München

W. Egger and L. Ravelli

Institut für Angewandte Physik und Messtechnik, Universität der Bundeswehr, München

E. Gilioli and C. Corradi

CNR-IMEM Parma and Trento

C. Armellini

Fondazione Bruno Kessler, Trento

R. Dal Maschio

Dipartimento di Ingegneria dei Materiali, Università di Trento

Chapter 1

The glassy state

The deepest and most interesting unsolved problem in solid state theory
is probably the theory of the nature of glass and the glass transition.
Whether it will help make better glass is questionable.
P.W. Anderson

The glassy state represents an intermediate state between liquids and crystals. Its structure is characteristic of the instantaneous structure of a liquid, isotropic and lacking of long range order. However, atoms are constrained to vibrate around their disordered equilibrium position, so that their dynamics is characteristic of a solid.

The glassy state is accessed by both Nature and Mankind through many routes [1, 2]. The most common and conventional process is the steady cooling of a liquid. The glass is obtained when the cooling liquid passes through the *glass transition*, which is actually a temperature region over which the system falls out of equilibrium, becoming a solid without crystallization, hence a glass.

1.1 Supercooled liquids and the glass transition

By cooling down a liquid below its melting point two phenomena may occur. The first process is the crystallization, which takes place at the melting temperature T_m. The crystal is formed through a process of nucleation and growth, where atoms or molecules rearrange to form a long range periodic structure [3]. The occurrence of this solid phase can be checked by looking at the temperature dependence of extensive thermodynamic variables such as volume and entropy. Figure 1.1 schematically shows the volume during cooling. In this plot, the crystallization process is represented as an abrupt drop of the volume occurring at T_m, which marks a first order phase transition.

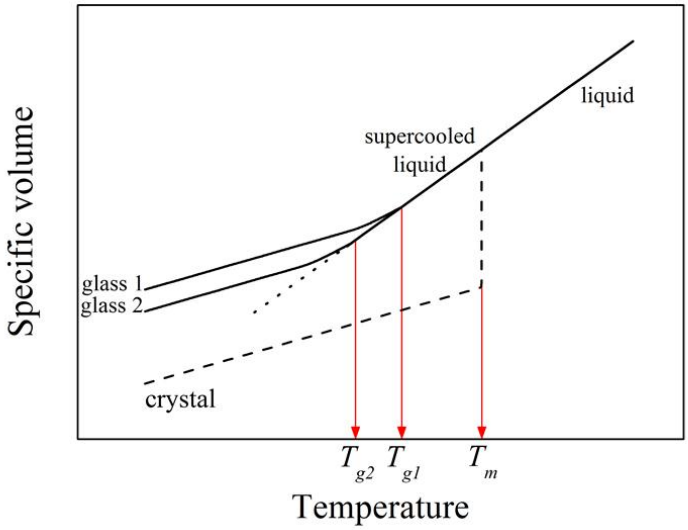

Figure 1.1: Schematic illustration of the change in volume with decreasing temperature in the case of crystallization and vitrification. The liquid-crystal transition temperature T_m is marked by an abrupt contraction of the volume. Conversely, in the glass formation process, $V(T)$ bends to a smaller slope. The region where the slope change takes place indicates the glass transition temperature T_g.

However, if the cooling rate is fast enough, the crystallization can be avoided and the liquid can be supercooled below T_m. By lowering the temperature,

the shear viscosity increases of many orders of magnitude, from a typical high temperature liquid value of about 10^{-4} poise to about 10^{13}. This increase is shown for many liquids in figure 1.2. The Maxweel relation $\eta = G_\infty \tau$, establishes a relation between the macroscopic viscosity and the microscopic relaxation time through G_∞, the infinite frequency shear modulus. Since G_∞ is almost constant, this means that the relaxation time is increasing. The supercooled liquid equilibrates through atomic and molecular rearrangements; when τ is increased they became slower and slower until the supercooled liquid is unable to equilibrate on the experimental timescale. The system falls out of equilibrium and the glass transition takes place.

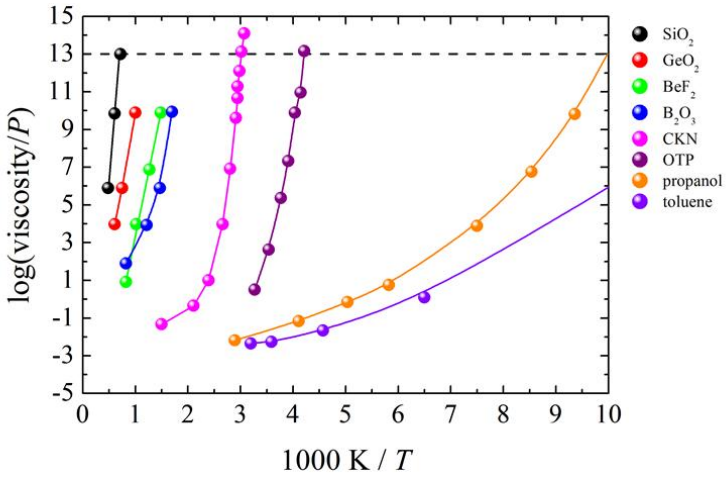

Figure 1.2: Variations of the viscosity η with temperature, plotted in Arrhenius form. The black dashed line represents $\eta = 10^{13}$ poise, conventional viscosity for a solid. Data are from ref. [1].

The structure of the system is frozen in the laboratory timescale and, except for thermal vibrations, all atomic motions cease. The glass transition is represented in figure 1.1 as a continuous break in slope of $V(T)$. The slope is the thermal expansion coefficient α: at the glass transition it changes from a liquid-like value to a crystal-like one.

The glass transition temperature T_g lyes at about $2/3T_m$ [4] and can be defined in many different ways, *e.g.* as the temperature at which $\tau \sim 10^3$ s [5, 3] or $\eta \sim 10^{13}$ poise [6, 1, 2]. In fact the glass transition takes place over a temperature region called transformation range. Moreover the glass transition temperature depends on the thermal history and on the cooling rate. The slower the cooling rate is and the lower the glass transition temperature is; examples of this glass transition cooling rate dependence are T_{g1} and T_{g2} in figure 1.1. Typically, the dependence of T_g upon cooling rate is relatively weak; an order of magnitude change in cooling rate may change T_g by only 3-5 K. Notwithstanding its dependence on cooling rate, Tg is an important material property.

The behavior shown by $V(T)$ is common to other extensive thermodynamic observables, like entropy and enthalpy. It suggests that the glass transition can be interpreted as a second order phase transition in the Ehrenfest sense [7], with continuity of volume and entropy but discontinuous changes of their derivatives. However the transition is continuous and cooling-rate dependent, so it cannot be a genuine phase transition. In fact, the glass transition is a kinetic process which depends upon the crossing of an experimental time scale and the time scales for molecular rearrangements [8].

In crystals the motion of the particles consists of vibrations around their ordered equilibrium position. The system is confined to one absolute minimum in the phase space. The same description seems to apply to a glass. Atoms vibrate around their disordered equilibrium position and the system is confined to a local energy minimum in the phase space. In both crystals and glasses ergodicity is broken but in glasses this is a dynamical phenomenon only due to the experimental time scale [3]. A glass can be considered as a liquid which behaves like a solid, since it continuously approaches the liquid state. As a consequence, the glass properties are time-dependent. This process is called aging when it is unwanted and annealing when it is used to remove stresses and

control the properties of the material [7].

1.2 Dynamics as T_g is approached: strong and fragile glassformers

By defining the glass transition temperature as the temperature at which $\eta = 10^{13}$ poise, data in figure 1.2 can be reported in the so called Angell plot, figure 1.3 [1, 2]. This Arrhenius representation of the viscosity as a function of a scaled temperature T_g/T highlights two different behaviors. As a matter of fact a first class of glassformers displays an Arrhenius behavior, *i.e.* a straight line in figure 1.3. Conversely, a second class is characterized by a a quite pronounced curvature at around $T_g/T \simeq 0.7$.

In order to classify different glassformers according their viscosity T-behavior we introduce the so-called fragility parameter, defined as [1]

$$m = \lim_{T \to T_g} \frac{d \log \eta}{d T_g/T}. \tag{1.1}$$

Low m glassformers present the Arrhenius behavior, and are called *strong*. On the other hand, *fragile* glassformers show high values of m, which means non-Arrhenius behavior.

The terminology strong and fragile is not related to the mechanical properties of the glass; this terms have been chosen to describe the sensitivity to the liquid structure to a change in temperature [1]. Moreover the fragility parameter m can be related to the microscopic interactions driving the dynamics of the system [9]. Strong liquids are characterized by covalent directional bonds and they typically form three dimensional network structures. Prototype of this class of materials is SiO_2, $m = 28$ [10]. On the other hand, fragile liquids typically consist of molecules interacting through non-directional, non-covalent bonding. The canonical fragile glassformer is the *o*-terphenyl OTP, $m = 81$ [10].

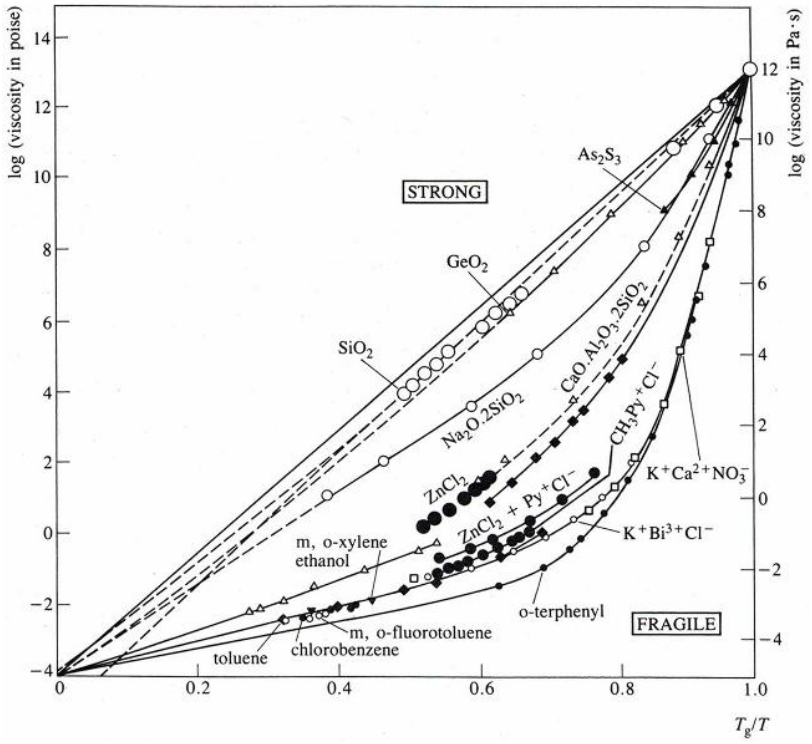

Figure 1.3: T_g scaled Arrhenius plots of the viscosity data showing the strong/fragile pattern of the liquid behavior. Adapted from ref. [1].

1.3 Glass structure

The determination of the atomic arrangement in space represents a key prerequisite for any subsequent study devoted to understand any physical and chemical properties. A striking example are proteins, where their functionalities are closely related to structural properties.

In crystals the determination of the structure is simplified by the periodicity. The whole lattice can be considered as a periodic repetition of a fundamental building block, the unit cell, which is often formed by only few atoms.

In glasses the situation is completely different. At the glass transition, except for vibrations, atoms are frozen in their instantaneous positions. The glassy structure is thus the supercooled liquid frozen structure, which is topological

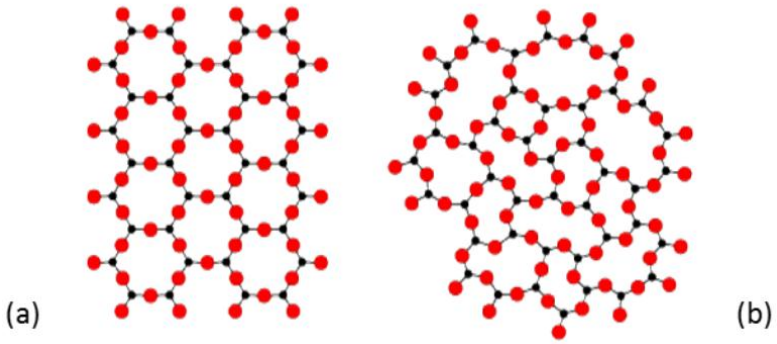

Figure 1.4: Bi-dimensional sketch of the structure of both crystalline α-quartz (a) and vitreous (b) SiO_2. Red dots are oxygen atoms while black dots refer to silicon ones, [11].

disordered, *i.e.* lacking of any long range periodicity. However, the glassy structure, even if disordered is far from being stochastic. As a matter of fact, also amorphous materials show a certain degree of order at some lengthscales. An example is SiO_2 as reported in figure 1.4. Both α-quartz (a) and vitreous silica (b) show the same coordination polyhedra, but in the glassy case they are arranged in an aperiodic fashion. The strength and the extension of the order in disordered materials are related to the different interactions, *e.g.* ionic and metallic glasses are more subject to a chemical and topological constrained random packing.

1.3.1 Order within disorder

To characterize the order in glassy structures it is useful to address to three different length scales [12]:

- short range order (SRO) in the range 2-5 Å;
- medium range order (MRO) in the range 5-20 Å;
- long range structures (LRS) for length scales > 20 Å.

Short range order involves one atom and its nearest neighbors. In the case of covalent materials, where direct bondings are dominant, SRO can be characterized in terms of well-defined coordination polyhedra. The SRO is often very similar to the local ordering in crystals: the number of nearest neighbors, the bond distances, and the bond angles are rather well defined.

MRO is pragmatically defined as the next highest level of structural organization beyond SRO. It arises from orientational correlation beyond the nearest neighbor distances. On a length scale just beyond SRO, 5-10 Å, larger structural units can be formed aggregating basic polyhedra connected together to form regular rings or clusters. In a larger length scale, between 10 and 20 Å, a further level of MRO can be associated with the connection between these structural units. This order is related to a local dimensionality of covalently bounded amorphous network. Considering a local dimensionality which arises from the structural connection, $d = 3$ corresponds to structural isotropy; lower local dimensionalities correspond to layer-like structures ($d = 2$), chain-like structures ($d = 1$) or isolated clusters, whose dimensionality is 0. Refined structural analysis have recently pointed out on the existence in some network glasses of an extended range of order [13, 14]. The lengthscale of this chemical order is about 40 Å.

To complete this overview of the order in amorphous materials we consider the macroscopic length scale. By definition, no long range periodic structures are present: the LRS is therefore characterized by inhomogeneity and phase separation.

1.4 Characterizing amorphous structure

The structure of a glass can be studied by means of several techniques. Nutron or X-ray diffraction provides valuable information on the short range order as

well as on the medium range. The sought quantity in a diffraction experiment in glass or liquids is the static structure factor, namely:

$$S(Q) = 1 + 4\pi\rho \int_0^\infty dr r^2 \frac{\sin qr}{qr} \left[g(r) - 1 \right], \tag{1.2}$$

i.e. the Fourier transform of the pair distribution function $g(r)$. This quantity conveys the probability of finding a particle at a distance r from a certain tagged particle and it is defined as:

$$g(r) = \frac{1}{N} \frac{1}{4\pi r^2 \rho} \left\langle \sum_i^N \sum_{i \neq j}^N \delta(r - r_{ij}) \right\rangle, \tag{1.3}$$

where N is the total number of particles, ρ is the density and $r_{ij} = \|\mathbf{r}_i - \mathbf{r}_j\|$. The analysis of the pair distribution function provides information on the short range order. For small r the radial distribution function is zero since the electron shells of two atoms cannot overlap strongly. On the other hand, nearest neighbors are expected at a certain distance r_{min}, producing a peak in $g(r)$. Due to the disorder atoms are not exactly at a distance r, hence the peak width will be finite. Further coordination shells can be distinguished depending on the system, but ultimately $g(r \to \infty) \to 1$.

A typical diffraction pattern for a glass is reported in figure 1.5(a) in the case of v-GeO_2. Figure 1.5(b) shows the diffraction spectrum of the liquid v-GeO_2. The two spectra look very similar: liquids and glasses retain almost the same structural properties [3]: from this point of view the glass transition is completely unexciting (at least using two points correlation functions [16]).

The first peak in the static structure factor is called first sharp diffraction peak (FSDP) and it is considered as the fingerprint of the presence of medium range order. As a matter of fact, even if every diffraction pattern has a first peak, this feature is rather peculiar [12, 17]. Firstly it is considerable narrower than the other peaks and it displays a different behavior as a function of both temperature and pressure [18]. There is, in general, no apparent difference in the

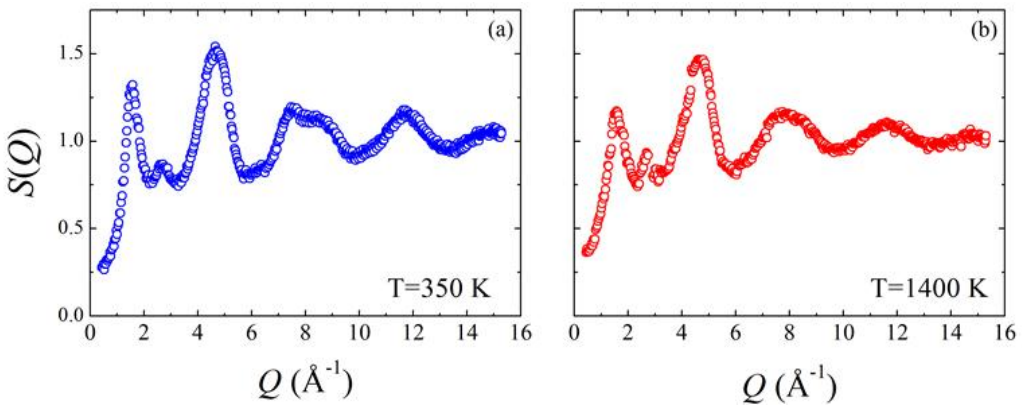

Figure 1.5: Static structure factor of glassy (a) and liquid (b) GeO_2 measured by means of neutron diffraction respectively at $T = 350$ K and $T = 1400$ K. The pattern of the glass is from [15], the liquid one is unpublished.

radial distribution function (RDF) obtained by Fourier transformation of the scattering data whether or not the FSDP is included in the Fourier transform, indicating that the peak results from rather subtle medium-range correlations which are not easily discernible in the $g(r)$ [12]. Many models have been proposed to explain this feature from the existence of crystallites [19], of cages [17, 20], and voids-clusters chemical ordering [21, 18].

Other techniques to characterize the structure of disordered systems are the Extended X-ray Absorption Fine Structure (EXAFS), which provides information on the environment of a specific atom, and the Nuclear Magnetic Resonance (NMR), which is also element selective and studies the correlations between an element and its neighbors. Also Raman scattering can give insights on the structure of the materials trough the identification of the vibrational bands. Moreover, in this work we will use the Positron Annihilation Lifetime Spectroscopy (PALS) as a probe for the medium range order, studying the interstitial voids in the material through the annihilation of the positronium.

1.5 Glass dynamics

Atoms in solids execute small oscillations around their equilibrium positions at every temperature, both at the absolute zero, as a result of zero-point motion, and at finite temperatures, as a result of thermal fluctuations. Below the glass transition temperature, *i.e.* in the arrested phase, the glass dynamics is restricted to these microscopic vibrations which are responsible for the sound propagation and the heat transfer and other thermodynamic quantities in solids.

1.6 Vibrations in solids

The theory of the dynamical properties of a solid can be treated by recurring to two approximations. The first is the adiabatic approximation which allows to separate the electronic dynamics from the corresponding nuclear one. The second is the so-called harmonic approximation which is based on the hypothesis of small nuclear oscillations around the equilibrium positions [22].

The vibrational dynamics of a system of N atoms in positions $\{\mathbf{r}\}$ is usually described in adiabatic approximation by an Hamiltonian of the form:

$$H = \frac{1}{2}\sum_{\alpha i} m_i \dot{r}_{\alpha i}^2 + V\left(\mathbf{r}_1, \ldots, \mathbf{r}_N\right), \tag{1.4}$$

where α indicates a Cartesian coordinate, m_i is the mass of the ith-atom, and $V\left(\mathbf{r}_1, \ldots, \mathbf{r}_N\right)$ is the N-body potential which describes interactions of all atoms in the solid. The atomic motions is a small displacement $\mathbf{u}$ about an equilibrium position $\mathbf{r}^0$, hence $\mathbf{r}_i = \mathbf{r}_i^0 + \mathbf{u}_i$. The use of the harmonic approximation can simplify the problem. As a matter of fact V can be expanded in series of u's until the first non-vanishing term, which is the quadratic ones. Therefore we

can write the equations of motion of the system:

$$\begin{aligned} m_i \ddot{u}_{\alpha i} &= -\sum_{\beta j} \left. \frac{\partial^2 V}{\partial u_{\alpha i} \partial u_{\beta j}} \right|_0 u_{\beta j} \\ &= -\sum_{\beta j} \Phi_{\alpha i}^{\beta j} u_{\beta j}. \end{aligned} \tag{1.5}$$

Considering a solution of eq. 1.5 which is periodic in time [23], *i.e.* $u_{\alpha i}(t) = m_i e_{\alpha i} exp(i\omega t)$, where $e_{\alpha i}$ are time independent; eq. 1.5 may be written as:

$$\omega^2 e_{\alpha i} = \sum_{\beta j} D_{\alpha i}^{\beta j} e_{\beta j}. \tag{1.6}$$

The problem is thus reduced to an eigenvalue problems for the $3N \times 3N$ matrix $\mathbf{D}$, whose elements are:

$$D_{\alpha i}^{\beta j} = \frac{\Phi_{\alpha i}^{\beta j}}{\sqrt{m_i m_j}}; \tag{1.7}$$

$\mathbf{D}$ is called dynamical matrix and it has $3N$ real eigenvalues ω_k^2 and $\mathbf{e}_k$ are the $3N$-dimensional $3N$ eigenvectors.

1.6.1 Vibrations in crystals

In the case of a perfect crystal the situation is simplified using the lattice periodicity. The Bloch theorem allows to restrict the problem to a single unit cell of r atoms. Moreover the vibrational eigenvectors in a crystal will be plane waves, labeled by well-defined wave vectors $\mathbf{q}$ lying in the first Brillouin zone.

In a quantum mechanical description, the $3N$ decoupled collective vibrations of a crystal can be described in terms of bosonic quasi particles called *phonons*.

For each allowed $\mathbf{q}$ there are $3r$ real eigenvalues denoted as $\omega_k^2(\mathbf{q})$; the frequencies $\omega_k \mathbf{q}$ are either real for the stability of the lattice. These $3r$ functions for each $\mathbf{q}$. can be regarded as branches of a multivalued functions: the relation $\omega = \omega_k(\mathbf{q})$ is called dispersion relation. In general there are three branches for which $\omega_k(\mathbf{q})$ goes to zero which are called *acoustic* branches. The vibrations of

the atoms are in phase. There are one acoustic mode with longitudinal polarization and two with transverse one. Moreover, if $r > 1$, there are further $3(r-1)$ *optic* branches. These branches tend to a finite value as $\mathbf{q}$ approaches zero; if $\mathbf{q} = 0$ the basis atoms vibrate against each other.

It is worth to note that a theory of the atomic vibrations in harmonic approximation does not allow to predict the damping of the vibrational excitations which is due to higher order effects.

1.6.2 Vibrations in glasses

The simple approach outlined in the previous section cannot be extended to glasses where the periodicity is lost. As a matter of fact the reciprocal lattice cannot be defined and $\mathbf{q}$ is no longer a good quantum number. The eigenvectors of the dynamical matrix are no longer plane waves; finally, the concept of phonon loses its original meaning.

A wide variety of models have been proposed to describe the effects of the disorder in glasses. It has also been claimed that vibrational excitations with different nature can coexist in amorphous materials: propagating, localized and diffusive ones.

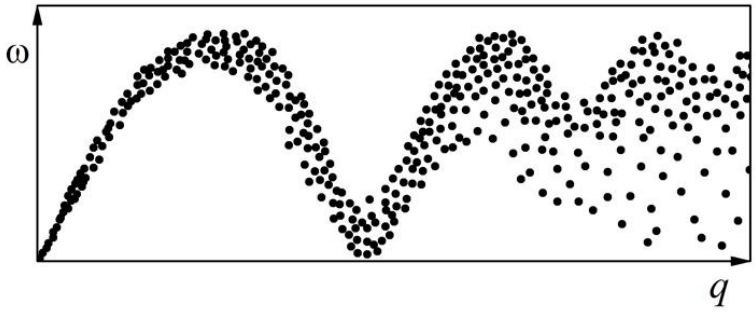

Figure 1.6: Schematic representation of the dispersion curve $\omega(q)$ of an acoustic branch in a glass, [24].

The common experience shows that in the macroscopic limit, sound propa-

gate also in a glasses as in corresponding crystals. In fact, averaging on a large scale, the details of the microscopic arrangement become essentially irrelevant.

At low frequencies, hence in the long wavelenght limit, a glass appears as an elastic continuum medium and the disorder does not affect the vibrational dynamics. As q approaches to zero, the vibrational excitations have the characteristic of linearly propagating acoustic waves, with speeds of sound v_L and v_T (the two transverse branch are degenerate because of the isotropy).

Increasing the frequency the lack of periodicity does not allow a plane waves description. However, acoustic phonon-like excitations can be detected up to a wavelenght comparable with the interparticle separation [25]. On decreasing further the wavelenght the atomic motions lose their propagating character giving rise to a more complex pattern of vibrations.

It has to be underlined that glassy modes in general are more damped than crystalline ones. Phonon damping arises from terms beyond the second order in the series expansion of V [26, 27]. The anharmonicity is in fact responsible for a direct interaction of sound waves with other thermal vibrations causing the damping through several mechanisms [28]. Moreover, also the disorder causes a phonon finite lifetime, since a plane wave cannot be an eigenstate of a system with a non periodic structure [29].

Figure 1.6 schematically shows the dispersion relation for an acoustic branch in glasses. Increasing the q value the excitation wavelength became shorter and the local structure is more and more relevant. The well-defined sound waves transform into a complex pattern of atomic motions that mirrors the structural disorder. Moreover, although the Brillouin zone is not rigorously defined, the dispersion relation shows a structure which can be related with the peaks of the static structure factor $S(Q)$ which are acting as smeared reciprocal lattice vectors.

1.7 The vibrational density of states

To describe the vibrational properties in crystals as well as in disordered systems we can use the vibrational density of states (VDOS), which is defined as:

$$g(\omega) = \sum_k \delta(\omega - \omega_k), \tag{1.8}$$

where $g(\omega)\, d\omega$ is the number of states lying between ω and $\omega + d\omega$.

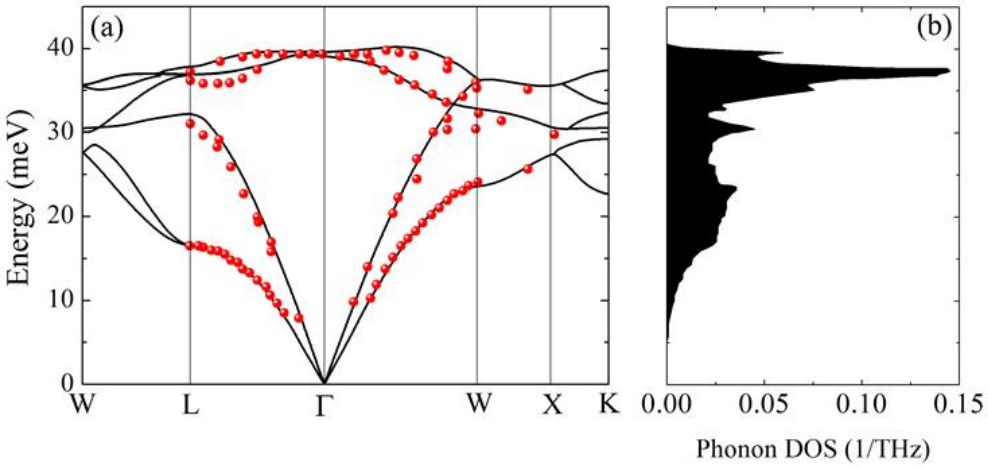

Figure 1.7: Phonon dispersion relation (a) and phonon density of states VDOS (b) of diamond. Solid curves show the calculated dispersions. Experimentally, dispersion relations over the Brillouin zone have been obtained by measurements such as neutron scattering, electron energy-loss spectroscopy, and x-ray scattering techniques. Data are from ref. [30].

For crystals the sum over $\mathbf{k}$ is over all branches and covers the first Brillouin zone. Figure 1.7 shows the relation between the dispersion relation and the DOS of a crystal. The peaks present in the DOS of a crystal are associated with the Van Hove singularities, the region where the dispersion curve is flat with $\partial\omega/\partial q = 0$.

In glasses, the index k in eq. 1.8 is only a label for the vibrational eigenstates. Moreover, the typical sharpness of the crystalline DOS disappears; Van Hove

singularities are smeared out as a consequence of the finite width of the energy distribution of vibrational excitation about a given q value.

The vibrational density of states represents the natural link between a microscopic description of a solids and its macroscopic properties. As a matter of fact, knowing the $g(\omega)$ we can derive thermodynamic properties such as the heat capacity C and the thermal conductivity κ [31].

1.7.1 The low frequency limit: the Debye model

In 1912 P. Debye proposed a quantum mechanical model to describe the low temperature specific heat of solids. In the low temperature limit thermally excited modes have an energy comparable with typical acoustic excitations and a wavelength greater than the interparticles distance. The solid can thus be treated as an elastic continuum in which acoustic waves can propagate. The vibrational excitations of the solid are described by the three acoustic branches with the same linear dispersion relation $\omega = v_D q$. The Debye velocity v_D is obtained averaging the longitudinal and transverse sound velocity, respectively v_L and v_T (in an isotropic medium the transverse branches are degenerate). The Debye velocity is defined as:

$$\frac{3}{v_D^3} = \left(\frac{1}{v_L^3} + \frac{2}{v_T^3} \right). \tag{1.9}$$

The total number of vibrational modes in the Debye model is $3N$, with N the number of atoms in the system. This constrain on the VDOS defines a limiting frequency ω_D which represents the highest frequency for the acoustic waves. The VDOS predicted by the model has the following form:

$$g(\omega) = \frac{3}{\omega_D^3}\omega^2. \tag{1.10}$$

The Debye frequency ω_D is defined as

$$\omega_D^3 = 6\pi^2 \rho_N v_D^3, \tag{1.11}$$

where ρ_N is the number density. Similarly to ω_D it can be defined a Debye wavevector $q_D = (2\pi\rho_N)^{1/3}$ which is maximum allowed wavevector for the acoustic modes and it corresponds to the typical inverse inter-particle distance of the system.

The description of the vibrational density of states allows a correct evaluation of the low temperature specific heat [32]:

$$c_v = \frac{12\pi^4}{5} N K_B \left(\frac{T}{\Theta_D}\right)^3, \tag{1.12}$$

where $\Theta_D = \hbar\omega_D/K_B$, and K_B the Boltzmann constant.

As already remarked, the Debye model holds rigorously for insulating crystalline material. However, since the local atomic arrangement is not considered, crystals and glasses can be both described within the same approximation. This would mean that if the temperature is lower than Θ_D, the temperature needed to excite all the acoustic modes, the thermodynamic properties are essentially the same. Unfortunately this is not the case [33].

Figure 1.8(a) shows that the specific heat c_v measured in both crystalline (α-quartz) and glassy SiO_2 [33]. The two systems display a markedly different behavior in the low temperature range. In particular the heat capacity of vitreous silica decreases much more slowly with temperature. Crystalline quartz data follows the Debye $\sim T^3$ behavior, eq. 1.12 whereas the specific heat of the glass deviates from the predictions and can be described adding a linear term, hence

$$c_v \sim aT + bT^3. \tag{1.13}$$

Below 1 K the specific heat is essentially linear in temperature, indicating a more or less constant density of states in addition to the Debye one. These behavior is described by the two level system model (TLS). This model assumes the existence of local structural instabilities of the glass, capable of tunneling

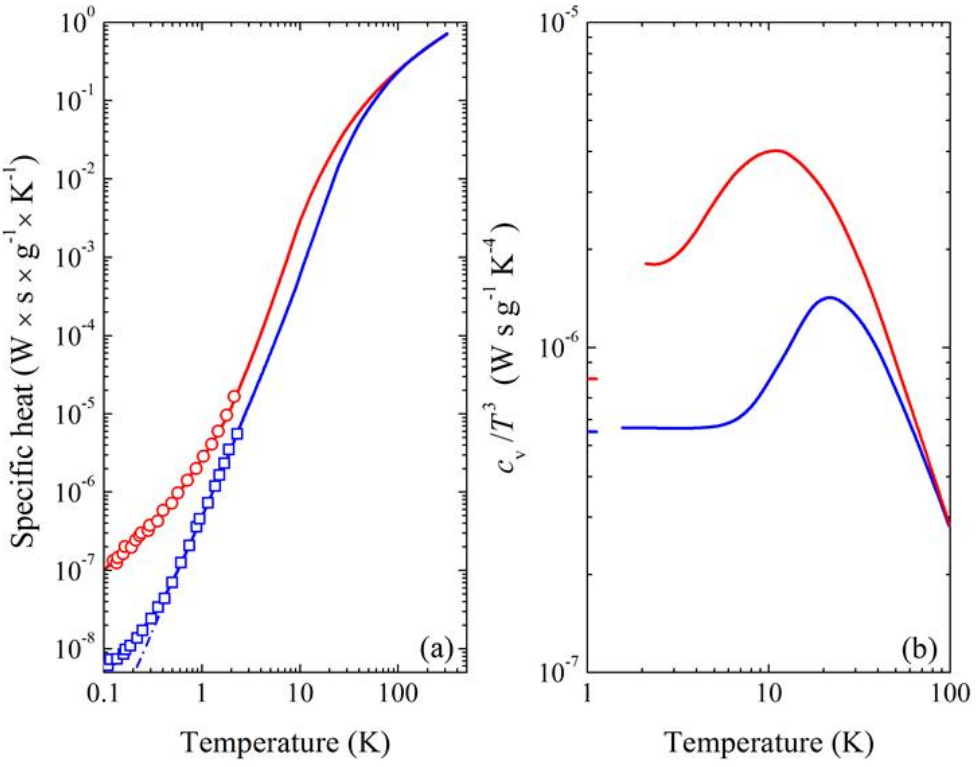

Figure 1.8: (a) measured specific heat for vitreous silica v-SiO_2 (red circles) and α-quartz (blue open squares); (b) specific heat divided to T^3 as for crystals (blue line) and glass (red line); dashed lines are the Debye model predictions. Data are from ref. [33].

among different configurations of the system. The anomalous behavior below 1 K is due to the elastic wave scattering by TLS.

Figure 1.8(b) shows c_v/T^3. The glass heat capacity exceeds the crystalline one, showing a bump at about ~ 10 K. This bump reflects the presence of an excess of modes in the vibrational density of states. It is worth to note that even crystals shows a bump in c_v/T^3 but it is usually related to the transverse acoustic vibrational excitations near the boundary of the first Brillouin zone.

1.7.2 The excess of vibrational states and the boson peak

The vibrational density of states $g(\omega)$ is directly accessible by means of Raman scattering, inelastic neutron scattering (INS), inelastic X-ray scattering (IXS), and nuclear inelastic scattering (NIS). Figure 1.9 show the VDOS measured in vitreous silica by means of inelastic neutron scattering [34]. Comparing the experimental data (red bullets) to the Debye prediction (dashed line), an excess of low energy modes is visible. This excess becomes more evident when we consider the reduced density of states $g(\omega)/\omega^2$, reported in fig. 1.9. In this plot, the Debye VDOS, which is proportional to ω^2, is a constant. On the other hand the glass shows a broad peak which is named *boson peak* (BP).

The boson peak is an universal behavior of glasses and supercooled liquid and it is responsible for the low temperature anomalies in the thermodynamic properties. Furthermore its importance goes beyond the physics of glasses. As a matter of fact the boson peak is a common feature of broad class of substances characterized by disorder, *e.g.* polymers, colloids and biologic material [35, 36].

1.7.3 Theoretical model for the boson peak

Despite of a large theoretical, computational and experimental efforts the explanation of the BP is still an open and debated topic. The main problems can

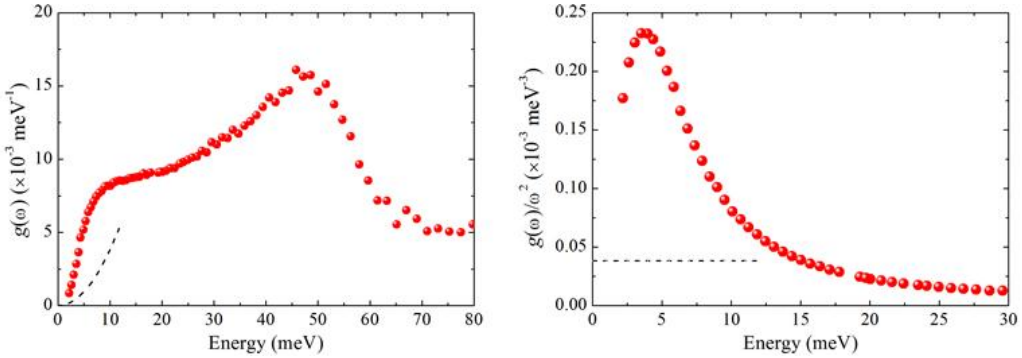

Figure 1.9: Vibrational density of states (a) and reduced vibrational density of states (b) measured in vitreous silica v-SiO_2 by means of neutron inelastic scattering [34]. The dashed line is the Debye level.

be summarized in two questions:

- *What is the nature of the vibrational modes in the boson peak region?*
- *What is the origin of the low frequency pilling up of the modes?*

In the following we present a brief review of the approaches used to explain the BP. It is worth noting that even starting from different and often incompatible assumptions, these model prodictions are qualitatively similar. It is therefore difficult to setup experiments able to discriminate between different model.

Dynamical disorder A first class of models that describes the boson peak is based on the presence of dynamical disorder in the glass.

In the model proposed by Taraskin and co-worker atoms occupy crystalline sites and the system is described as formed by coupled harmonic oscillators interacting through random independent elastic force constants K_{ij} whose strength fluctuates according a probability distribution $P(K_{ij})$ [37]. On increasing the width of the distribution $P(K_{ij})$, the system becomes unstable, thus with negative force constants K_{ij} , and this instability gives rise to the well know excess of modes in the vibrational density of state. Wider is the distribution, stronger

the BP will be. In this approach the excess in the reduced VDOS is associated with the lowest van Hove singularity in the spectrum of the reference crystalline system, although the disorder causes its broadening and a downwards shift in energy. The vibrational modes originating the lowest van Hove singularity in the crystal are also those responsible for the boson-peak in the corresponding glass. In general, they seem to be related to transverse branches. A more recent model proposed by Schirmacher and co-workers [38, 39, 40] is based on a macroscopic tensorial elastic and lattice-independent approach. The model assumption is that the disorder leads to microscopic random spatial fluctuations of the transverse elastic constant (shear modulus) whose variance is proportional to a disordered parameter γ. The DOS excess arises from a band of disorder induced irregular vibrational states, the onset of which approaches lower frequencies as the disorder is increased. The model predicts also a strict correlation between the excess in the vibrational density of states and the sound damping of the acoustic waves present in the corresponding energy range.

Euclidean Random Matrix Euclidean Random Matrix models should not be included in the HRM class, even if they are developed in the harmonic approximation. As a matter of fact the model deals directly with a topological disordered solid. The Euclidean random matrix provides a theoretical framework to treat the problem of the topological disorder, where the interactions cannot be split in an ordered part plus a disorder dependent contribution [41]. This model supports the idea that the boson peak marks the transition between acoustic like excitations and a disorder dominated regime for the vibrational spectrum.

Soft Potential Model The Soft Potential Model (SPM) assumes the existence of additional quasi-local vibrations (QLV) that interact with the sound

waves, giving rise to the boson peak [42, 43, 44]. This model can be considered as an extension at higher temperature of the two level system model (TLS), describing the thermal anomalies of glasses below 1 K.

QLV are additional non acoustic modes characterized by a large vibrational amplitude of some group of atoms. The physical origin of these modes can be traced to local irregularities of the amorphous structure, or to low-lying optical modes in parental crystals. The disorder destroys the long range coherence of these optical modes so they are indistinguishable from quasi-local modes. The vibrational density of states of QLV's cannot be arbitrary, depending only on the particulars of the glass. QLV's can be described as low frequency harmonic oscillators which weakly couple to the sound waves of the elastic continuum medium. This coupling leads to a dipole-dipole interaction between different harmonic oscillators. The interaction between harmonic oscillators give rise to a $g(\omega)$ which is a universal function at low frequency [44]. This universality derives from the vibrational instability of the spectrum due to the interacting harmonic oscillators. For $\omega_c < \omega_D$, anharmonicity stabilizes the system in a new minimum thus it reconstructs the VDOS in a new spectrum. As a final result $g(\omega)/\omega^2$ shows a maximum without a peak in the density of states.

In the SPM, the boson peak energy depends on the interaction strength among the different HO's. The stronger the interaction, the higher is the energy of the boson peak maximum. The weak coupling between QLV's and acoustic modes and the continuum medium avoids any influence of the localized modes on the acoustic properties of the system. In this way the model is able to explain both boson peak and acoustic features. Moreover, a recent work pointed out a direct link between boson peak and two-level systems: the raising of a peak in the reduced vibrational density of states seems to inevitably lead to the creation of two-level systems and *vice versa* [43]

Inhomogeneous cohesion Another approach consists on ascribing the BP to the inhomogeneous cohesion of glasses at the nanometric scale [45].

In this case the system is assumed to consist of an aggregate of "regions" with different elastic constants. The material is characterized by more cohesive domains separated by softer interdomain zones on the nanometric spatial range. The boson peak arises from vibrational modes spatially localized in such regions. In particular, the excess of modes in the VDOS is viewed as the signature of the hybridization of acoustic modes with localized ones, inherent to the elastic heterogeneities. The heterogeneous elastic response at the nano-scale can possibly be related to the existence of dynamical heterogeneities observed in supercooled liquids above the glass [16]. Cohesion heterogeneities in glasses would originate from the mobility heterogeneities in the supercooled state conserved during the glass transition. Spatially correlated dynamics of the molecules in the melt is somehow "frozen in" at the glass transition, and leads to the creation of softer and harder zones in the glassy phase. Conversely the existence of elastic inhomogeneities in the mesoscopic spatial range does not imply automatically the existence of visible static density inhomogeneities. As a matter of fact, elasticity fluctuation can correspond to a negligible density fluctuation [45].

Spatially correlated modes The boson peak has been suggested to reflect a crossover from long wavelength vibrations propagating in the continuous media to localized vibrations on a characteristic length scale of $R \sim 10$ Å. This length has been interpreted as the correlation length for the disordered structure of the system [46, 47]. The energy of the peak result to be inversely proportional to the size of these spatial correlated regions, $\omega_{BP} \sim 1/R$. This correlation length R has been connected to the medium range order extension as obtained considering the width or the position of the first sharp diffraction peak of the glass [46].

Chapter 2

Experimental probes: X-ray and neutrons

Experiments must be reproducible.
They should all fail in the same way.
Finagle's third law

The study of the dynamics of a solid can be approached by perturbing the equilibrium of the system by an external force and recording its reaction, *i.e.* the relaxation to the equilibrium state. Paying attention that the perturbation does not alter too much the properties of the system it is possible to get information of the forces acting in the system.

The reliability of an experimental technique which follows this procedure is based on the theorem of the linear response which states the equivalence between the response of the system in regime of small perturbation (linear response) and the spontaneous fluctuations in absence of perturbation [48].

The atomic dynamics can be investigated by means of inelastic scattering techniques. In an inelastic scattering experiment the measured signal is determined by the double differential scattering cross section. This conveys the

fraction of the incident probe with energy E_i and wavevector $\mathbf{k}_i$ which is scattered into an element of solid angle $d\Omega$, in direction given by k_f, with an energy between E_f and $E_f + dE_f$. The cross section has the dimensions of an area and it is denoted by

$$\frac{d^2\sigma}{d\Omega dE_f} \tag{2.1}$$

Within the linear response theory the cross section can be written quite generally as the product of three terms which describe:

1. the intensity of the probe-sample coupling (independent from the energy of the incident particle);

2. the phase-space volumes of the incident and scattered particles;

3. the space and time Fourier transform of the correlation function of the observable in the system which couples to the probe.

The last term contains the information related to the elementary excitations characteristic of the system.

In this chapter we will briefly outline the basic theory of both inelastic X-ray scattering (IXS) [49, 50, 51, 52] and inelastic neutron scattering (INS) [48, 24, 53, 54]. Moreover we will derive an expression for the main quantity involved in this study, namely the static structure factor [51].

2.1 Inelastic X-ray scattering

Inelastic X-ray scattering is a relatively new inelastic technique. As a matter of fact the main limitation to the development of this technique was extremely high energy resolution. Photons with a wavelength of $\lambda = 0.1$ nm have an energy of about 12 keV. Therefore, the study of phonon excitations in condensed matter

is necessary a resolution better than $\Delta E/E \sim 10^{-7}$. However, once overcome these technical difficulties, IXS provides a powerful investigation tool.

In a typical inelastic X-ray scattering experiment the incident photon with energy E_i, wavevector $\mathbf{k}_i$ and a polarization $\hat{\varepsilon}_i$ is scattered by the sample and collected at an angle ϑ within a solid angle $d\Omega$. The scattered photon energy, wavevector and polarization are E_f, $\mathbf{k}_f$, and $\hat{\varepsilon}_f$.

The energy and momentum conservation impose that:

$$\hbar\omega = E_f - E_i; \quad \mathbf{Q} = \mathbf{k}_f - \mathbf{k}_i; \tag{2.2}$$

The relation between momentum and energy in the case of photons is given by $E = c\hbar k$, where c is the speed of light. We can write:

$$\begin{aligned} Q^2 &= k_i^2 + k_f^2 - k_i k_f \cos\vartheta/2 \\ &= k_i^2 \left[1 + \left(1 - \frac{E}{E_i}\right)^2 - 2\left(1 - \frac{E}{E_i}\right)\cos\vartheta \right]. \end{aligned} \tag{2.3}$$

Considering that the exchanged energy associated to phonon-like excitations is ∼meV, always smaller than the energy of the incident photons ∼KeV, 2.3 becomes:

$$Q = 2k_i \sin\vartheta/2, \tag{2.4}$$

i.e. the ratio between the exchanged momentum and the incident photon momentum is completely determined by the scattering angle ϑ.

2.1.1 X-ray inelastic scattering cross section

In the weak relativistic limit the Hamiltonian describing the electron-photon interaction consists of four terms. If we neglect resonance phenomena close to X-ray absorption thresholds, the much weaker magnetic couplings, and the direct photon-nucleus coupling the Hamiltonian reduces to the Thomson interaction

term, *i.e.*

$$H_{int} = \frac{1}{2} r_0 \sum_j \mathbf{A}^2 (\mathbf{r}_i, t) , \tag{2.5}$$

where $r_0 = e^2/m_e c^2$ is the classical electron radius, e and m_e the charge and the rest mass of the electron; $\mathbf{A}(r_i, t)$ is the electromagnetic field vector potential in the $\mathbf{r}_i$, coordinate of the ith electron. The sum extends over all the electrons in the system.

In a scattering process, where a photon of energy E_i, wavevector k_i, and polarization ε_i, is scattered into a final state of energy E_f, wavevector $\mathbf{k}_f$, and polarization $\hat{\varepsilon}_f$, and the electron system goes from the initial state $|I\rangle$ to the final state $|F\rangle$. The double differential cross section can be written as

$$\frac{d^2\sigma}{d\Omega dE_f} = \frac{dP_{i\to f}}{dt} \frac{1}{j} \rho_s (E) , \tag{2.6}$$

where $\rho_s(E)$ is the density of states of scattering angle, j the incident current density and $dP_{i\to f}/dt$ is the probability rate per sample and probe unit that a probe particle makes the transition from the initial to the final state [55]. The transition of the incident particle between i and f involves many possible elementary excitations in the sample. Indicating $dP_{i,|I\rangle\to f,|F\rangle}/dt$ the scattering probability involving the transition in the sample, the total probability can be expressed as a sum over the initial and final states. The transition probability can be calculated from the perturbation theory using the Fermi's golden rule. Assuming that the initial and final photon states are plane waves, one gets:

$$\frac{d^2\sigma}{d\Omega dE_f} = r_0^2 \frac{k_f}{k_i} (\hat{\varepsilon}_f \cdot \hat{\varepsilon}_i)^2 \sum_{I,F} P_I \left| \langle F | \sum_i e^{i\mathbf{Q}\cdot\mathbf{r}_i} | I \rangle \right|^2 \delta (\hbar\omega - E_f + E_i) , \tag{2.7}$$

where P_I is the statistical weight, i.e. the equilibrium population of the initial states.

The double differential cross section in eq. 2.7 contains the correlation function of the electron density. The correlation function of the atomic density

can by obtained assuming that the adiabatic approximation holds. The adiabatic approximation allows the separation of the system quantum state $|S\rangle$ into the product of a nuclear part $|S_n\rangle$ and an electronic part, $|S_e\rangle$, which depends only parametrically by the coordinates of the nuclei. We can thus write $|S\rangle = |S_n\rangle\,|S_e\rangle$. This approximation is particularly good for exchanged energies that are small with respect to the excitations energies of electrons in bound core states. In metals, this approximation, one neglects the portion of the total electron density in proximity of the Fermi level. Moreover we consider only the case in which the electronic part of the total wave function is not changed by the scattering process. The differences between the initial state and the final state are only due to excitations associated with atomic density fluctuations. Equation 2.7 can be rewritten as:

$$\frac{d^2\sigma}{d\Omega dE_f} = r_0^2 \frac{k_f}{k_i} \left(\hat{\varepsilon}_f \cdot \hat{\varepsilon}_i\right)^2 \sum_{I_n,F_n} P_{I_n} \left| \langle F_n | \sum_i f_i\left(Q\right) e^{i\mathbf{Q}\cdot\mathbf{r}_i} |I_n\rangle \right|^2 \delta\left(\hbar\omega - E_f + E_i\right), \tag{2.8}$$

where $f_k\left(Q\right)$ is atomic form factor of the ith atom with position vector $\mathbf{R}_i$. The states $|I_n\rangle$ and $|F_n\rangle$ are the initial and final nuclear state. Assuming that all the scattering units are equal, eq. 2.8 becomes:

$$\frac{d^2\sigma}{d\Omega dE_f} = r_0^2 \frac{k_f}{k_i} \left(\hat{\varepsilon}_f \cdot \hat{\varepsilon}_i\right)^2 \left|f\left(Q\right)\right|^2 S\left(\mathbf{Q},\omega\right), \tag{2.9}$$

where $\left(d\sigma/d\Omega\right)_T = r_0^2 \left(\frac{k_f}{k_i}\right) \left(\hat{\varepsilon}_f \cdot \hat{\varepsilon}_i\right)^2$ is the Thomson scattering cross section and $S\left(Q,\omega\right)$ is the dynamic structure factor, i.e.

$$S\left(\mathbf{Q},\omega\right) = \frac{1}{2\pi\hbar N} \int_{\infty}^{+\infty} dt e^{i\omega t} \left\langle \sum_{ij} e^{i\mathbf{Q}\cdot\mathbf{r}_i(t)} e^{-i\mathbf{Q}\cdot\mathbf{r}_j(0)} \right\rangle \tag{2.10}$$

where $\langle \ldots \rangle$ is the thermal average.

In the limit $Q \to 0$ the form factor $f\left(Q\right)$ is equal to the number of electrons in the scattering atom. Increasing Q, $f\left(Q\right)$ decreases almost exponentially. The

decay constant is determined by the size of the radial distribution of the electrons in the atomic shells of the considered atom.

The double differential cross-section of equation 2.9 is valid for a system composed of a single atomic species. This derivation can be generalized to molecular or crystalline systems by substituting the atomic form factor with either the molecular form factor or the elementary cell form factor. If the system is multi-component and disordered, the factorization is not straightforward and it is possible only assuming some distribution among the different atoms. In the limit case of a completely random distribution, an incoherent contribution appears in the X-ray scattering cross-section [50].

2.2 Inelastic neutron scattering

Neutrons are subnuclear massive particles with zero electrical charge. Neutrons interact with matter mainly via nuclear interaction and they are a perfect probe to investigate the matter. In fact, the energy of neutrons with wavelengths of the order of inter-particle distances is about 100 meV, and therefore comparable to the energy of collective excitations.

We consider the scattering of unpolarized neutrons. The energy and momentum conservation impose that:

$$\hbar\omega = E_i - E_f; \quad \mathbf{Q} = \mathbf{k}_f - \mathbf{k}_i; \tag{2.11}$$

For neutrons, *i.e.* massive particles, the relation between momentum and energy is given by $E = \hbar k_i^2/2m_n$, where m_n is the neutron mass. This leads:

$$\begin{aligned} Q^2 &= k_i^2 + k_f^2 - k_i k_f \cos\vartheta/2 \\ &= k_i^2 \left[1 + \left(1 - \frac{E}{E_i}\right) - 2\cos\vartheta\sqrt{1 - \frac{E}{E_i}}\right] \end{aligned} \tag{2.12}$$

Equation 2.12 imposes limitations to the region of the (Q, E) plane which can be explored in a neutron inelastic scattering experiment. The kinematic region

accessible to INS is reported in figure 2.1. Neutron scattering experiments have to face these limitations. As a matter of fact, in the case of acoustic excitation propagating with the dispersion relation $E = v_s \hbar Q$, the neutron technique can be applied only if $v_n > v_s$ where v_n is the incident neutron velocity.

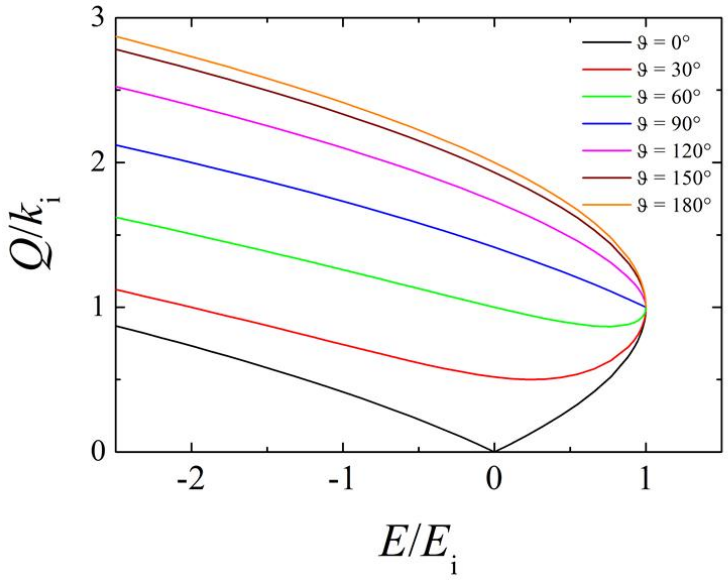

Figure 2.1: Kinematic region accessible to INS.

2.2.1 Neutron inelastic scattering cross section

The double differential cross-section can be determined in the framework of the first order perturbation theory on the basis of the Fermi golden rule [48]. The initial state of the system composed by the incident neutron and the target is, $|I\rangle = |k_i, \lambda\rangle \equiv |k_i\rangle\,|\lambda\rangle$. The state of the neutron is a plane wave labeled with k_i, whereas the system is labeled with λ. The states $|\lambda\rangle$ form a complete set with the closure relation $\sum_\lambda |\lambda\rangle\,\langle\lambda| = 1$.

The double differential cross section can be written as

$$\frac{d^2\sigma}{d\Omega dE_f} = \frac{k_f}{k_i}\overline{\sum_{\lambda,\lambda'} P_\lambda \left|\langle k_f\lambda_f|\,\hat{V}\,|k_i\lambda_i\rangle\right|^2 \delta\left(\hbar\omega - E_\lambda + E_{\lambda'}\right)}, \tag{2.13}$$

where $\hat{V}$ is the interaction potential that causes the transition and E_λ $E_{\lambda'}$ associated with the target initial and final states respectively. P_λ represents the probability of finding the system in the initial state I. The horizontal bar stands for the any relevant averages over and above those included in the weights P_λ, *e.g.* the distribution of isotopes, the nuclear spin orientation, or the precise positions of the nuclei.

Neutrons interact with matter both via nuclear and magnetic interactions but, for our purposes, we can neglect the magnetic term considering only the interaction between neutrons and nuclei. Even if a complete theory for the nucleon-nucleon interaction is still lacking we can write the interaction using the so-called Fermi pseudo potential:

$$\hat{V}(\mathbf{r}) = \frac{2\pi\hbar^2}{m_n} b\delta(\mathbf{r} - \mathbf{R}) \tag{2.14}$$

where R is the position of the nucleus and b the scattering length of the atom. It is worth to note that this expression is only a mathematical description ensuring that using the Born approximation the scattering is isotropic and thus described by the single parameter b. Indeed, perturbation theory is inapplicable to the scattering of a neutron by a nucleus because, although the potential has a very short range ($\sim 10^{-15}$ m), it is very strong. The Fermi pseudo-potential does not correspond to the actual nuclear potential, it is a formal artifice defined to give, in the Born approximation, what is correct for s-wave scattering.

Considering a system of atoms in the positions $\{\mathbf{R}\}$ with $\mathbf{R}_i$ the position of the ith nucleus. The Fermi pseudo potential can be written as [48]:

$$\left(\frac{m_n}{2\pi\hbar^2}\right)\hat{V}(\mathbf{r}) = \sum_i \hat{V}_i \delta(\mathbf{r} - \mathbf{R}_i) \tag{2.15}$$

If we sobstitute 2.15 into 2.13, the double differential cross section becomes:

$$\frac{d^2\sigma}{d\Omega dE} = \frac{k_f}{k_i} \sum_{\lambda,\lambda'} P_\lambda \overline{\left| \langle \lambda' | \sum_i \hat{V}_i(\mathbf{Q}) e^{(i\mathbf{Q}\cdot\mathbf{R}_i)} | \lambda \rangle \right|^2} \delta(\hbar\omega + E_\lambda - E_{\lambda'}). \tag{2.16}$$

where

$$\hat{V}_i(\mathbf{Q}) = \int d\mathbf{r} \exp(i\mathbf{Q}\cdot\mathbf{r})\,\hat{V}(\mathbf{r}), \tag{2.17}$$

so that

$$\langle \mathbf{k}_f | \hat{V} | \mathbf{k}_i \rangle = \sum_i \hat{V}_i(\mathbf{Q}) \exp(i\mathbf{Q}\cdot\mathbf{r}). \tag{2.18}$$

Writing the δ-function in its integral form and using the Heisenberg operator property, $\hat{\mathcal{O}}(t) = e^{it\mathcal{H}/\hbar}\hat{\mathcal{O}}e^{-it\mathcal{H}/\hbar}$, equation 2.16 can be written as:

$$\begin{aligned}\frac{d^2\sigma}{d\Omega dE_f} &= \frac{k_f}{k_i}\frac{1}{2\pi\hbar}\int_{-\infty}^{\infty} dt e^{-i\omega t} \\ &\times \overline{\sum_{i,j}\left\langle e^{\left(-i\mathbf{Q}\cdot\hat{\mathbf{R}}_i\right)}\hat{V}_i^*(\mathbf{Q})\,\hat{V}_j(\mathbf{Q},t)\,e^{\left(-i\mathbf{Q}\cdot\hat{\mathbf{R}}_j(t)\right)}\right\rangle}.\end{aligned} \tag{2.19}$$

Where the suffix * indicates the complex conjugate and the angular brackets $\langle\ldots\rangle$ the thermal average of the enclosed quantity. $\hat{\mathbf{R}}(0) \equiv \hat{\mathbf{R}}$ If the average denoted by the horizontal bar is independent on the thermal average, eq. 2.19 can be written as

$$\frac{d^2\sigma}{d\Omega dE_f} = \frac{k_f}{k_i}\frac{1}{2\pi\hbar}\int_{\infty}^{\infty} dt e^{-it\omega}\overline{\sum_{i,j}\hat{V}_j^*(\mathbf{Q})\,\hat{V}_i(\mathbf{Q})\left\langle e^{\left(-i\mathbf{Q}\cdot\hat{\mathbf{R}}_i\right)}e^{\left(-i\mathbf{Q}\cdot\hat{\mathbf{R}}_j(t)\right)}\right\rangle}. \tag{2.20}$$

For a monoatomic target sample

$$\overline{\hat{V}_j^*(\mathbf{Q})\,\hat{V}_i(\mathbf{Q})} = \overline{b_i^* b_j} = \left|\bar{b}\right|^2 + \delta_{ij}\left[\overline{|b|^2} - \left|\bar{b}\right|^2\right]. \tag{2.21}$$

The average of the scattering length $\bar{b}_i$ over all isotopes and spin is called coherent scattering length; conversely the mean square deviation of b_i from its average value is known as the incoherent scattering length, thus:

$$\left|\bar{b}\right|^2 = b_{coh}^2 = \tfrac{\sigma_{coh}}{4\pi};\quad \overline{|b|^2} - \left|\bar{b}\right|^2 = b_{inc}^2 = \tfrac{\sigma_{inc}}{4\pi}. \tag{2.22}$$

Therefore, it is possible to separate the coherent and the incoherent contribution

to the scattering cross section being:

$$\begin{aligned}\sum_{i,j}\overline{\hat{V}_j^*(\mathbf{Q})\hat{V}_i(\mathbf{Q})}\left\langle e^{\left(-i\mathbf{Q}\cdot\hat{\mathbf{R}}_i\right)}e^{\left(-i\mathbf{Q}\cdot\hat{\mathbf{R}}_j(t)\right)}\right\rangle &= \sum_{i,j}\overline{b_i^*b_j}\left\langle e^{\left(-i\mathbf{Q}\cdot\hat{\mathbf{R}}_i\right)}e^{\left(-i\mathbf{Q}\cdot\hat{\hat{R}}_j(t)\right)}\right\rangle \\ &= \sum_{i,j}\frac{\sigma_{coh}}{4\pi}\left\langle e^{\left(-i\mathbf{Q}\cdot\hat{\mathbf{R}}_i\right)}e^{\left(-i\mathbf{Q}\cdot\hat{\mathbf{R}}_j(t)\right)}\right\rangle \\ &+ \sum_{i}\frac{\sigma_{inc}}{4\pi}\left\langle e^{\left(-i\mathbf{Q}\cdot\hat{\mathbf{R}}_i\right)}e^{\left(-i\mathbf{Q}\cdot\hat{\mathbf{R}}_j(t)\right)}\right\rangle\end{aligned} \tag{2.23}$$

In this way the double differential cross section of eq. 2.20 becomes

$$\frac{d^2\sigma}{d\Omega dE_f} = \frac{k_f}{k_i}\left\{\frac{\sigma_{coh}}{4\pi}S(\mathbf{Q},\omega)+\frac{\sigma_{inc}}{4\pi}S_i(\mathbf{Q},\omega)\right\}. \tag{2.24}$$

The functions $S(Q,\omega)$ and $S_s(Q,\omega)$ are the so called dynamic structure factor, and dynamic self structure factor defined as

$$S(\mathbf{Q},\omega) = \frac{1}{2\pi\hbar N}\int_{\infty}^{\infty}dte^{-it\omega}\sum_{i,j}\left\langle e^{\left(-i\mathbf{Q}\cdot\hat{\mathbf{R}}_i\right)}e^{\left(-i\mathbf{Q}\cdot\hat{\mathbf{R}}_j(t)\right)}\right\rangle; \tag{2.25}$$

$$S_s(\mathbf{Q},\omega) = \frac{1}{2\pi\hbar N}\int_{\infty}^{\infty}dte^{-it\omega}\sum_{i}\left\langle e^{\left(-i\mathbf{Q}\cdot\hat{\mathbf{R}}_i\right)}e^{\left(-i\mathbf{Q}\cdot\hat{\mathbf{R}}_j(t)\right)}\right\rangle. \tag{2.26}$$

In the case of coherent nuclear scattering, the interaction potential couples the neutron to the density of the target system. The coherent scattering cross section gives information on the collective motions of the atoms thus on the wavevectors and frequency of the vibrational modes, and allows to map the dispersion relation in the $(\mathbf{Q},\omega)$ space. On the other hand the incoherent gives information on the single particle dynamics trough the dynamic structure factor self. It is worth to note that in the limit of large $\mathbf{Q}$ which corresponds to short wavelenghts, coherent processes are minimal so that $S(\mathbf{Q},\omega)=S_s(\mathbf{Q},\omega)$.

2.2.2 Scattering from nuclei undergoing harmonic vibrations

Let us assume time dependent positions of the N atoms of the system. The time dependent atomic position of the ith atom $\mathbf{R}_i$ is the sum of equilibrium position $\mathbf{r}_i^0$ and displacement $\mathbf{u}_i(t)$,

$$\mathbf{R}_i(t) = \mathbf{r}_i^0 + \mathbf{u}_i(t). \tag{2.27}$$

Sobstuting 2.27 in 2.20 we obtain:

$$\begin{aligned}\frac{d^2\sigma}{d\Omega dE_f} &= \frac{k_f}{k_i}\frac{1}{2\pi\hbar}\int_\infty^\infty dt e^{-it\omega}\sum_{i,j}\overline{b_i^* b_j}\left\langle e^{\left(-i\mathbf{Q}\cdot\hat{\mathbf{R}}_i\right)}e^{\left(-i\mathbf{Q}\cdot\hat{\mathbf{R}}_j(t)\right)}\right\rangle \\ &= \frac{k_f}{k_i}\frac{1}{2\pi\hbar}\sum_{i,j}\overline{b_i^* b_j}e^{-i\mathbf{Q}\cdot\left(\mathbf{r}_i^0-\mathbf{r}_j^0\right)}\int_\infty^\infty dt e^{-it\omega}\left\langle e^{(-i\mathbf{Q}\cdot\mathbf{u}_i)}e^{(i\mathbf{Q}\cdot\mathbf{u}_j(t))}\right\rangle\end{aligned} \tag{2.28}$$

In the harmonic approximation, using the Bloch identity for the argument of the integral, we can shift the average to the exponent:

$$\begin{aligned}\left\langle\exp\left(-i\mathbf{Q}\cdot\mathbf{R}_i\right)\exp\left(i\mathbf{Q}\cdot\mathbf{R}_j(t)\right)\right\rangle &= e^{-W_i}e^{-W_j}e^{\langle(\mathbf{Q}\cdot\mathbf{u}_i)(\mathbf{Q}\cdot\mathbf{u}_j(t))\rangle} \\ &= e^{-2W}e^{\langle(\mathbf{Q}\cdot\mathbf{u}_i)(\mathbf{Q}\cdot\mathbf{u}_j(t))\rangle}\end{aligned} \tag{2.29}$$

The exponent W_i is called Debye-Waller factor. It is equal to $\frac{1}{2}\left\langle\left(\mathbf{Q}\cdot\mathbf{u}_i\right)^2\right\rangle$ provided that the atomic displacements follow a Gaussian distribution. In a cubic symmetry the average is $\frac{1}{6}Q^2\left\langle u\right\rangle^2$ and this result is a fair approximation also for isotropic systems. The mean square displacement can be used as an indicator of the non harmonic behavior of the material or of the existence of relaxational phenomena, *e.g.* [15]. Moreover is directly connected with the density of states $g(\omega)$,

$$\left\langle u^2\right\rangle = \frac{\hbar}{2m}\int_\infty^\infty \frac{g(\omega)}{\omega}\left[2n(\omega,T)+1\right]d\omega \tag{2.30}$$

where m is the molecular mass and $n(\omega,T)$ the Bose factor.

We can separate the coherent and the incoherent contribution to the differential neutron scattering cross section:

$$\left(\frac{d^2\sigma}{d\Omega dE_f}\right)_{coh} = \frac{k_f}{k_i}\frac{1}{2\pi\hbar}e^{-2W}\frac{\sigma_{coh}}{4\pi}\sum_{ij}e^{-iQ\cdot\left(\mathbf{r}_i^0-\mathbf{r}_j^0\right)}\int_{\infty}^{\infty}dte^{-i\omega t}e^{\langle\mathbf{Q}\cdot\mathbf{u}_i\mathbf{Q}\cdot\mathbf{u}_j(t)\rangle}; \tag{2.31}$$

$$\left(\frac{d^2\sigma}{d\Omega dE_f}\right)_{inc} = \frac{k_f}{k_i}\frac{1}{2\pi\hbar}e^{-2W}\frac{\sigma_{inc}}{4\pi}\sum_{i}\int_{\infty}^{\infty}dte^{-i\omega t}e^{\langle\mathbf{Q}\cdot\mathbf{u}_i\mathbf{Q}\cdot\mathbf{u}_i(t)\rangle}. \tag{2.32}$$

If we expand the exponential of eq. 2.29:

$$e^{\langle(\mathbf{Q}\cdot\mathbf{u}_i)(\mathbf{Q}\cdot\mathbf{u}_j(t))\rangle} = e^{\langle UV\rangle} = 1 + \langle UV\rangle + \frac{}{2}\langle UV\rangle^2 + \ldots. \tag{2.33}$$

The first term in eq. 2.33 corresponds to the elastic scattering and the second one to one-phonon scattering events. Further terms correspond to multiphonon effects and can be considered as a small correction.

The coherent one phonon cross section for a Bravais lattice reads:

$$\begin{aligned}\left(\frac{d^2\sigma}{d\Omega dE_f}\right)_{coh}^{1p} &= \frac{\sigma_{coh}}{4\pi}\frac{k_f}{k_i}\frac{(2\pi)^2}{2mv_0}\sum_{\mathbf{G}}e^{-2W\mathbf{Q}}\sum_{i,\mathbf{q}}\frac{\left|\mathbf{Q}\cdot\mathbf{e}^j(\mathbf{q})\right|^2}{\omega_j(\mathbf{q})} \\ &\times \left[n_j(\mathbf{q})\,\delta\left(\omega+\omega_j(\mathbf{q})\right)\delta\left(\mathbf{Q}+\mathbf{q}-\mathbf{G}\right)\right. \\ &+ \left. n_j(\mathbf{q}+1)\,\delta\left(\omega-\omega_j(\mathbf{q})\right)\delta\left(\mathbf{Q}-\mathbf{q}-\mathbf{G}\right)\right].\end{aligned} \tag{2.34}$$

The cross section 2.34 is the sum of two terms. The first, which contains the expression $\delta\left(\omega+\omega_j(\mathbf{q})\right)\delta\left(\mathbf{Q}+\mathbf{q}-\mathbf{G}\right)$, represents a scattering process in which one phonon is annihilated. On the other hand, the second term, containing $\delta\left(\omega-\omega_j(\mathbf{q})\right)\delta\left(\mathbf{Q}-\mathbf{q}-\mathbf{G}\right)$, represents a process in which one phonon is created. The two δ-functions imply that the scattering obeys to the conditions:

$$\hbar\omega = E_f - E_i; \quad \mathbf{G} = \mathbf{Q}+\mathbf{q}; \tag{2.35}$$

with $\mathbf{q}$ lying in the First Brillouin Zone and $\mathbf{G}$ a vector of the reciprocal lattice. These conservation conditions imply that the coherent scattering yields information on the wave-vector and the frequency of the vibrational normal modes, permitting to map the dispersion relations in the $(\mathbf{Q}, E)$ space.

On the other hand, the incoherent scattering cross section directly measures the vibrational density of states $g(\omega)$. In fact, the one-phonon incoherent cross section reads:

$$\left(\frac{d^2\sigma}{d\Omega dE_f}\right)_{inc}^{1p} = \frac{\sigma_{inc}}{4\pi}\frac{k_f}{k_i}\frac{N}{m}Q^2 e^{-2W_{\mathbf{Q}}}\frac{g(\omega)}{\omega}\left[n(\omega)+1\right]. \tag{2.36}$$

Equation 2.36 means that it is possible to obtain information on the VDOS of a system by measurin the incoherent contribution to the scattering cross section.

2.3 The dynamic structure factor

In this section we will derive an expression for the dynamic structure factor in disorder systems [56, 57, 51].

Let us start from some basic definition. The microscopic number density $\rho_n(\mathbf{r}, t)$ of a system of N point particles is defined as

$$\rho_n(\mathbf{r}, t) = \sum_i \delta\mathbf{r} - \mathbf{r}_i(t). \tag{2.37}$$

Its mean value is the mean number density $\rho_N = N/V$ where V is the volume occupied by the system. The relevant quantity is the density fluctuation,

$$\delta\rho_n(\mathbf{r}, t) = \rho_n(\mathbf{r}, t) - \rho_n, \tag{2.38}$$

i.e. the difference between the number density and its mean value. The space Fourier transform of the density reads:

$$\rho_n(\mathbf{Q}, t) = \sum_i e^{i\mathbf{Q}\cdot\mathbf{r}_i(t)}, \tag{2.39}$$

The time correlation function associated with the dynamics of density fluctuation is called intermediate scattering function and it is defined as:

$$F(\mathbf{Q},t) = \frac{1}{N}\left\langle \delta\rho_n^*(\mathbf{Q},0)\,\delta\rho_n(\mathbf{Q},t)\right\rangle, \tag{2.40}$$

and its time Fourier transform is the dynamic structure factor $S(\mathbf{Q},\omega)$

$$S(\mathbf{Q},\omega) = \frac{1}{2\pi}\int_{-\infty}^{\infty} e^{i\omega t}F(\mathbf{Q},t). \tag{2.41}$$

The value of the intermediate scattering function at $t = 0$ equals the integral over the frequency of $S(Q,\omega)$ that is the static structure factor $S(\mathbf{Q})$ which is discussed in section 1.4. It is often convenient to define a normalized correlation function as

$$\phi(\mathbf{Q},\omega) = \frac{F(\mathbf{Q},t)}{S(\mathbf{Q})}, \tag{2.42}$$

which is called relaxation function.

The coefficients of the Taylor expansion in time of $\phi(\mathbf{Q},t)$ are called the normalized frequency moments $\omega_0^{2n}(\mathbf{q})$:

$$\omega_0^{2n}(\mathbf{q}) = (-1)^n\frac{d^{2n}\phi(\mathbf{q},t)}{dt^{2n}}\bigg|_{t=0} = \int_{infty}^{\infty} d\omega\omega^{2n}S(\mathbf{Q},\omega) \tag{2.43}$$

In the classical limit all odd moments are zero because the dynamic structure factor is symmetrical in frequency. The other moments define a set of sum rules that constitute a group of constrains for a theory aiming to a correct description of the dynamics.

In the framework of the generalized hydrodynamic theory the evolution of $F(Q,t)$ is given by the Langevin equation [5, 56, 51]

$$\ddot{F}(Q,t) + \omega^2 F(Q,t) + \int_0^t m(Q,t-t')\,\dot{F}(Q,t')\,dt' = 0, \tag{2.44}$$

where $\omega_0^2 = K_BTQ/mS(Q)$ and $m(Q,t)$ is the memory function. By Fourier transformation of eq. 2.44 we obtain

$$S(Q,t) = \frac{1}{\pi}S(Q)\,\frac{\omega_0^2 m'(Q,\omega)}{\left[\omega^2-\omega_0^2+\omega m''(Q,\omega)\right]^2+\left[\omega m'(Q,\omega)\right]^2}, \tag{2.45}$$

where $m'(Q,\omega)$ and $m''(Q,\omega)$ are the real and imaginary parts of the time Fourier transform of the memory function.

A first guess for the memory function $m(Q,t)$ is the so called Markov approximation,

$$m(Q,t) = \Gamma(Q)\,\delta(t)\,. \tag{2.46}$$

This leads to a damped harmonic oscillator (DHO) model for the dynamic structure factor. When the ration Γ/ω_0 is sufficiently small the DHO function is characterized by two side peaks with FWHM $\sim \Gamma(Q)$

The crude Markov approximation can be improved considering the relaxation processes in a glass. These can often be divided into two main classes, associated to two different relaxation times. The structural relaxation processes (α) are associated with a relaxation time τ_α that in a glass can be on the time scale of centuries. This corresponds to the limit $\omega\tau_\alpha \gg 1$ which is certainly reached. On the contrary microscopic processes with timescale τ_μ are faster. Considering this two relaxation processes scenario the memory function can be considered as the sum of two contributions: a constant and very fast decay. The constant reflects contribution of the frozen α relaxation. On the other hand the contribution of these microscopic processes for $\tau_\mu \to 0$ can be described by the Markov approximation considering a δ-function. The memory function can be thus written:

$$m(Q,t) = 2\Gamma(Q)\,\delta(t) + \Delta_\alpha^2(Q)\,, \tag{2.47}$$

where $2\Gamma(Q)$ and $\Delta^2(Q)$ which represent respectively the areas of the instantaneous process and the long time limit of $m(Q,t)$. Equation 2.45 reduces to

$$S(Q,\omega) = S(Q)\left[f_Q\delta(\omega) + (1-f_Q)\,\frac{1}{\pi}\frac{\Omega^2(Q)\,\Gamma(Q)}{\left(\omega^2-\Omega^2(Q)\right)^2+\omega^2\Gamma^2(Q)}\right], \tag{2.48}$$

where

$$\Omega(Q) = \sqrt{\Delta_\alpha^2(Q)+\omega_0^2};\quad f_Q = 1-\omega_0^2/\Omega^2(Q)\,. \tag{2.49}$$

The spectral shape 2.48 can be considered as a reasonable approximation for the dynamic structure factor of glasses well below the glass transition temperature. In this approach the thermal fluctuations have been neglected so that we may speak of an *harmonic glass* approximation. The central line accounts for a fraction f_Q of the total intensity. The parameter f_Q is the so called non ergodicity factor. Moreover, equation 2.48 fulfills the first two sum rule:

$$\int d\omega S\left(Q,\omega\right) = S\left(Q\right); \tag{2.50}$$

$$\int d\omega \omega^2 S\left(Q,\omega\right) = \frac{K_B T}{M} Q^2. \tag{2.51}$$

Equation 2.48 is obtained in a classical approach. To account for the quantum dynamic behavior of the *real* structure factor we have to correct the classical $S\left(Q,\omega\right)$ writing:

$$S_q\left(Q,\omega\right) = \frac{\hbar\omega}{K_B T}\left[n\left(\omega,T\right)+1\right] S\left(Q,t\right), \tag{2.52}$$

where $n\left(\omega,T\right)$ is the Bose-Einstein factor.

Equation 2.52 fulfills the detailed balance condition [48]:

$$S_q\left(Q,-\omega\right) = exp\left(\frac{\hbar\omega}{K_B T}\right) S_q\left(Q,-\omega\right). \tag{2.53}$$

Chapter 3

Boson peak and elastic medium in permanently densified v-SiO_2

It is well known that soluble models are not realistic
and realistic models are not soluble.
G. Parisi

In this chapter we present a study of the densification effects on the vibrational density of states of the prototypical strong glass v-SiO_2. In particular, we focus our efforts on the investigation of the boson peak, *i.e.* the characteristic excess of low energy modes above the Debye level, whose phenomenology has already been introduced in section 1.7.2.

An effective approach in order to gather information on the origin of the boson peak and on the nature of its modes, is the investigation of its evolution as a function of thermodynamical parameters like temperature [58, 59, 60, 61] and pressure [62, 36, 63]. In general, an increase of the system density gives rise to a shift of the BP towards higher frequencies and at the same time to a simultaneous decrease of its intensity. This has been observed also in a permanently densified glass [64, 65, 66] and during the chemical vitrification process of an

epoxy-amine mixture, where the system evolves with the reaction time [67].

All these studies have shown that the BP intensity variation is closely related to its frequency shift. This finding is highlighted by the existence of a master curve that has also been theoretically predicted [41]. When this master curve holds [65, 68] the intensity variation is only apparent and it is due to the BP shift, whose physical origin is still the open problem.

The need for a satisfactory explanation of the BP evolution encompassed in an universal scaling law started with the investigation of its position. A first guess is obtained treating the system as an elastic medium which evolves as a function of the external parameters and is characterized by the Debye frequency ω_D. Within this framework we disentangle the contribution of the excess, which is assumed to be constant, and the elastic medium evolution, which causes the boson peak evolution. This approach has been widely used providing conflicting results. As a matter of fact it works properly in sodium silicate glasses studied as a function of both temperature and density [64, 59] and in the chemical vitrifiing system DGEBA-DETA [67]. Conversely it does not work in vitreous silica as a function of temperature [58, 60] and germania as a function of both temperature [61] and density [65]. Also polymeric systems [62, 36] show a stronger than Debye behavior.

The Debye scaling of the VDOS supports an acoustic origin of the BP; these results point out the existence of further mechanisms [60, 61] claiming for new experiments able to clarify this issue.

Vitreous silica v-SiO_2 is the prototype of the strong covalent network forming glasses [1, 2] and it is probably the most well studied glass in literature. Obsidiana, a natural silica glass, is historically the first glass used by Mankind to produce sharp cutting tools. Moreover, according to Plinius legend, a silica mixture was the first glass quenched by phoenician sailors. The interest in this material arises also from its technological applications, for instance in the field

of optic fibers' technology.

In this chapter we report a detailed Raman scattering investigation of the boson peak in permanently densified vitreous silica. Vitreous silica has been already studied as a function of density by several research groups [69, 70, 71, 72, 73]. We focus on the comparison between the boson peak and the elastic medium, carefully detailed by means of Brillouin Light Scattering (BLS) and Inelastic X-Ray Scattering (IXS) measurements, respectively in the GHz and THz frequency range. We show that in a 10% densification range a scaling law for the BP and a master curve as a function of density both exist. Moreover we demonstrate that the related scaling coefficient has a stronger dependence on density than the Debye frequency. Finally we show a significative change of the vibrational properties when the density is increased up to the 22%. These findings suggest that the Debye scaling of the Boson peak does not cover the full story.

3.1 Sample preparation

Permanently densified silica samples were obtained from a commercial-grade Spectrosil block, purchased from SILO (Florence). Rod pieces were cored from the starting block and then rounded off using a lathe with diamond grinding wheels, obtaining cylinders of 4 mm diameter and 4 mm length. These cylinders were permanently densified using the high-pressure high-temperature multi-anvil apparatus of the CNR-IMEM institute in Parma.

The high pressure part is based on a 6-8 geometry press which is schematically depicted in figure 3.1. Samples are loaded into holes drilled in a ceramic MgO_2 octahedral cell. The faces of the octahedron seat against the truncated corners of a series of eight tungsten carbide anvils, figure 3.1(a). The resulting cube is perfectly arranged in two sets of three wedges (up and down), which

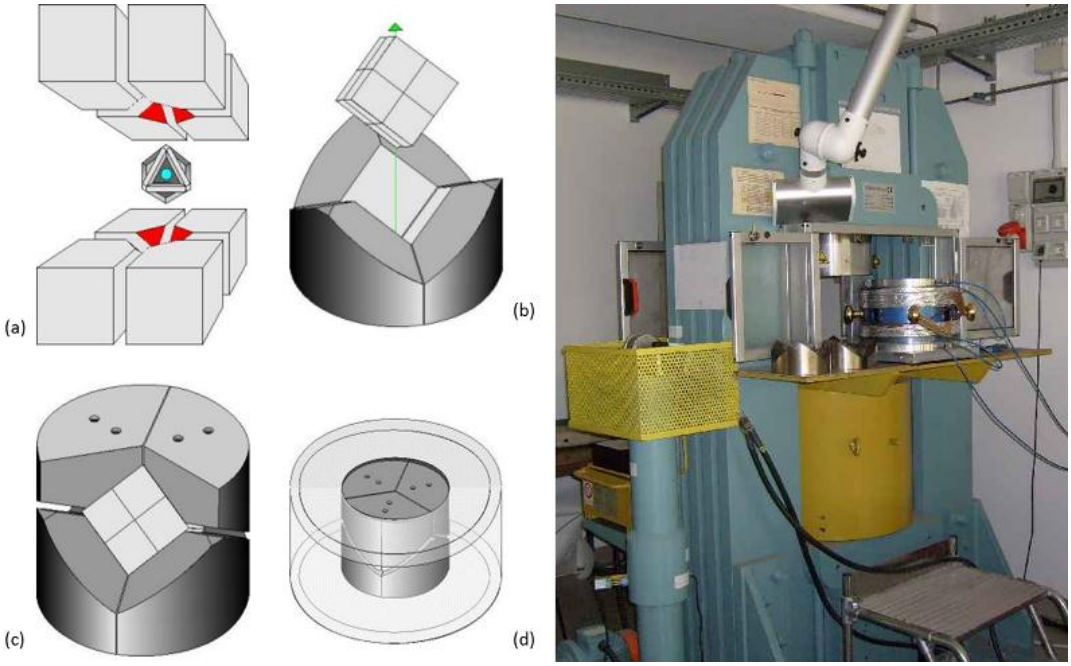

Figure 3.1: Schematic representation of the multi anvil apparatus; (a) shows the ceramic octahedron arranged inside the anvils; (b) and (c) depict the position of the anvil cubic assembly inside the six wedges which are put inside the module (d). The right picture shows the HP-HT apparatus at the CNR-IMEM institute in Parma. The wedges as well as the multi anvil mudule showed in (d) are clearly visible on the shelf in front of the press.

act upon the faces of the cubic assembly. This set-up is clearly visible in figures 3.1(b) and (c). These two sets of wedges are placed between the upper and the lower plates of a large press, figure 3.1(d). This set-up ensures that the pressure linearly applied by the press can be efficiently converted into an hydrostatic compression of the sample. The high temperatures are obtained using an internal resistance furnace (graphite or $LaCrO_3$).

To prevent any sample contamination, the cylindrical pieces were encapsulated in a noble metal container, a Pt foil of 50 μm thickness. The so obtained capsule was inserted in the octahedral cell and then in the multi-anvil apparatus. The pressure was firstly increased to the desired value at the rate of 40 kPa/min. The capsule was then heated up to 773 K at the rate of 50 K/min and kept at this temperature for 10 minutes. The sample was rapidly cooled down to room temperature by switching off the heater. The pressure was finally slowly released at 40 kPa/min. A Pt/Pt-Rh thermocouple in contact with the capsule monitored the temperature during the process. Once the capsule had been removed from the multi-anvil apparatus, the product was easily recovered.

Four samples were prepared applying a pressure of 2, 4, 6 and 8 GPa. The combined use of high pressure and high temperature conditions ensured the stability of the permanently densified glass after its removal from the multi-anvil apparatus. The final product is a single glass block, as shown in figure 3.2.

The densities ρ of the samples were measured by means of the Archimedes method, using ethanol as immersion fluid. Ethanol temperature was monitored to account for its density T-dependence. The obtained density values are reported in table 3.1 as well as the densification ratio with respect to the normal silica. In the following we will refer to the samples using the densification pressure; 0 GPa indicates the non-densified glass.

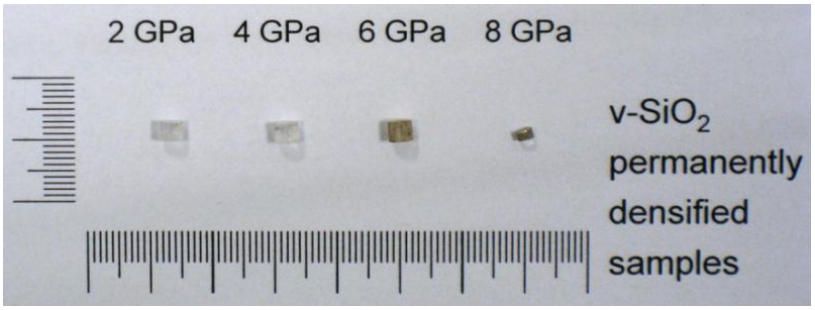

Figure 3.2: permanently densified silica samples as obtained by means of the described procedure. The dark coloration of the 6 and 8 GPa samples is due the creation of color center as a consequence of the X-ray exposure during inelastic X-ray scattering experiments.

Pressure (GPa)	Density (g/cm^3)	Densification (%)
0	2.198 ± 0.005	0
2	2.210 ± 0.005	0.6
4	2.255 ± 0.005	2.6
6	2.406 ± 0.005	9.5
8	2.67 ± 0.01	22

Table 3.1: Density and densification ratio for the permanently densified silica samples; each sample is identified by the densification pressure.

3.2 The vibrational density of states

The vibrational density of states was measured by means of Raman scattering experiments. In the case of first-order Raman scattering on a disordered system, the experimental intensity is proportional to the vibrational density of states $g(\omega)$. In the case of a Stokes process the Raman intensity is given by [74, 75]

$$I^{Exp}(\omega) = C(\omega)g(\omega)\frac{[n(\omega)+1]}{\omega}\ , \tag{3.1}$$

where $C(\omega)$ is the light to vibration coupling function and $n(\omega)$ is the Bose factor. Removing in eq. 3.1 the trivial temperature dependence given by the Bose factor and dividing by ω, we obtain the so called reduced Raman intensity

$$I(\omega) = \frac{I^{Exp}}{[n(\omega)+1]\omega} = C(\omega)\frac{g(\omega)}{\omega^2}, \tag{3.2}$$

which is directly proportional to the reduced VDOS trough the coupling function.

Room temperature Raman scattering experiments were performed using a Jobin-Yvon U1000 double monochromator and, as incident light, the 514.5 nm line of an argon ions laser. Measurements were performed both in vertical-vertical (VV) and horizontal-vertical (HV) polarization configurations. Low resolution Raman spectra were collected in the $-300 \div 1300$ cm^{-1} range. These spectra are in agreement with those already published [73, 77] and were used to adequately estimate the background contribution. The BP region has been detailed with short range - high resolution spectra. The resolution was fixed to about 2 cm^{-1}. In order to compare spectra corresponding to different densities they were normalized to the same total measured area calculated on the extended range spectra.

Figure3.3 shows the low frequency part of the depolarized Raman spectra. As the density is increased the boson peak evolution is characterized by two distinct features: the peak shifts upwards and the intensity decreases. Increasing the

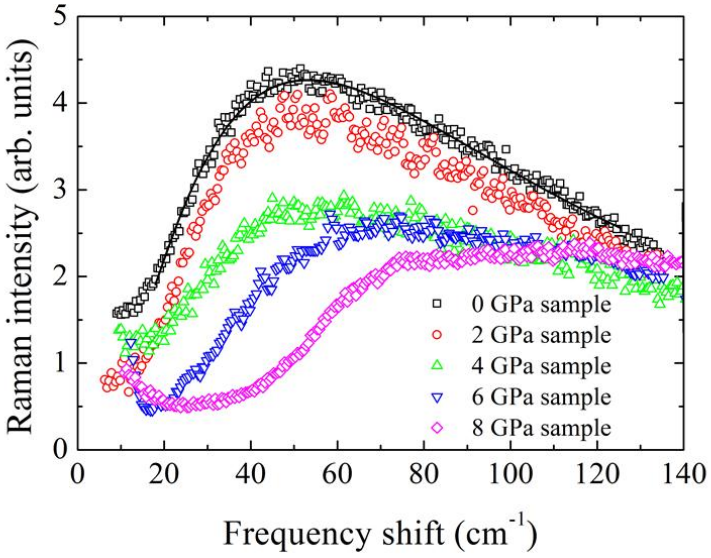

Figure 3.3: reduced Raman spectra for the normal and densified samples as reported in the legend; the continuous line represents the fit using a log-normal function defined as $I(\omega) \propto \frac{1}{\omega} \exp - \frac{(\ln(\omega/\omega_{BP}))^2}{2\sigma^2}$, where σ is the BP variance [76].

density by the 22%, we observe a peak shift of about 100% with a corresponding intensity drop of 50%. This is larger than that previously observed in sodium silicates [64] and even in vitreous germania [65]. In order to accurately determine ω_{BP}, we fitted the BP spectra using a log-normal function as indicated in figure 3.3 [76].

3.3 The boson peak shape: the squeezing procedure

Now we focus on the intensity evolution of the boson peak. We limit our analysis to normal silica 2, 4 and 6 GPa samples. To compare the shape of the peak as a function of ρ, we will perform the so called *squeezing procedure* [58]. We firstly consider the scaled frequency $\nu = \omega/\omega_S$, where ω_s is a squeezing param-

eter. Therefore we perform the variable transformation $g(\nu)d\nu = g(\omega)d\omega$. The squeezed reduced intensity $I(\nu)$ can be written as:

$$I(\nu) = I(\omega) \times \omega_s^2. \tag{3.3}$$

To derive this relation we assume that the coupling function is linear in the boson peak region. This assuption is supported by several works, *e.g.* refs. [78, 79, 80, 81].

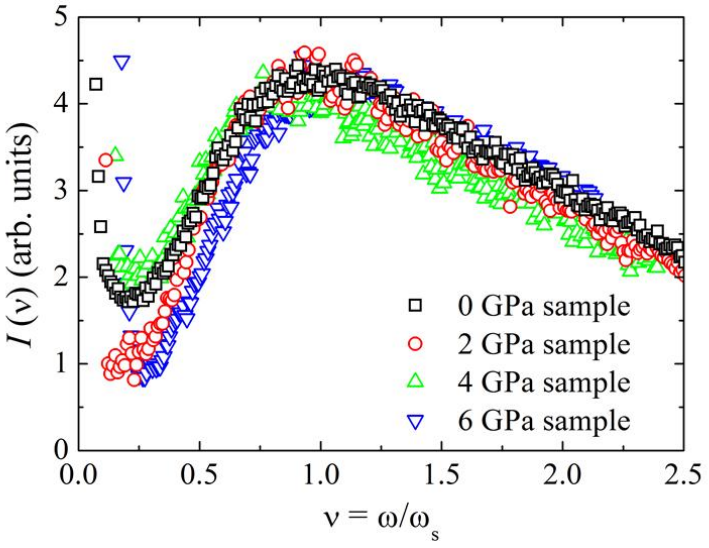

Figure 3.4: Master curve obtained using eq. 3.3 as discussed in the text.

The so-squeezed spectra are shown in figure 3.4. It is worth to note that the spectra rescale one on top of the other without any adjusting parameter. The differences visible in the low frequency tails can be ascribed to the presence of the quasi elastic scattering (QES) [58, 61]. The so obtained master curve is also expected by theoretical predictions [41].

The same result is reached if the scaling is performed directly on the reduced VDOS $g(\omega)/\omega^2$, namely dividing the reduced Raman intensity $I(\omega)$ by the coupling function $C(\omega)$. Assuming that the density dependence of $C(\omega)$ is negligible, we can use that measured in normal silica reported in ref. [79]. This

hypothesis is supported by the results obtained in densified v-GeO_2, where, in a similar densification range, it has been demonstrated that the coupling function does not depend on the sample density [82], at least in the BP region. As a matter of fact in the QES region the coupling function is almost constant and its value is system dependent (in the present case ρ-dependent) [78, 58].

Applying the procedure described before, the reduced VDOS rescales as:

$$g(\nu)/\nu^2 = [g(\omega)/\omega^2] \times \omega_s^3. \tag{3.4}$$

The result of this different procedure is reported in fig 3.4. The reduced VDOS in 3.4(a) successfully rescale on the master curve reported in 3.4(b). The discrepancies visible in the low frequency tail are due to the coupling function.

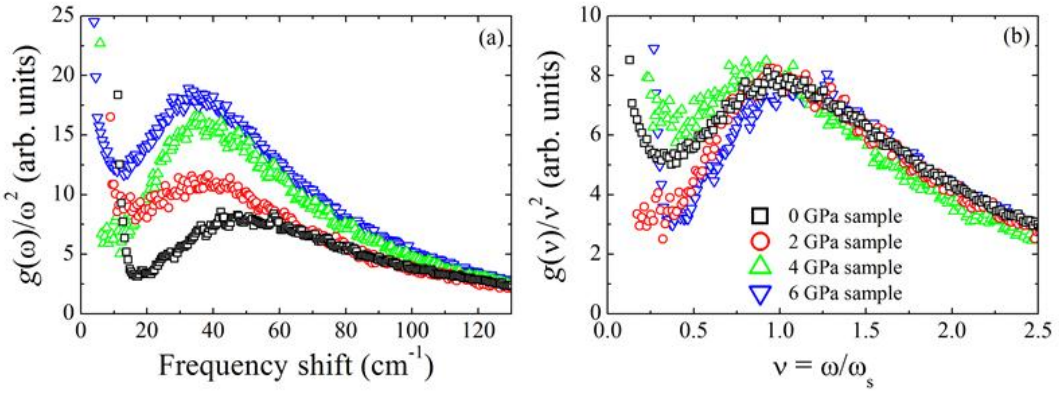

Figure 3.5: (a) Reduced vibrational density of states obtained from Raman data taking explicitly into account the coupling function reported in ref. [79]. (b) Master curve of the Boson Peak for $g(\omega)/\omega^2$

The existence of these master curves demonstrates that the BP intensity variation can be accounted for using only a single parameter ω_s. However the meaning of this parameter has not already been set. Figure 3.6 shows a comparison between the boson peak positions obtained in the present work and the positions determined by means of Inelastic neutron scattering by Inamura and co-workers [72]. Each datasets is normalized to its normal silica value. Raman

(red dots) and neutron data (black squares) show the same trend, indicating that the Raman coupling function does not induce strong modifications in the density behavior of ω_{BP}. On the same plot we report the normalized values of ω_s obtained with both the procedures (magenta diamond and green circles). In both cases we find the same behavior for the scaling factor ω_s. This gives a strong evidence of the equivalence of the two squeezing methods. Moreover, the two values of ω_s, despite of being more scattered, show a comparable density dependence as ω_{BP}. We can therefore conclude that the BP evolution in these sample is only due the peak shift. As a matter of fact the BP is better seen in $g(\omega)/\omega^2$: when the peak shifts upwards its intensities lowered by the division. The small differences between ω_{BP} and ω_s are presumably due to the fact that it is always difficult to obtain an absolute Raman intensity.

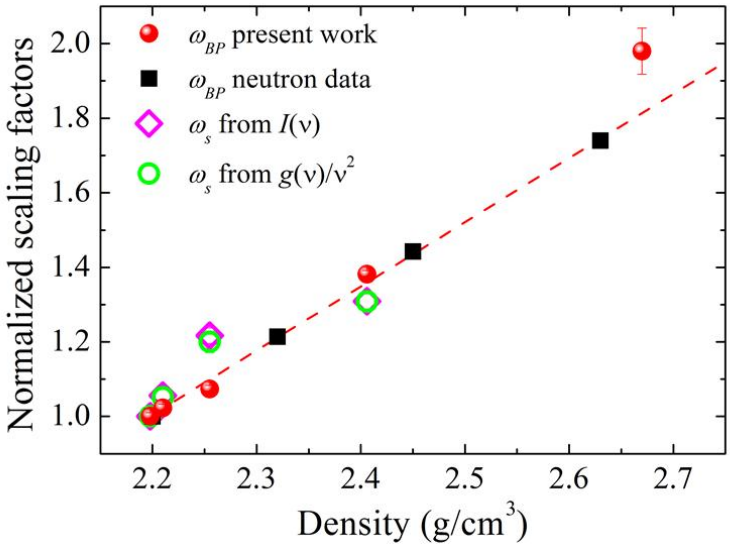

Figure 3.6: Comparison between Raman (red dots) and neutron data (black squares) from [72] and the squeezing frequency ω_S obtained squeezing $I(\omega)$ and (magenta diamond) and $g(\omega)/\omega^2$ (green circles); the red line represents the fitted density trend of the neutron data. Each data set is normalized to its normal silica value.

The squeezing procedure cannot be successfully applied to the 8 GPa sample

spectrum. As a matter of fact we do not find a ω_s which is able to scale both peak position and intensity. Figure 3.7 shows two unsuccessful tentative scalings. In fig. 3.7(a) it is reported the squeezed reduced Raman intensity $I(\nu)$ obtained using an ω_S optimized for the intensity; conversely the squeezed reduced density of states $g(\nu)/\nu^2$ is reported in fig. 3.7(b). In this case ω_S is chosen as the peak maximum. In both cases the correspondence is poor.

A similar unsuccessful squeezing has already been recognized in vitreous germania, where the difference is between the normal and the densified samples [65]. A possible explanation is that in both cases a strong modification in the packing of the local structure is induced by the densification [68] and it is reflected in the dynamical properties, directly in the VDOS or distorting the coupling function [71]. However the epoxy-amine mixture DGEBA-DETA does not show any similar behavior even if the chemical vitrification process strongly modifies the structure [67].

We can conclude that, at least in a 10% densification range, the BP peak intensity change is only due to the peak shift. Following this observation, we focus on the existence of a scaling law for the peak position.

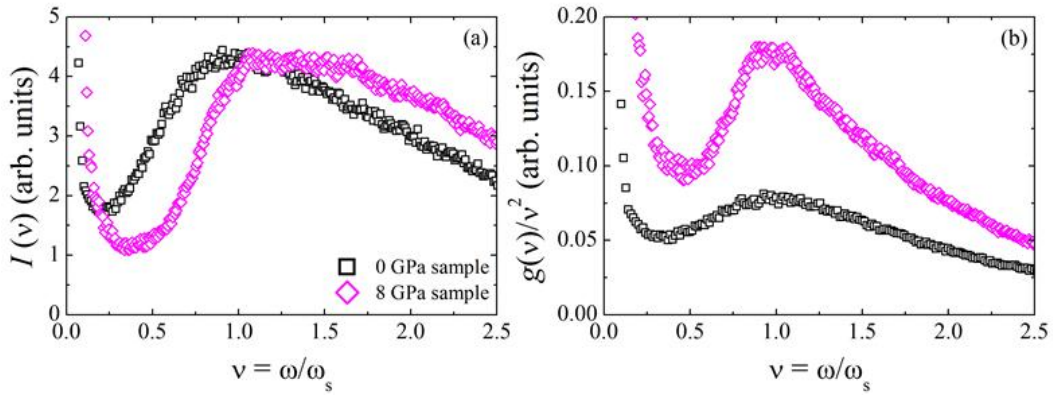

Figure 3.7: (a) tentative squeezing of the 8GPa reduced Raman intensity using an ω_S optimized for the intensity; (b) tentative scaling of the 8GPa reduced VDOS $g(\omega^2)/\omega^2$ using as squeezing parameter the boson peak position.

3.4 Elastic medium characterization in the GHz frequency range

The elastic medium can be represented by the Debye frequency ω_D introduced in 1.7.1 in the framework of the Debye theory. Equation 1.11 defines ω_D as:

$$\omega_{DB}^3 = 6\pi^2 \rho_n v_D^3, \tag{3.5}$$

where ρ_n is the number density and v_D the Debye velocity, namely:

$$\frac{3}{v_D^3} = \left(\frac{1}{v_L^3} + \frac{2}{v_T^3} \right); \tag{3.6}$$

v_D depends on both the longitudinal and transverse sound velocities, v_L and v_T. These quantities can be measured by means of Brillouin scattering experiments.

3.4.1 Brillouin light scattering experiments

Brillouin light scattering experiments were carried out using a laser with $\lambda = 514.5$ nm and a SOPRA double-pass monochromator as spectrometer. The 90° scattering geometry with no polarization analysis of the scattered light allowed us to measure both the longitudinal and the transverse acoustic modes in the same spectrum.

Figure 3.8(a) shows the evolution of the Brillouin longitudinal peak as a function of density. It can be seen that the peak position shows a minimum about 4 GPa. BLS measurements as a function of pressure, show a similar behavior between 2 and 3 GPa, roughly corresponding to our density region [83]. This softening is known as silica elastic anomaly and it is generally ascribed to a polyamorphic transition [84].

The Brillouin peak position is related to the sound velocity by the following relation:

$$v_i = \frac{\omega_i \lambda}{4\pi n_R \sin \vartheta/2}. \tag{3.7}$$

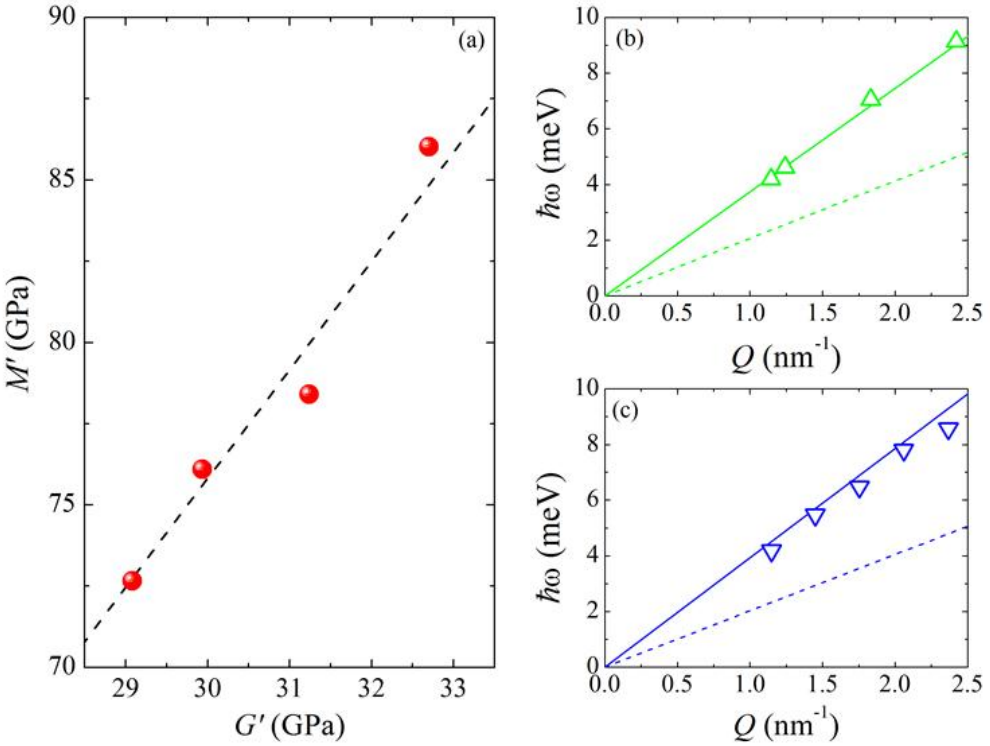

Figure 3.8: Left panel shows the longitudinal Brillouin peak evolution as a function of the increasing density, the peak intensity is normalized to its maximum. In the right panel it is reported the density evolution of the longitudinal and transverse sound velocity (respectively with blue and red bullets).

The index i labels the branches of the sound velocity v_i and the corresponding Brillouin peaks centered at ω_i; n_R is the refractive index, λ is the laser wavelength, and ϑ_s the scattering geometry The refractive index has been determined in each sample by prism coupling techniques at the experimental wavelength. Figure 3.8(b) displays the evolution of the sound velocity as a function of the density. The elastic anomaly is visible both in the longitudinal and transverse branch.

3.5 Inelastic X-ray scattering experiments

The presence of relaxations and anharmonicities can affect the sound velocity measured in the GHz frequency region [59, 67]. The sound velocity becomes frequency dependent and does no more correspond to the fully unrelaxed frequency limit needed to characterize the elastic properties of the medium. In this case we have to consider a sound velocity corresponding to higher frequency, namely moving from the visible light to X-rays, from Brillouin light scattering to inelastic X-ray scattering (IXS).

3.5.1 The X-ray spectrometer ID28

IXS measurements were carried out at the beamline ID28 at the European Synchrotron Radiation Facility in Grenoble.

The beamline lay-out is reported in [49] and it is based on the triple-axis principle. The first axis is composed of the high energy resolution monochromator fixing the incident energy E_i. The second axis is the sample goniometer, and it determinates the momentum transfer by selecting the scattering angle. Finally the third axis is the crystal analyzer which selects the scattered energy E_f. Due to the backscattering geometry the beamline is fairly long in order to acquire a sufficient beam offset between the incident photon beam from the X-ray source

and the focused very high-energy resolution beam at the sample position. The source consists of three linear undulators of 32 mm magnetic period (U32), providing X-rays linearly polarized in the horizontal plane. Typically, emission from the 3rd or 5th harmonic is utilized. This X-ray beam has an angular divergence of approximately 40×15 μrad (FWHM), a spectral bandwidth $\Delta E/E \sim 10^{-2}$, and an integrated power within this divergence of the order of 200 W. This beam is first pre-monchromated to $\Delta E/E \sim 2 \times 10^{-4}$ using a silicon (111) double crystal device kept in vacuum and at the cryogenic temperature of 110 K. Moreover, the pre-monochromator coupled with a post-monochromator act to reduce the heat load produced by the intense beam on the main monochromator. This avoids any thermal broadening of the energy resolution function. The high energy resolution backscattering monochromator consists of a flat perfect single crystal, operating at a Bragg angle of 89.98° and utilizing the silicon (nnn) reflection orders. High order Bragg reflections and perfect crystals are required in order to obtain the necessary energy resolution of $\Delta E/E \sim 10^7 \div 10^8$. The reflections are $n = 7; 8; 9; 11; 12; 13$. The Energy scans are performed by varying the temperature of the monochromator, controlled in the mK region, and keeping the temperature of the analyzer fixed. The highly monochromatic beam impinges on a toroidal mirror, focusing at the sample position to a beam size of 250 (horizontal) $\times$ 150 (vertical) mm^2 (FWHM). Once scattered by the sample, the X-rays are energy-analyzed by the analyzers. Each analyzer is composed of 12000 undistorted perfect flat crystals glued on a spherical surface. The analyzers operate in a Rowland circle geometry at the same reflection order as the main monochromator. The refocused, energy-analyzed X-rays are detected by a Peltier cooled inclined silicon diode detector. There are in fact nine independent analyzer systems with a fixed angular offset between them, mounted on a 7 m long arm that can rotate around a vertical axis through the scattering sample. This rotation allows one to choose the scattering angle Q for the nine analyzers,

and therefore the corresponding exchanged momentum, $Q = 2k_i \sin\vartheta/2$. The arm operates between 0 and 55°.

3.5.2 Experimental setup

In the present experiment, in order to get the highest energy resolution, we chose an incident beam with an energy of 23.724 keV and the silicon (12,12,12) reflection order for the main backscattering monochromator. The experimental resolution has been determined by measuring the scattering from a disordered sample (Plexiglass) at a temperature of $\sim$ 13 K and at a Q-transfer corresponding to the first maximum of its static structure factor (10 nm^{-1}). In this way the elastic contribution to the scattering is maximized. The overall energy resolution of the spectrometer was $\sim$ 1.3 meV (FWHM), depending on the analyzer crystal.

To increase the population of the acoustic excitation, and therefore the inelastic signal, measurement were performed at $T = 573$ K putting the sample in an evacuated fournace.

Since we are interested in determine the longitudinal sound velocity in the purely elastic limit we focused in low exchanged momentum range, collecting spectra between 1.1 and 2.5 nm^{-1}. Each spectrum was acquired in the $-35 \div +35$ meV energy range; in the central part ($-25 \div +25$ meV) the energy step was 0.25 meV whereas the step was 0.5 meV in the tails. Moreover to improve the statistical accuracy of the data we acquire at least four spectra for each Q, averaging the results. The total integration time is about 24 hours for each spectrum.

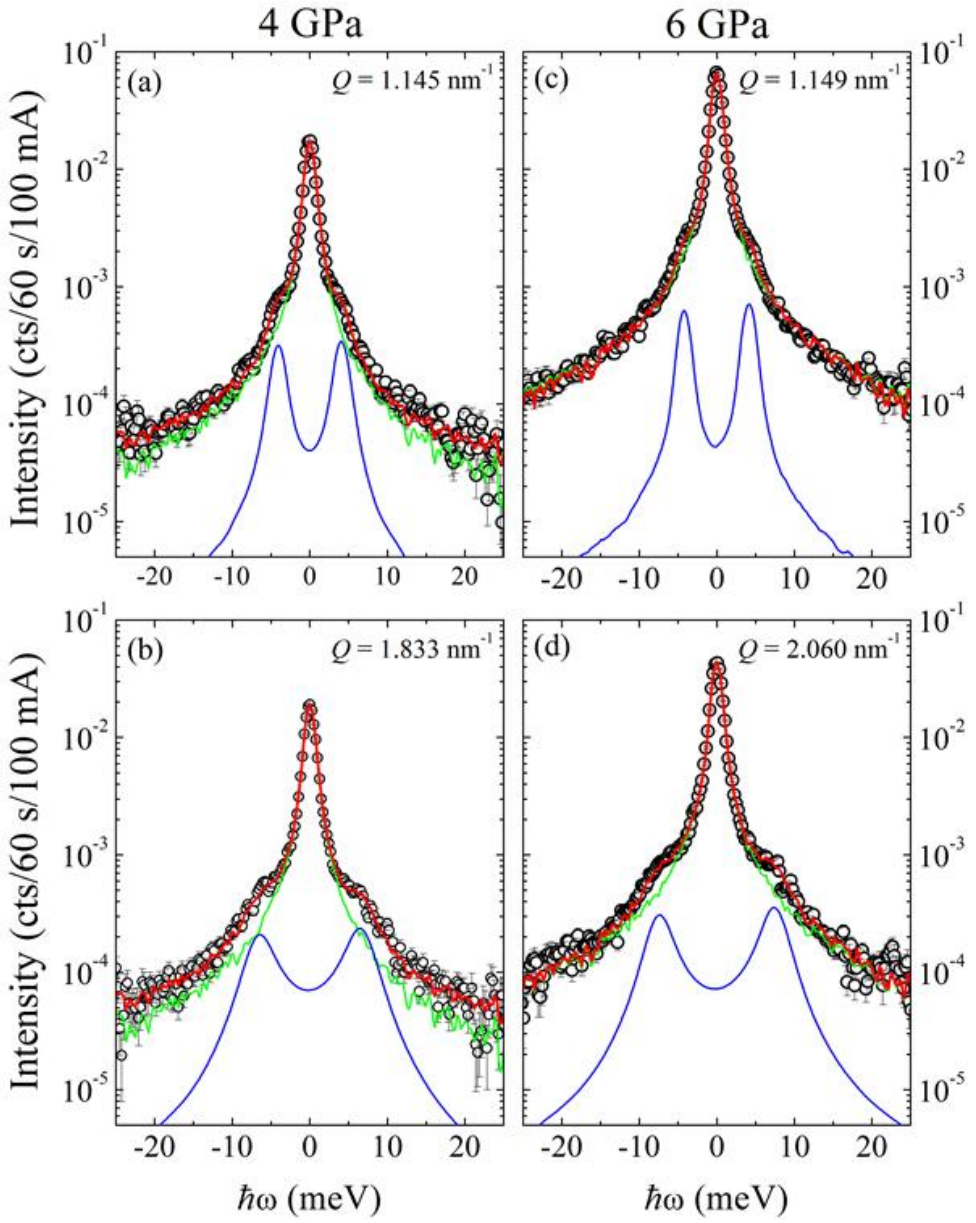

Figure 3.9: Representative IXS spectrum on the analyzed samples measured at $T = 573$ K at selected Q (black circles); left pannels refers to the 4 GPa sample whereas the right ones to the 6 GPa sample. The measured instrumental resolution is also reported (green line). The red line is the best fit of the data and the blue line is the inelastic contribution.

3.5.3 IXS data analysis

Figure 3.9 shows a selection of spectra collected at selected values of the exchanged momentum Q. Spectra were acquired on the 4 GPa sample, fig. 3.9(a) and (b), and on the 6 GPa sample, fig. 3.9(c) and (d). Spectra are composed by an elastic peak and two inelastic features corresponding to the Stokes and anti-Stokes components of the Brillouin doublet and thus related to the acoustic-like modes. Increasing Q, the doublet shifts toward higher energies and becomes broader.

The measured intensity in IXS experiment can be written as the convolution between the dynamic structure factor $S(Q,\omega)$ and the resolution function $R(\omega)$, namely:

$$I_{IXS}(Q,\omega) = I_0(Q)\, R(\omega) \otimes \left\{ \frac{\hbar\omega}{K_B T} \left[n(\omega,T) + 1 \right] S(Q,\omega) \right\} + bkg, \qquad (3.8)$$

$n(\hbar\omega)$ is the Bose factor, the term $[n(\omega,T)+1]\,\hbar\omega/K_B T$ accounts for the quantum nature of the interaction and fulfills the detailed balance principle. The baseline term is added in order to take into account the electronic background of the detector and the environmental background. Moreover, the overall intensity factor $I_0(Q)$ is a normalization factor which is influenced by the atomic form factors, the efficiency of the analyzers, and by all other angle-dependent instrumental correction factors. In principle data can be reported in absolute unit [85], but this is irrelevant in the present discussion.

The dynamic structure factor $S(Q,\omega)$ can be modeled as the sum of a delta function to describe the elastic line and a damped harmonic oscillator (DHO) for the inelastic component:

$$S(Q,\omega) = A_{el}(Q)\,\delta\omega + A_2(Q)\,\frac{1}{\pi}\frac{\Omega(Q)^2\,\Gamma(Q)}{\left(\omega^2 - \Omega(Q)^2\right)^2 + \omega^2\Gamma(Q)^2}. \qquad (3.9)$$

where A_{el} describes the intensity of the elastic component whereas A_1, Ω, and Γ refer to the inelastic propagating excitations and they respectively represent the

intensity, position and attenuation. Examples of this fit procedure are reported in figure 3.9. The best fitting line shape obtained using eq. 3.8 is indicated with a red line. The experimental resolution is depicted with a green line and the DHO contribution corresponding to the inelastic features with a blue one.

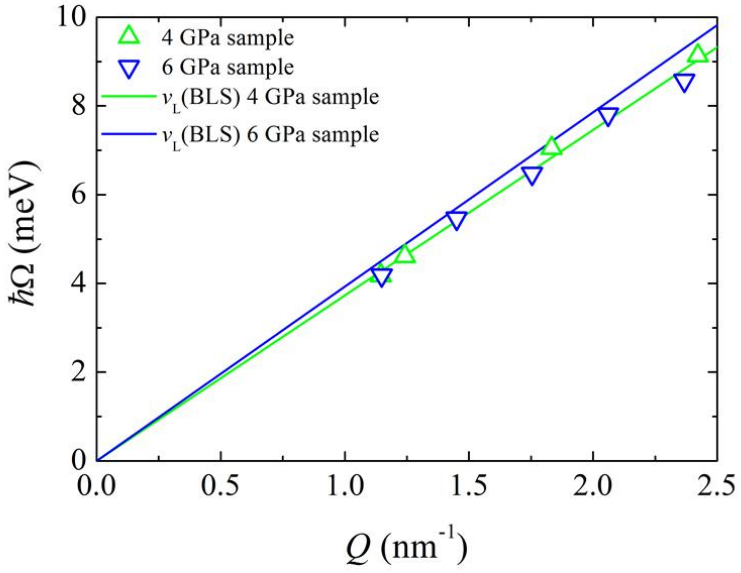

Figure 3.10: Dispersion curve for 4 GPa sample (green up triangles) and for the 6 GPa one (blu down triangle). The dashed line is the extrapolation of the BLS sound velocity.

The obtained dispersion curves of the two samples are displayed in fig. 3.10. The dashed lines are the extrapolation of the low frequency sound velocities measured by BLS. IXS and BLS sound velocities are in good agreement, even if the THz data are slightly lower than the GHz ones. This small difference could be ascribed to the presence of a softening of the modes in the low-Q region, around the BP frequency, as it has been recently shown in other glassy systems [86].

3.6 The end of the story - The breakdown of the Debye scaling

The calculation of the Debye frequency ω_D in the case of BLS data is a straightforward application of eq. 1.11. As a matter of fact v_L and v_T are both measured.

In the purely elastic limit we can measure only one mode, corresponding to the longitudinal one. However the transverse sound velocity can be estimated using the Cauchy-like relation connecting the high frequency limit of the longitudinal elastic modulus $M' = \rho v_L^2$ and the shear one $G' = \rho v_T^2$. The relation reads:

$$M' = A + BG'. \tag{3.10}$$

This has been recently found to hold for a great variety of systems at all frequencies [87] with $B \sim 3$ and A a system dependent constant. The bulk moduli G' and M' calculated using BLS sound velocity values are reported in figure 3.11(a). Data shows again a linear behavior with a slope $B = 3.3 \pm 0.7$. This confirms the applicability of the Cauchy relation and allows the determination of the high frequency transverse sound velocity and then the appropriate Debye frequency. Figures 3.11(b) and (c) show the estimated transverse branches (dashed lines).

In order to check whether the shift of the Boson Peak can be totally ascribed to changes in the elastic constants, we can compare the dependence of ω_{BP} and ω_D on the same plot, figure 3.12. Data are normalized to their normal density value. As in fig 3.6 we show the BP position obtained by both Raman and neutron inelastic scattering [72] data. Blue and cyan diamonds represents the elastic continuum, *i.e.* the Debye frequency ω_D, obtained using respectively IXS and BLS data. The two values agree very well. The density dependence of ω_{BP} and ω_{DB} is roughly linear, though with slopes about one order of magnitude

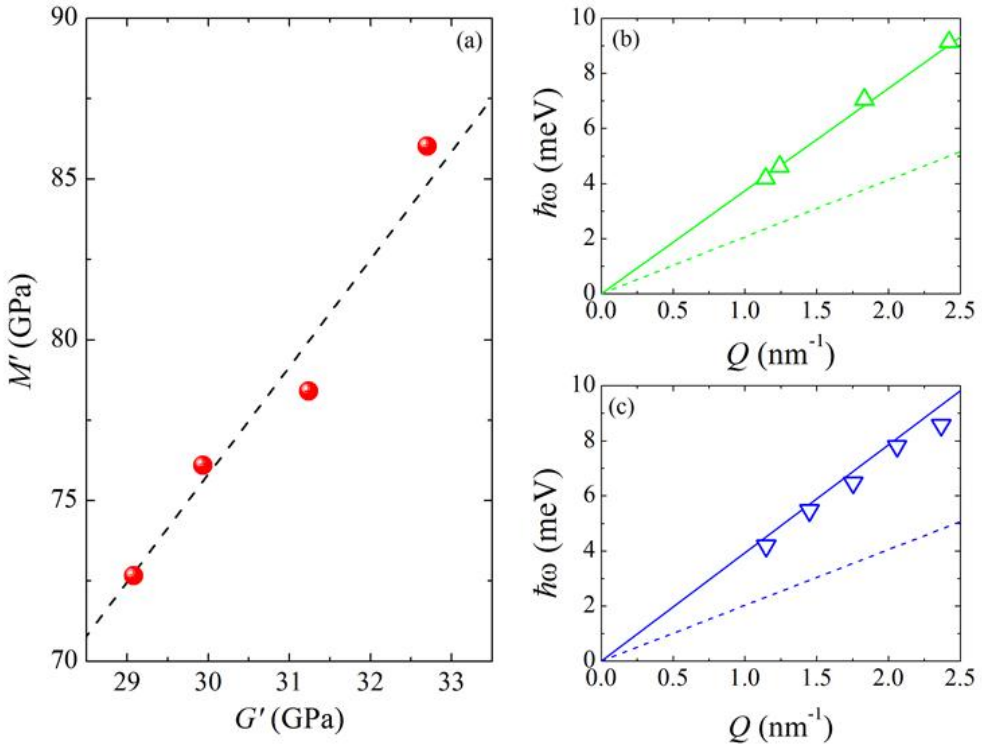

Figure 3.11: (a) Application of the Cauchy generalized relation using densified silica bulk moduli calculated by BLS data; (b) and (c) dispersion relations for the 4GPa and 6GPa sample; open up and down triangles are experimental values, the solid line is the extrapolated BLS longitudinal sound velocity and the dashed line the transverse sound velocity obtained using eq. 3.10.

different. This result clearly demonstrates that the elastic medium transformations cannot account for the BP shift. The boson peak shows a stronger than Debye evolution with ρ.

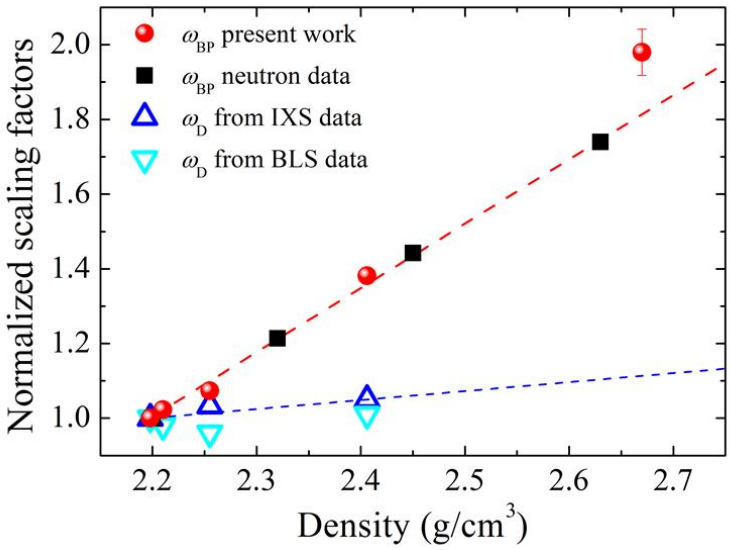

Figure 3.12: Comparison between ω_{BP} and ω_D; red bullets correspond to the Boson Peak frequency as function of density obtained from Raman spectra; black squares to the corresponding data obtained using neutron scattering [72]. Cyan down-triangles: Debye frequency calculated using BLS sound velocities; blue up-triangles: Debye frequency calculated using the IXS sound velocity.

To conclude, we add a new proof that the scaling of the BP with the continuum elastic medium properties represented by the Debye frequency is not a universal feature of disordered materials. This confirm that the Debye scaling does not cover the full story and we have to look for new mechanisms to explain the density evolution of the Boson Peak in vitreous silica.

We also highlight that the BP shape is invariant but only in a limited range of density, namely only if *something new* does not happen. Raman data allow two possible competing explanation: the densification induces a direct change in the vibrational density of states $g(\omega)$ or causes a distortion of the coupling function

which is no longer density independent. A definitive answer to this question can rise only measuring the vibrational density of states. Suitable techniques are inelastic neutron scattering o inelastic X-ray scattering.

Chapter 4

Medium range order and voids in permanently densified vitreous silica

Natura abhorret vacuum.
Plutarchus

In the previous chapter we have dealt with the problem of the densification effects, considering them mainly from a dynamical point of view. Now we focus on the structural transformation occurring in vitreous silica when the density is increased.

Since the pioneering work of Zachariasen [11], the structure of vitreous SiO_2 has been object of several experimental and simulative studies [17]. The short range order is well characterized [12]. The structural building block is the well defined $Si\left(O_{1/2}\right)_4$ tetrahedron [12, 17]. These tetrahedra link together to form a tridimensional topological disordered network of corner sharing units. Diffraction data show the presence of the so-called first sharp diffraction peak, which is considered as the signature of the existence of an order beyond the short range,

namely an order in the tetrahedra connections.

In this chapter we will characterize a prominent feature of the SiO_2 network, *i.e.* the presence of void space inside the tetrahedral arrangement. These cages have been analyzed by means of the positron annihilation lifetime spectroscopy (PALS). It allows an *in-situ* characterization of the defects implanting positrons in matter and measuring the time elapsing between implantation and annihilation [88, 89, 90, 91]. The PALS technique is a well established method for the characterization of defects in technological materials but it represents a new approach for directly accessing to structural information.

The so-obtained data will be discussed together with diffraction data [72] to account for the densification induced structure evolution in v-SiO_2 [92]. Void spaces will be analyzed also as a key feature of the medium range length-scale, highlighting their contribution to the first sharp diffraction peak [93, 21, 18]. Moreover, we present a preliminary analysis of the relation between these medium range features and the boson peak.

4.1 Positrons and positronium

The positron is the anti particle of the electron. Positrons (e^+) and electrons (e^-) share the same physical properties except for the electric charge and the magnetic moment, which are opposite. The main properties of positrons are reported in table 4.1.

The existence of positrons was theoretically predicted by Dirac in 1928 as the negative energy extension of his theory of electron energy levels. Few years later, in 1932, Anderson, studying cosmic rays using a cloud chamber, identified the trace of a *positive charged electron*. This particle was named *positron* and it was the first evidence of the existence of the antimatter.

In general, positrons annihilate with electrons, predominantely via 2γ-rays

mass	510.998928(11) keV/c^2
spin	1/2
electric charge	$+1.602176565(35)\times10^{-19}$ C
magnetic moment	$+1.00115965218076(27)\mu_B$
lifetime	$>2\times10^{21}$ yrs

Table 4.1: Properties of the positrons; $\mu_B = e\hbar/2m_e$ is the Bohr magneton and its value is $9.27400915(23)\times10^{-24}$ J/T. Data are from ref. [94].

decay. However, in some circumstances a positron can bind with an electron, forming an hydrogen-like atom, called *positronium* (Ps) [95]. Differently from hydrogen, positronium can be depicted as two equal mass particles orbitating around a common center. The Ps energy levels can be calculated using the Bohr formula

$$E_0 = \frac{\alpha^2 mc^2}{2n^2}, \tag{4.1}$$

where α is the electromagnetic coupling constant and $m = m_e/2$ is the reduced mass, with m_e the electron rest mass. The positronium ground state binding energy is thus 6.8 meV, one half of the hydrogen one. The mean separation between the two particles is given by the Bohr radius, namely

$$r_{Ps} = \frac{\hbar c}{\alpha^2 mc^2} = 1.06\text{Å}, \tag{4.2}$$

which is twice the Bohr radius in the hydrogen case.

The ground state of the positronium has two possible configurations:

- singlet $^1S_0$ state, para-positronium (p-Ps), with total spin $S = 0$ and $m_s = 0$;
- triplet $^3S_0$ state, ortho-positronium (o-Ps), with total spin $S = 1$ and $m_s = 0, \pm1$.

Since e^+ and e^- annihilate, positronium has a finite lifetime. In particular the two states have different vacuum mean lifetimes and decay channels. The selection rule prescribed by the charge conjugation invariance for the Ps annihilation is

$$(-1)^{l+s} = (-1)^n \,. \tag{4.3}$$

The left side is the charge conjugation number for positronium with angular momentum l and total spin s. The right side is the charge conjugation number for n photons. Moreover, the conservation of energy and momentum forbids the single photon 1γ annihilation process for free Ps. Therefore, p-Ps decay via even (two) γ-rays, with a lifetime $\tau_{p\text{-Ps}} = 125$ ps (in vacuum). The ortho Ps has a longer life, $\tau_{o\text{-Ps}} = 142$ ns, and it decays into odd (three) γ-rays. The relative ammount of ortho and para-positronium is, in absence of external distrubances, 3:1.

4.2 Positrons in solids

In this section we will briefly review the *life* of a positron implanted into a material with an energy $E_i \sim$ keV. This life can be divided into three main stages. The first stage is the slowing down and the thermalization, the second stage is the diffusion and perhaps the trapping, whereas the latter is, obviously, the annihilation [89, 88, 91, 90]. Focusing only on positron inside the material we neglect surface effects and the reemission of positron or positronium from a surface [89, 88].

After its introductions into the solid the energetic positron interacts with the atoms of the medium loosing energy. The energy-loss channels are strictly dependent on the nature of the material.

In metals, the primary channel is the ionization. Core electron excitation

hands over to plasmons and finally to electron-hole pair formation. These processes are very effective and they last until the energy falls below a few tenths of eV, where phonons scattering dominates. Positrons reach the thermal equilibrium in $\sim 10^{13}$ s.

In intrinsic semiconductors, similar energy-loss channels occur but they are active only until the energy is greater than the band gap energy E_g. At this point the thermalization slows down since single inelastic phonon scattering events are inefficient whereas multiple phonon scattering ones are very rare.

For insulator the situation is almost the same as for semiconductors, however there is a further energy-loss channel to count. As a matter of fact positrons can also continue to thermalize below the band gap energy forming positronium. Forming Ps an e^+-e^- pair gains $E_{Ps} = 6.8$ eV. If the positron energy E is contained in the region $E_g - E_{Ps} < E < E_g$, it is energetically possible to excite an electron from the valence band. For energies below $E_g - E_{Ps}$ the ionization of an electron and the formation of positronium are not possible. At the same time, if $E > E_g$, electron-hole pair formation is much more likely than positronium formation. The energy region where Ps formation is the only available energy loss mechanism is called the *Ore gap*. In metals and in semiconductors, positrons cannot form positronium because the high electron density screens the Coulomb interaction between positrons and electrons. Moreover, Ps can be formed via the so called *spur* mechanism. As a matter of fact, as positron thermalizes it leaves a trail of ionized electrons, the spur. Once the positron is thermalized it can form positronium binding with one e^- in the terminal spur.

Between the time of thermalization ($\sim 10^{-12}$ s) and the time of annihilation ($\sim 10^{-10}$ s), the positron exists in insulators in both free and bound states. During this time, e^+ and Ps have a thermal energy $\sim K_B T$ and they diffuse through the material. Their deBroglie wavelength at room temperature is on the order of 10^2 Å, greater than the typical interatomic distances. Where a

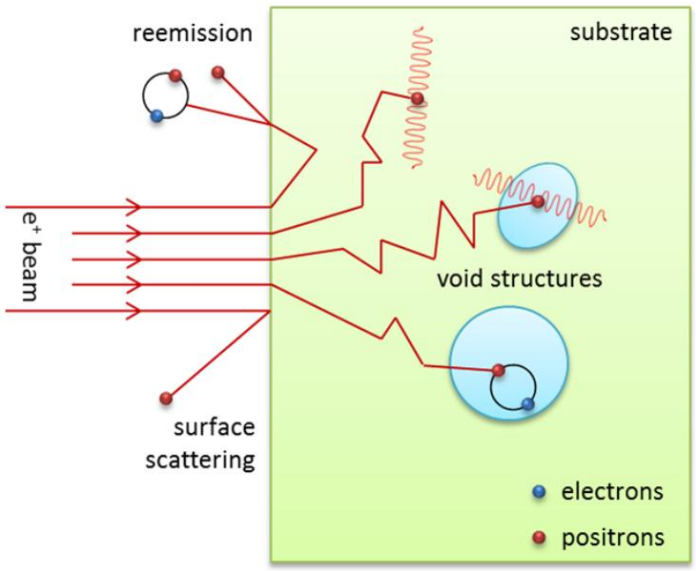

Figure 4.1: Schematic representation of the interaction between positrons and condensed matter.

percentage of free-volume exist at a size a few Ångstroms, both thermalized positrons and Ps have sufficient chance to sense the existence of such holes. Positrons and positronium are energetically more stable in the voids than in the bulk, where they sense the core strong repulsive potential between the ion core and the positively charged positron or the highly polarizable Ps.

The final fate of an implanted positron, free or bound, trapped or diffusing, is eventually to a approach an electron at a dangerously close distance and to be annihilated [90].

The lifetime of the positronium confined in voids will depend on two factors: the intrinsecal *p*-Ps or *o*-Ps lifetime, and the probability of a *pick-off* annihilation. In principle the *o*-Ps life in vacuum (or in voids) is up to three order of magnitude greater than the other e^+ states in materials. In fact the *o*-Ps trapped in voids explore the voids volume and annihilates with an electron of the surrounding atoms clouds. This process is called pick-off annihilation and its rate is proportional to the overlap between the e^+ and e^- wavefunctions,

hence to the void volume.

The typical lifetimes of the positronic processes in solids are resumed in table 4.2.

e^+ lifetime in vacuum	$\sim 2 \times 10^{22}$ yrs
e^+ scattering and diffraction	$\sim 10^{-15}$ s
e^+ thermalization (to $\sim \varepsilon_F$)	$\sim 10^{-13}$ s
e^+ thermalization (to $\sim \frac{3}{2} K_B T$)	$\sim 10^{-12}$ s
e^+ trapping after thermalization	$\sim 10^{-15}$ s
e^+ lifetime freely diffusive	$\sim 1 \times 10^{-10}$ s
e^+ lifetime void trapped	$\sim 3 \times 10^{-10}$ s
p-Ps lifetime in vacuum	$\sim 1.28 \times 10^{-10}$ s
o-Ps lifetime in vacuum	$\sim 1.42 \times 10^{-7}$ s
o-Ps lifetime trapped in voids	$\lesssim 10^{-9}$ s

Table 4.2: Timescales characterizin the fate of an implanted positron [89].

4.3 Positron Annihilation Lifetime Spectroscopy

The study of the lifetime of o-Ps in solids can give insights on the nature of the material, in particular on the presence of trapping defects such as pores and void spaces. This is the main task of the Positron lifetime Annihilation Spectroscopy (PALS). In a typical PALS experiment the relevant quantity is the elapsing time from the implantation of the positron and its annihilation determined through the detection of the annihilation γ-rays.

PALS measurements were performed at Pulsed Low Energy Positron System (PLEPS) which is coupled to the positron surce NEPOMUC, NEutron-induced POsitron source MUniCh. These instruments are located at the research reactor *Heinz Maier-Leibnitz* FRMII of the Technische Universität München.

4.3.1 The positron source NEPOMUC

The positron source NEPOMUC creates a positron beam exploiting the pair production mechanism, *i.e.* the creation of a e^+-e^- pairs by materialization of high energy gamma rays in the electric field generated by the nuclei of a converter materials. The energy threshold of this process is $E_\gamma > 2m_e c^2$.

A cascade of high energy γ's is produced through a thermal neutron capture process. The reactive material is cadmium which has an huge neutron absorption cross section in the thermal region ($\sigma_{abs}^{Cd} = 20600$ barn) The capture reaction $^{113}\mathrm{Cd}\,(n,\gamma)^{114}\,\mathrm{Cd}$ relases an energy of 9.05 MeV per neutron. On a average, for each captured neutron 2.3 γ's are produced with $\langle E_\gamma \rangle = 1.5$ MeV. Since the pair production cross section is approximately proportional to Z^2, materials with high nuclear charge Z are preferable. The NEPOMUC converter is composed by platinum (Z=78) foils which are also used to moderate the produced beam [96].

The e^+ source is mounted inside the reactor moderator tank, close to the pile core. The Pt converter is surrounded by a cadmium cap which operates as gamma rays source as well as shielding material. The thermal load is dissipated into the reactor heavy water pool. Positrons are produced and moderated into the Pt foils, then they are accelerated using high voltages. At 1 keV the source yields 9×10^8 positron per second collimated in a 7 mm (FWHM) beam in a longitudinal magnetic guiding field of 6 mT. To clean the beam, eliminating the γ and fast neutrons background, the e^+ are bended three times in the biological shield.

The brightness of the positron source is improved by a positron remoderator based on a tungsten single crystal in back-reflection geometry. The energy of the remoderated beam can be adjusted between 20 and 200 eV. The total efficiency of the setup is about 5%.

4.3.2 The positron lifetime spectrometer PLEPS

The positron source NEPOMUC provides a continuous beam, but it is not suitable for positron annihilation lifetime (PAL) measurements. As a matter of fact the measure of the lifetime needs a perfect knowledge of the implantation time of every single positron, hence it is required a monochromatic beam with a periodic structure. To produce this structure there are two techniques: chopping and bunching. In general, the chopper blanks out the beam, causing an intensity loss. On the other hand, bunchers exploit electric field to accelerate or decelerate charged particles to obtain a time focus somewhere in the space, but loosing the monochromaticy. However, the combined use of these techniques can compensate these disadvantages [97]. PLEPS pulsing section is thus composed by a prebuncher, a chopper, and a buncher. These devices operate at a frequency of 50 MHz to produce at a given point in time within the time window of 20 ns a sharp pulse of 150 ps (FWHM), ensuring between two pulses a low background noise at the sample location. In "PLEPS words" pulse means that one out of 100 pulses will contain at most one positron and only one out of 10^5 will contain more than one e^+. The other pulses are blanks. This allows to have only one positron at the time in the sample [98].

The sharp pulse is thus accelerated to a desired implantation energy between 0.2 keV and 22 keV. Positrons impinge on the sample, undergoing to the processes described in sec 4.2. After the annihilation, γ's are detected by a BeF_2 scintillator coupled to a photomultiplier. A Wienn filter and a field-free Faraday cage are used to remove scattered positrons which can introduce a spurious background. The entire apparatus works in high-vacuum conditions.

4.3.3 Experimental setup

PALS experiments were performed on all the permanently densified silica samples and in a normal silica one. Samples were glued to an ultra-pure golden foil. This metallic substrate was chosen in order to provide a good lifetime-contrast between sample and substrate annihilations.

PALS is an *in-situ* technique. As already discussed in sec. 4.2, positrons implanted in the matter lose their energy until the thermalization is reached. The implantation depth $\langle z \rangle$ is the depth at which positrons or positronium end the slowing down and start their diffusive motions. According to a Makhovian implantation profile the implantation depth can be written as

$$\langle z \rangle \, [nm] = \frac{40}{\rho \, [g/cm^3]} E_i^{1.6} \, [keV] \, , \tag{4.4}$$

where ρ is the density [89].

The PALS experiments were performed with two implantation energies, 16 and 18 keV. The implantation depths calculated for our samples using eq. 4.4 are reported in figure 4.2. It can be seen that $\langle z \rangle \, (E_i = 16$ keV) ranges from 1.56 μm to 1.26 μm whereas $\langle z \rangle \, (E_i = 18$ keV) goes from 1.86 μm to 1.52 μm. These $\langle z \rangle$ values ensure that we are probing the bulk properties of our samples.

4.4 Positron Lifetime Spectra

PALS experimental observable is the time between the implantation and the annihilation. By accumulating typically several millions of annihilation events one obtains an exponential decay spectrum.

Figure 4.3 shows the PALS spectra measured in the densified samples and in normal silica using the two implantation energy. The typical PAL spectrum is formed by a prompt peak due to fast events and a long tail related to long living particles. Figure 4.3 shows that, increasing the density, the long time tail

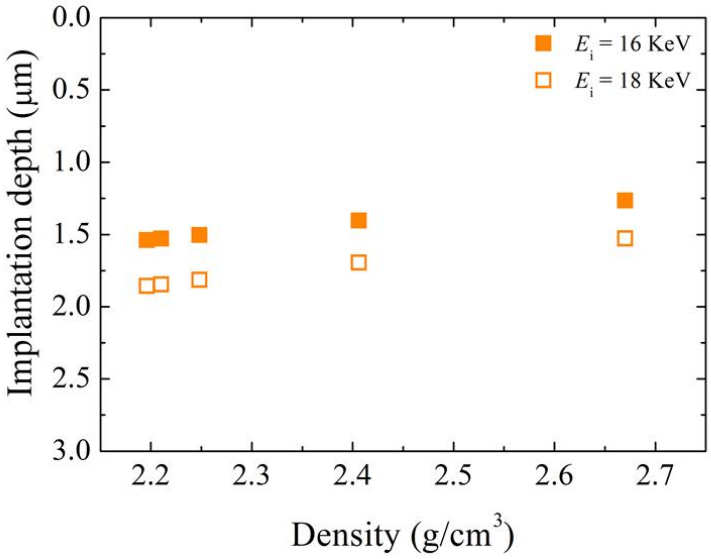

Figure 4.2: Implantation depths for the two selected energies, 16 keV (full orange squares) and 18 keV (open orange squares).

of the spectrum decreases. Moreover, comparing spectra at the same density but different energy *i.e.* at different depth, figure 4.4, they appear identical. This indicates that the samples are microscopically homogeneous.

The measured PAL spectrum $Z(t)$ can be viewed as the sum of N exponential decay lifetime components convoluted with an instrumental resolution function $R(t)$ superimposed to a constant background bkg:

$$Z(t) = R(t) \otimes \sum_{i}^{N} \frac{I_i}{\tau_i} exp(-t/\tau_i) + bkg, \tag{4.5}$$

where τ_i and I_i indicates the lifetime and the intensity associated to the state i.

The instrumental resolution $R(t)$ is determined by measuring a PALS spectra on a reference substance, in this case a p-type silicon carbide slab. This shows a bulk lifetime $\tau_{bulk} = 345$ ps and a surface lifetime $\tau_{surf} = 145$ ps. Using eq. 4.5 and performing a reverse lifetime analysis the time resolution function $R(t)$ can be retrieved.

As already noted, spectra corresponding to different E_i are indistinguishable,

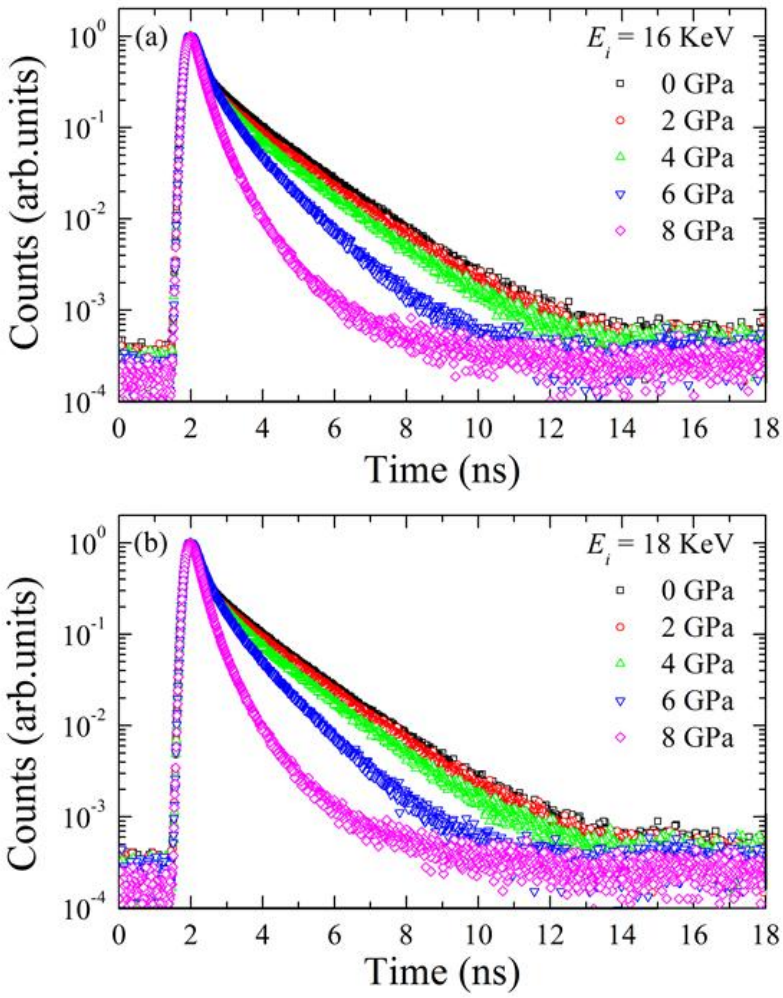

Figure 4.3: Positron annhilation lifetime spectra measured in normal and densified silica samples as reported in the legend. Spectra are obtained implanting positrons with $E_i = 16$, (a), and $E_i = 18$ keV (b).

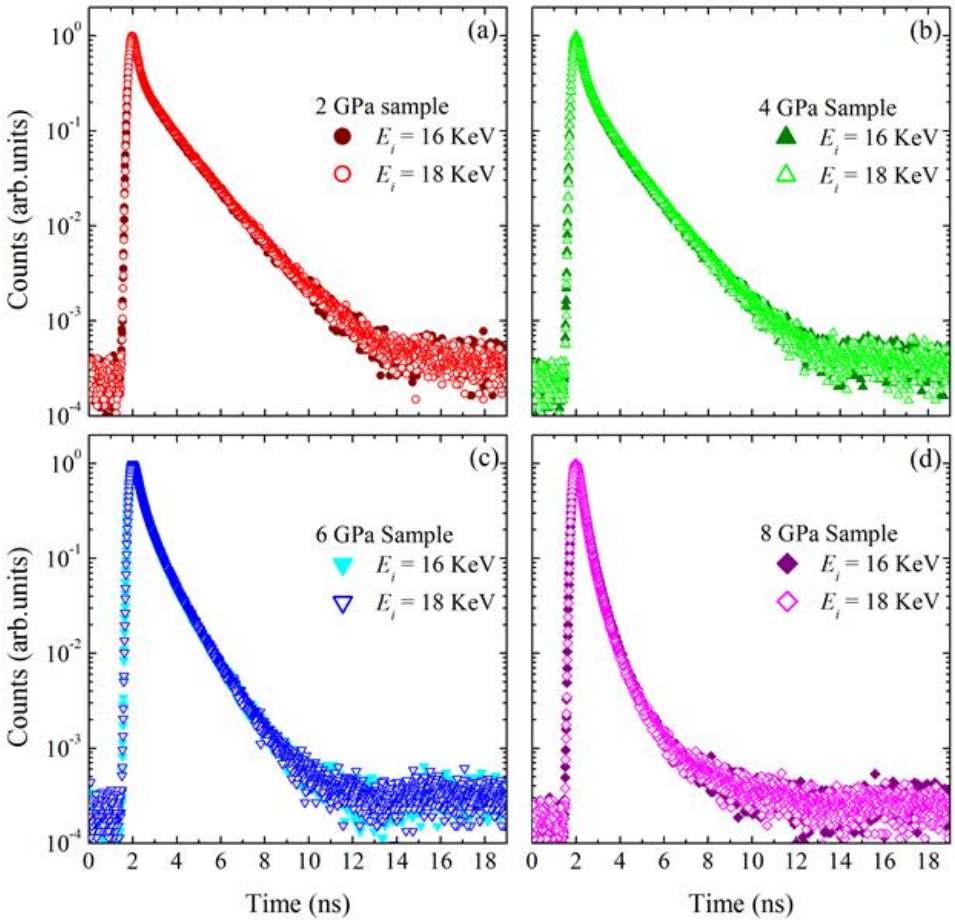

Figure 4.4: Comparison between PALS spectra measured with different implantation energies: $E_i = 16$ keV (full symbols) and $E_i = 18$ keV (open symbols); PAL spectra are measured in the samples densified at 2 (a), 4 (b), 6 (c), and 8 GPa (d).

see 4.4. In the quantitative analysis they were averaged and then analyzed using the program POSITRONFIT [99] in order to determine the lifetime τ_i and the intensity I_i of the N decaying components in eq. 4.5.

The decomposition of the 0, 2 and 4 GPa spectra shows the existence of $N = 3$ components. On the other hand in the 8 GPa case in order to obtain a good fit it is necessary to consider a fourth lifetime τ_4 which has a small but non neglegible intensity I_4. The 6 GPa sample is the intermediate case where we can obtain a satisfactory decomposition either with three or four components (reduced χ^2 close to 1). As a matter of fact, the fourth component is very small and the other lives are scarcely affected by its introduction. The so obtained parameter τ_i and I_i are reported in figure 4.5.

The first component is characterized by a $\tau_1 \simeq 160$ ps and $I_1 = 25\%$. This fast decaying life is associated to the prompt p-Ps self-annihilation and/or free e^+ annihilation. Both the lifetime and the intensity, figure 4.5(a) and (b), are almost constant increasing the density; an increase of I_1 is visible only in the most densified sample.

The second life is characterized by τ_2 which increasing the density decreases from ~ 0.73 ns to ~ 0.36 ns. The intensity I_2 doubles. This lifetime is associated with the annihilation of trapped positron with oxygen atoms around pores and that do not form Ps [100].

The most interesting lifetime is τ_3 which is associated with the pick-off annihilation of o-Ps in voids. Increasing the density this lifetime is cut by half. Moreover the intensity I_3 decreases from the 55% to 13%. In the two most densified sample (6 and 8 GPa) a further lifetime emerges. This fourth component has a rather constant long life and a very low intensity $I_4 \lesssim 1\%$. This life is limked to the annihilation of o-Ps and it could account for the existence of larger voids or internal cracks originated by the densification process.

The overall picture that PALS data suggest is that in the available void

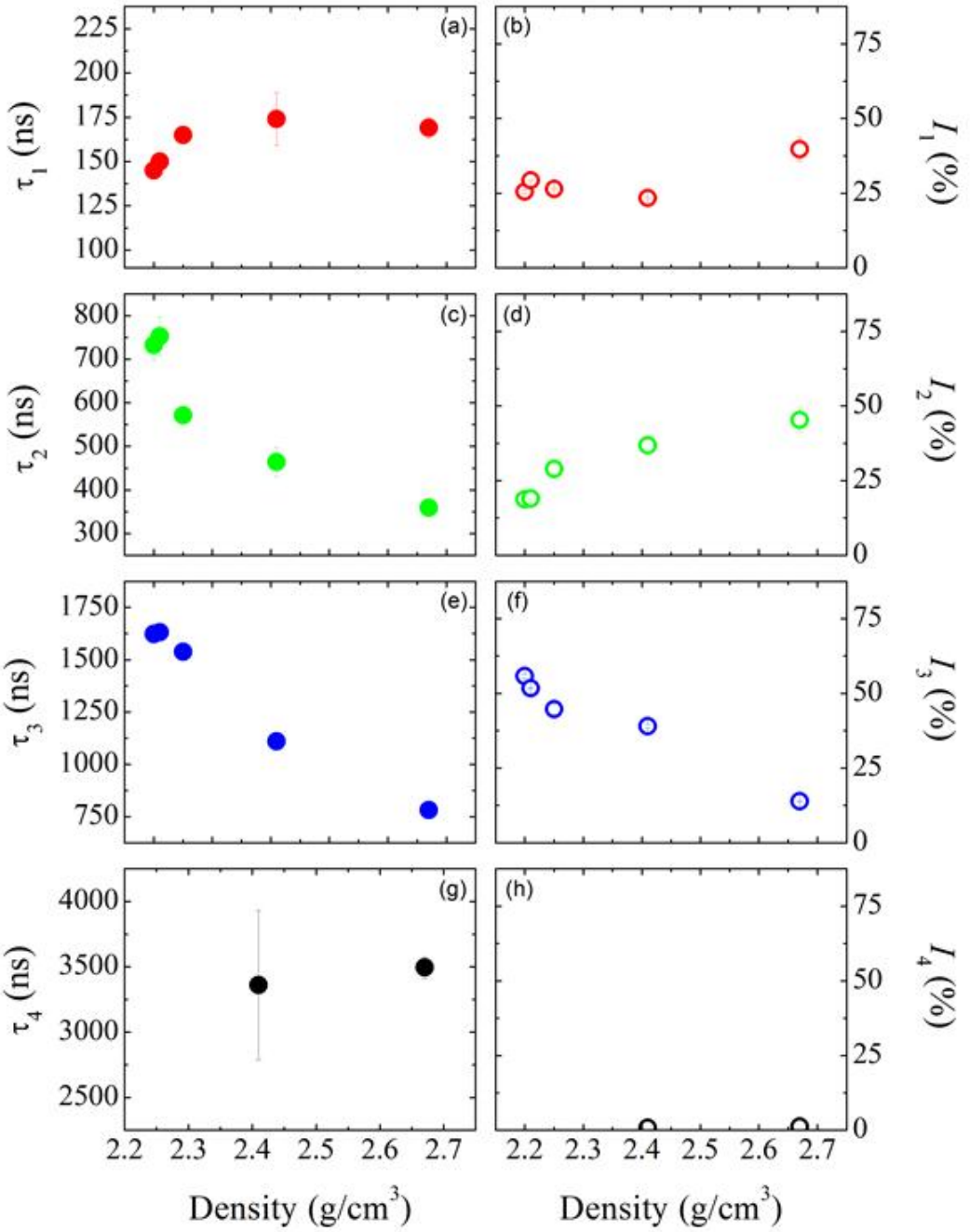

Figure 4.5: PALS fit parameter obtained using eq. 4.5.

volume is strongly reduce by the densification procedure. The annihilation time of free e^+ and p-Ps is basically unaffected and eventually the probability of these annihilation raises with density. On the other hand the lifetimes due to trapped particles, τ_2 and τ_3 shows a drop indicating an increase of the pick-off probability, hence a reduction of the available volume [101].

The densification process induces also a strong quenching of positronium formation. As a matter of fact, the positron formation ratio in normal silica is $\nu_{Ps} \simeq= \frac{4}{3} I_3 = 73\%$ being the proportion between p-Ps and o-Ps $1:3$ [100]. The intensity I_3 drops from 55% to 13% (17% of positronium formation). This reduction can be due to concomitant factors: compacting of the material with reduction of free volumes available for Ps formation, enrichment of the free volumes by displaced oxygen, and free electrons at dangling bonds. Conversely the fraction I_2 increases from 19% up to 45%. The strong increase of I_2 is due to the oxygen enrichment of the trapping sites and annihilation of positrons at negative charged oxygen-related defects as evidenced by the decrease of the lifetime τ_2 of the trapped positrons [101].

To quantify this reduction in terms of a pore radius, it is necessary to introduce a model for the pick-off annihilation of o-Ps [102].

4.5 The Tao-Eldrup model

In order to understand the experimental PALS data we need a model which connect the o-Ps lifetime with the void size.

We consider the positronium atom as a single scalar particle with twice the electron mass, trapped into an infinite spherical potential well with radius R_0.

The radial part of the Schrödinger equation for the center-of-mass motion of Ps is written as [55]

$$\left\{ \frac{\hbar^2}{2m} \left[\frac{d^2}{dr^2} - \frac{l\,(l+1)}{r^2} \right] + V\,(r) - E_n \right\} \Psi_{Ps}\,(r) = 0, \tag{4.6}$$

where

$$V(r) = \begin{cases} 0 & 0 < r < R_0 \\ \infty & \text{elsewhere} \end{cases} . \tag{4.7}$$

The ground state wave function inside and outside the well is given by

$$\Psi_{Ps}(r) = \begin{cases} \frac{1}{2\pi R_0} \frac{\sin(\pi r/R_0)}{r} & 0 < r < R_0 \\ 0 & \text{elsewhere} \end{cases} . \tag{4.8}$$

The eigenvalues for Ps at the nth state are given by

$$E_n = \frac{n^2 \hbar^2 \pi^2}{2mR_0^2}. \tag{4.9}$$

The calculation of the annihilation rate requires the electron density ρ_e. Following the semiempirical approach after Tao [103] and Eldrup et al. [104], we assume the existence of a homogeneous electron layer with a thickness $\Delta R = R_0 - R$ inside the well. The probability for Ps in the ground state inside the electron layer is then given by

$$P = 4\pi \int_R^\infty |\Psi(r)|^2 r^2 dr = 1 - \frac{R}{R_0} + \frac{1}{2\pi} \sin\left(\frac{2\pi R}{R_0}\right). \tag{4.10}$$

Assuming the annihilation rate of o-Ps inside the electron layer is 2 ns, which is the spin averaged annihilation rate of p-Ps and o-Ps, which is also very close to the annihilation rate of Ps, the o-Ps annihilation rate as a function of free-volume radius, R, is then given by

$$\tau_{pick-off} = (2P)^{-1} = \frac{1}{2}\left[1 - \frac{R}{R+\Delta R} + \frac{1}{2\pi} \sin\left(2\pi \frac{R}{R+\Delta R}\right)\right]^{-1}. \tag{4.11}$$

The empirical parameter ΔR represents the overlap between the Ps wave function and those of the electrons in the layer. The parameter ΔR can be determined by fitting the observed τ_3 in materials with well characterized small pores [102]. The best-fitted value of ΔR for all known data is found to be 1.68 Å [102, 105].

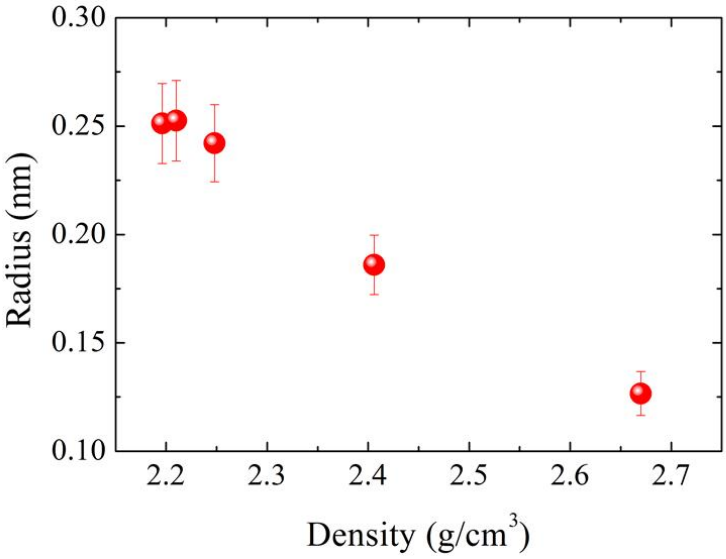

Figure 4.6: Pore radius as a function of the increasing density as obtained applying the Tao-Eldrup model using the o-Ps lifetime as described in the text.

It is worth noting that the Tao-Eldrup model assumes that the Ps is in its atomic ground state so it works only in small pores, $R \leq 2.5$ nm [105].

The mean voids radius R is reported in figure 4.6 as a function of the sample density. In the 6 GPa sample where the two decomposition described in 4.4 coexist, we consider an intensity weighted average of τ_3.

Figure 4.6 shows that the voids radius shrinks by about the 100% when the density is increased by about 22%. As a matter of facts the radius of the voids in normal silica is about 2.5 Å and it drops to 1.3 Å in the 8 GPa densified sample. The considered pore is the center of a 3D cage [17, 106]. The R values presented in 4.6 are in agreement with a void spaces molecular dynamics (MD) analysis in densified silica [107].

4.6 Medium range order in permanently densified v-SiO_2

At this point we can qualitatively discuss how the v-SiO_2 structure is affected by the densification procedure.

Diffraction data by Inamura and co-workers [72] shows that, in similar densification range, the SRO, *i.e.* the $Si(O_{1/2})_4$ thetrahedral structure is scarcely influenced by the densification. On the other hand, the FSDP is strongly affected by the density increase and it is shifted upwards by about 18%. The FSDP is an universal feature of glasses and liquids and it is considered as a fingerprint of the existence of the MRO. We can interpretate its density behavior as a proof of a modification in the MRO domain.

On the other hand, present data suggest that the open network of normal v-SiO_2 is filled causing the dramatical drop of the voids size highlighted in figure 4.6.

A densification mechanism which account for these experimental observation has been proposed by Sampath and co-workers for permanently densified v-GeO_2 [92]. In a simple 2D view normal silica is characterized by tetrahedra rings [106]. The applied hydrostatic pressure induces a distorsion of the tethrahedra packing. They will rearrange shrinking the volume of the inter tetrahedral rings [106]. Increasing further the densification, coordination number modification will appear, marking the transition from fourfold to sixfold coordinated structure [73].

4.7 The voids size and the FSDP

As already pointed out in the previous chapter the presence of the FSDP is thought as the fingerprint of the presence of MRO. It can be schematically

and roughly seen as the signature of a quasi-periodic arrangement of period $\mathcal{R} = 2\pi/Q_1$ which has a correlation length of $\mathcal{L} = 2\pi/\Delta Q_1$, where Q_1 is the peak position ad ΔQ_1 the peak width.

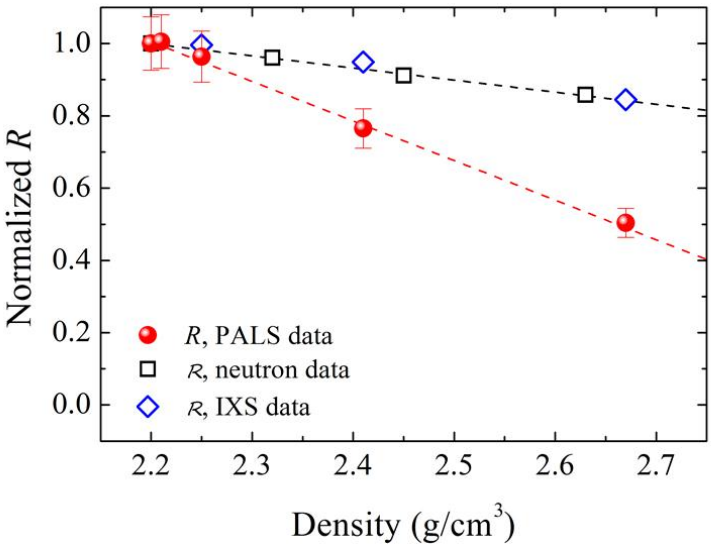

Figure 4.7: Pore radius R and FSDP associated length $\mathcal{R}$, both normalized to the normal silica value. Black squares are neutron diffraction data, from ref. [72] whereas blue diamonds indicate the FSDP position as obtained by an $S(Q, \omega = 0)$ scan during the IXS experiments.

Having two quantities which describes the medium range, a correlation attempt sounds natural. A first approach is to compare the voids radius R with the lengthscale $\mathcal{R}$. At this stage we are interested only in comparing their trends, so figure 4.7 reports the length $\mathcal{R}$ and the pore radius R normalized to their normal silica value. Despite both follow a linear trend the slope is completely different, $\mathcal{R}$ changes by about 18% whereas R by about 100%.

To improve our comprehension of the correlation between the FSDP and the measured void we consider the void-cluster model firstly proposed by Blétry [93] and subsequently utilized by Elliott [21, 18]. Within this framework the glass network is approximated as a mixture of spherical atoms and holes, having about

the same diameter and concentration. These spheres are arranged in a packing which maximizes the local chemical short-range order of atom and voids. In our case atoms are cation centered clusters, *i.e.* $\mathrm{A}\left(\mathrm{X}_{1/2}\right)_4$ tetrahedra. Atoms are separated by the average distance $d \equiv r_{A-A}$ and they are surrounded by spherical voids at an average distance D from the cations.

According to Blétry [93] such simplified system originates a peak in the concentration - concentration partial structure factor $S_{cc}(Q)$ in the Bhatia-Thornton formalism [108], and thus in the static structure factor. If atoms and voids have the same dimension $d = 3.08$ Å [17], the FSDP position is given by:

$$Q_1^{model} \simeq \frac{3\pi}{2d}. \tag{4.12}$$

Equations 4.12 can be generalized to the case of different atoms and holes sizes. Considering $\delta = D/d = 1 + \varepsilon$ the FSDP becomes shifted to the value

$$Q_1^{model} \simeq \frac{3\pi}{2d}\left(1 - \frac{\varepsilon}{2}\right) = \frac{3\pi}{2d}\left(\frac{3}{2} - \frac{D}{2d}\right). \tag{4.13}$$

The cation-void distance D of eq. 4.13 can be decomposed as

$$D = R + r_{\mathrm{Si}}, \tag{4.14}$$

where R is the void radius and $r_{\mathrm{Si}} = 0.4$ Å is the silicon crystalline radius [109].

Figure 4.8 shows the comparison between the FSDP position measured by neutron and X-ray and the calculated Q_1^{model} by means of the model. It can be seen that the proposed approach produce data which shows a qualitative agreement, with a small overestimation by about 2%. To obtain a better agreement we fix r_{Si} to obtain $Q_1^{model}(0\ \mathrm{GPa}) = Q_1(0\ \mathrm{GPa})$. The red open circles are obtained with $r_{\mathrm{Si}} = 0.6$ Å. This discrepance can be due to a screening effect of the oxygen atoms, whose radius is greater then the silicon one, $r_{\mathrm{O}} = 1.26$ Å [109].

Recent X-ray and neutron diffraction measurements in vitreous silica by Mei and co-workers have pointed out that the $S_{cc}(Q)$ does not present any

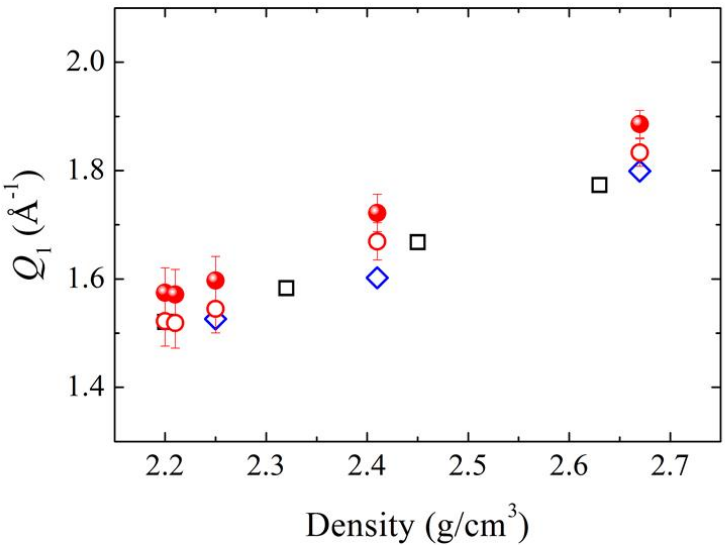

Figure 4.8: Comparison between the measured FSDP position Q_1 and Q_1^{model} calculated as described in the text using the ionic radius r_{Si} (red bullets) and the optimized value (red open circles). Black squares are neutron diffraction data, from ref. [72]; blue diamonds indicate the FSDP position as obtained by an $S(Q, \omega = 0)$ scan during the IXS experiments.

peak compatible with the FSDP, thus criticizing the Blétry-Elliott model [20]. Alternative models such as the approach proposed by Wright [17] presents strong analogies in the microscopical picture originating the first sharp diffraction peak. As a matter of fact, Blétry's void centered atoms cluster is replaced by a periodic repetition of void centered cages [92, 20]. In both cases we are considering a void centered cluster of $\mathrm{Si}\left(\mathrm{O}_{1/2}\right)_4$ tetrahedra. This strong analogy and the good result obtained using the Blétry approach could suggest that, even it is not rigorously correct, the model is accounting for an underlying more general property.

4.8 Density evolution of structural and dynamical quantity

In this section we will try to summarize the observation about the evolution of structural and dynamical quantities as a function of the density in permanently densified vitreous silica.

The first results obtained in chapter 3 is that ω_{BP} doubles its position when the density is increased by the 22%. Conversely the Debye frequency ω_D which describes the elastic medium evolution shows a weaker density dependence.

In this chapter we have dealt with the structural evolution of the densified material. The first sharp diffraction peak shows a variation of its position Q_1 of about $\sim$18% whereas the width is almost unchanged. In the common and quite accepted view of the FSDP, this means that the MRO extent in the glass is not substancialy modified whereas the densification acts on its periodicity. The investigation of the dimension of the interstitial voids in vitreous silica shows an abrupt shrinkage of the voids volume as a function of the density ρ. As a matter of fact the voids radius is reduced by 50%. The inter tetrahedral voids are one of the main features characterizing the medium range in glasses [106, 20].

The use of a model based on the chemical ordering of thetrahedral clusters and voids [93, 21, 18] allows to link the evolution of the void spaces with the FSDP reproducing quantitatively both its position and evolution.

In figure 4.9 we report a comparison between the normalized BP position and the FSDP position which shows a weaker trend. Conversely the inverse of the void-silicon distance D shows a remarkable good agreement with the observed boson peak position.

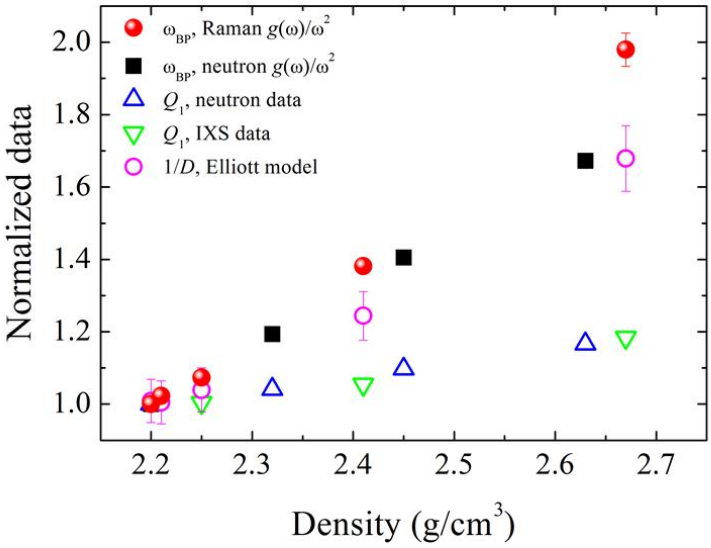

Figure 4.9: Density evolution of the BP and of the Q_1 and $1/D$; symbols are as in the legend. Each dataset is normalized to its normal silica value.

A proposed model for the origin of the boson peak links its appearance to the lowest energy van Hove singularity in the vibrational density of states $g(\omega)$ [37, 69, 66]. Within this framework the boson peak is originated by transverse acoustic modes which pill-up near the the border of the Brillouin zone [37, 69]. As a matter of fact, even if the absence of translational periodicity prevents the construction of a reciprocal lattice, the peaks in the static structure factor act as reciprocal vectors giving origin to a pseudo-periodic structure already observed in many materials [110, 111]. The border of the first pseudo Brillouin

zone (p-BZ) is thus $Q_1/2$.

Following this line of argument, the BP will mark the maximum of the transverse acoustic branch. However the flattening of the trasverse branch can anticipate the appearance of this maximum at Q_0. The flattening of the transverse branch has been observed by means of IXS [112, 113] and MD simulations [70, 69]. We can thus define an effective p-BZ border corresponding to the maximum of the branch, *i.e.* the BP position [66, 61]. Assuming a sinusoidal dispersion of the transverse branch up to the maximum, the position of the BP reads

$$\tilde{\omega}_{BP} \propto \frac{\pi}{2}\frac{v_T}{Q_0}. \tag{4.15}$$

We assume that $Q_0 \propto 1/D$, where D is the void silicon distance detailed in eq. 4.14 with $r_{Si} = 0.6$ Å. This result is reported in figure 4.10.

It is worth to note that the $\tilde{\omega}_{BP}$ refers to $g(\omega)$ whereas ω_{BP} is determined as the maximum in $g(\omega)/\omega^2$. Assuming a log-normal shape for the BP in the reduced VDOS [76] we can transforme $\tilde{\omega}_B P$ to ω_{BP} as

$$\tilde{\omega}_{BP} \overset{e^{-2\sigma^2}}{\longrightarrow} \omega_{BP}, \tag{4.16}$$

where σ is the variance of the log-normal.

Experimental fitted values of $\sigma(\rho)$ are very close, hence the transformation in eq. 4.16 does not strongly perturb the trend.

The BP trends reported in figure 4.10 are in good agreement. To obtain data on absolute units, it is needed a determination of the proportionality between $1/D$ and Q_0. A possible way exploits the similarity between 8 GPa densified glass and α-quartz polycrystal which will be presented in the chapter 5. In any case, even if from a qualitative point of view, this finding suggests that the evolution of the BP can be explained by considering the evolution of the dispersion curve of the transverse acoustic branch. The BP is related to the

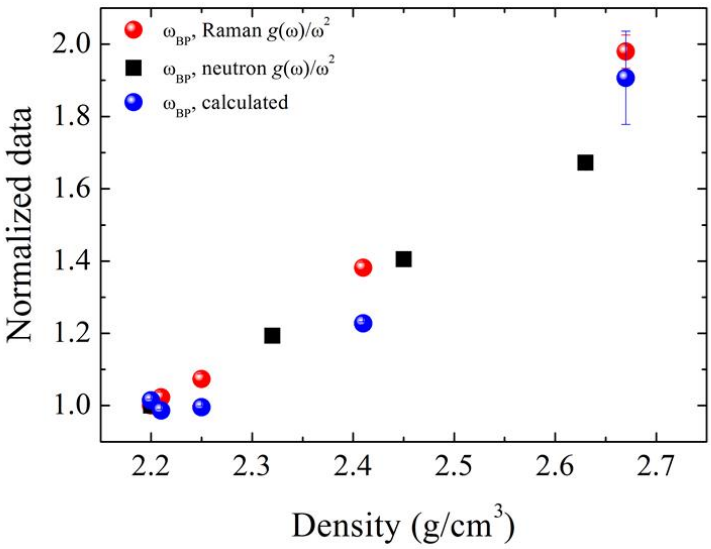

Figure 4.10: Density evolution of the measured boson peak position with that calculated using eq. 4.15 and 4.16; symbols are as in the legend. Each dataset is normalized to its normal silica value.

evolution of an effective Brillouin zone border as well as to the modifications of the elastic constants trough the sound velocity.

Chapter 5

Elastic continuum and microscopic dynamics in glasses

Si l'ordre est le plaisir de la raison,
le désordre est le délice de l'imagination.
P. Claudel

In a recent paper by Chumakov and co-workers have shown the gradual transformation with pressure of the boson peak of the sodium silicate glass $Na_2FeSi_3O_{0.85}$ in the transverse acoustic van Hove singularity of aegirine, *i.e.* the corresponding crystal [66]. This finding is mainly obtained by means of nuclear inelastic scattering (NIS) and *ab-initio* calculations. Glass and crystal show an equal excess of states above the Debye level. This observation suggests that the VDOS of a glass is similar to that of a crystal, consisting only of acoustic modes without any additional modes. These acoustic modes are modified by the disorder but their energy spectrum does not differ qualitatively from that of the crystal (apart from an additional broadening). The boson peak originates from the piling up of these acoustic states near the boundary of the pseudo-Brillouin zone.

As a matter of fact, even if the reciprocal lattice cannot be rigorously defined, the existence of a pseudo Brillouin zone (p-BZ) has been already observed in glasses [110, 111]. In particular the peaks in the static structure factor act as ill defined reciprocal vectors. The size of the first p-BZ is thus Q_1, the position of the FSDP, being $Q_1/2$ the position of its border. On the other hand, dynamical data show that the transverse branch can reach its maximum before the p-BZ border thus defining an effective zone border Q_0 [66, 61].

Triggered by such considerations, we have carried out a direct investigation of the modes in both polycrystalline α-quartz and in the permanently densified glass with the corresponding density. This comparison is possible exploiting the 8 GPa permanently densified silica sample. NIS spectroscopy is a good tool to determine the vibrational density of states $g(\omega)$, if a Mössbauer atom is present [114]. On the other hand it does not allow the direct investigation of the modes which are probed by IXS.

In this chapter we will show some preliminary results of this comparison between the response of the glass and that of the polycrystal. The vibrational dynamics is marked by a characteristic wavelength ξ, which separates the macroscopic elastic response from the microscopic dynamics, where polycrystalline and glassy spectra are almost indistinguishable. At higher Q, where spectra are proportional to $g(\omega)/\omega^2$ the crystal spectrum shows a peak at 9 meV which is very close to the boson peak of the glass.

5.1 Inelastic X-ray scattering experiments

Silicon dioxide SiO_2 presents nineteen different crystalline phases; among these α-quartz is the stable one at room temperature and pressure. The density of the α-quartz is 2.65 g/cm^3 which is really close to $\rho_8 = 2.67 \pm 0.01$ g/cm^3 measured for the 8 GPa sample, see table 3.1.

Inelastic X-ray scattering experiments on both polycrystalline α-quartz and 8 GPa permanently densified glass were performed at the high resolution beamlines ID16 and ID28 at the European Synchrotron Radiation Facility (ESRF) in Grenoble (France).

The layout of ID28 has been already presented in section 3.5.1. In general ID16 is quite similar: actually ID28 is based on ID16 layout. The main differences are the absence of the post-monochromator, and the dimension of the experimental hutch of the beamlines: ID16 analyzers arm is limited only to $0° \leq \vartheta \leq 13°$ whereas ID28 arm can span between 0° and 50°.

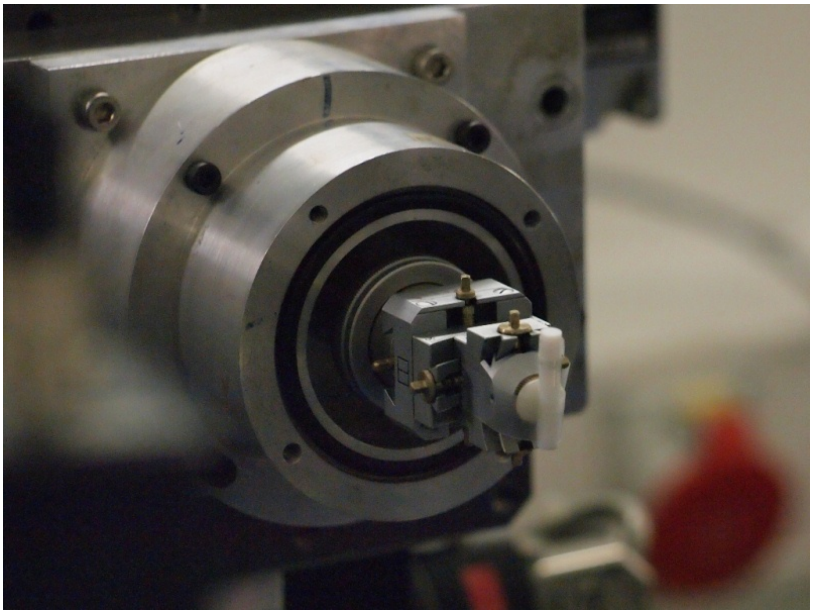

Figure 5.1: Polycrystalline sample in the mylar sample holder.

Measurements were performed using the (12 12 12) reflection of the silicon monochromator. This allows an experimental resolution of about $\Delta E \simeq 1.3$ meV (FWHM), which has been measured on a plexiglass slab. Low Q measurement on the polycrystal were performed on ID16 whereas high Q measurements and the whole investigation on the 8 GPa sample were carried out at ID28. Moreover in order to compare the datasets acquired on different instruments, we measured

also a reference low Q polycrystal spectra at ID28.

The polycrystalline powder has been obtained by crushing a single crystal in a mortar. The size of the so obtained grains is bigger than commercial powders, thus preventing small angle scattering effects. The quartz powder was contained in a mylar cylindrical tube (wall thickness $\sim$5 μm) and fixed between two caps. A lead strip above the sample position has been placed to ease the alignment procedure. Figure 5.1 shows the mylar sample holder loaded with the sample.

Low Q measurements on the SiO_2 glass have been performed at $T = 573$ K. Conversely, the investigation on the polycrystal and the high Q measurements on the glass have been carried out at room temperature.

5.1.1 IXS spectra: polycrystal *versus* glass

Low Q spectra obtained for the two samples are reported in figure 5.2 at almost the same Q value. The polycrystal, fig. 5.2(a), has been measured quite far from a Bragg peaks. This results in a reduct elastic line. The inelastic features are clearely visible. In the glass, fig. 5.2 (b), the inelastic part of the spectra appears masked by the more relevant elastic contribution.

Figure 5.3 shows the Q evolution of the inelastic part of the spectrum of both glass and polycrystal. The inelastic part is calculated by subtracting the elastic line as obtained by fitting the spectrum with a δ function convoluted with the experimental resolution (actually the model function includes also the inelastic part as reported in eq. 5.1. In order to safely compare datasets coming from different experiments and instruments, experimental data have been corrected for the detectors efficiency as well as for the measured transmission, and for the Bose-Einstein population factor.

The Q evolution is reported in figure 5.3, from 1.3 nm^{-1}, inset (a), up to 72 nm^{-1} inset (f).

In the low exchanged wavevector region, $Q \lesssim 2$ nm^{-1} the polycrystal spectra

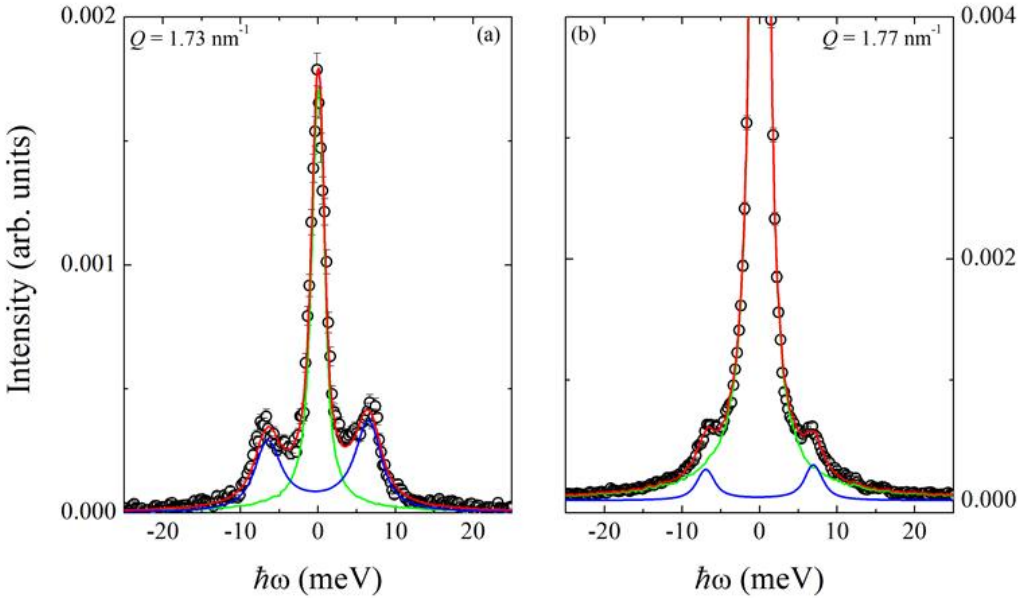

Figure 5.2: Comparison between IXS spectra of the polycrystalline α-quartz (a) and the 8 GPa permanently densified silica sample (b). The Q values are reported in the plot. Black circles are the experimental data, red line is the best fit using the model of eq. 5.1. The green line is the experimental resolution and the blue line the inelastic component. The intensities are normalized to a 100 mA current in the storage ring and are reported as counts per 60 s.

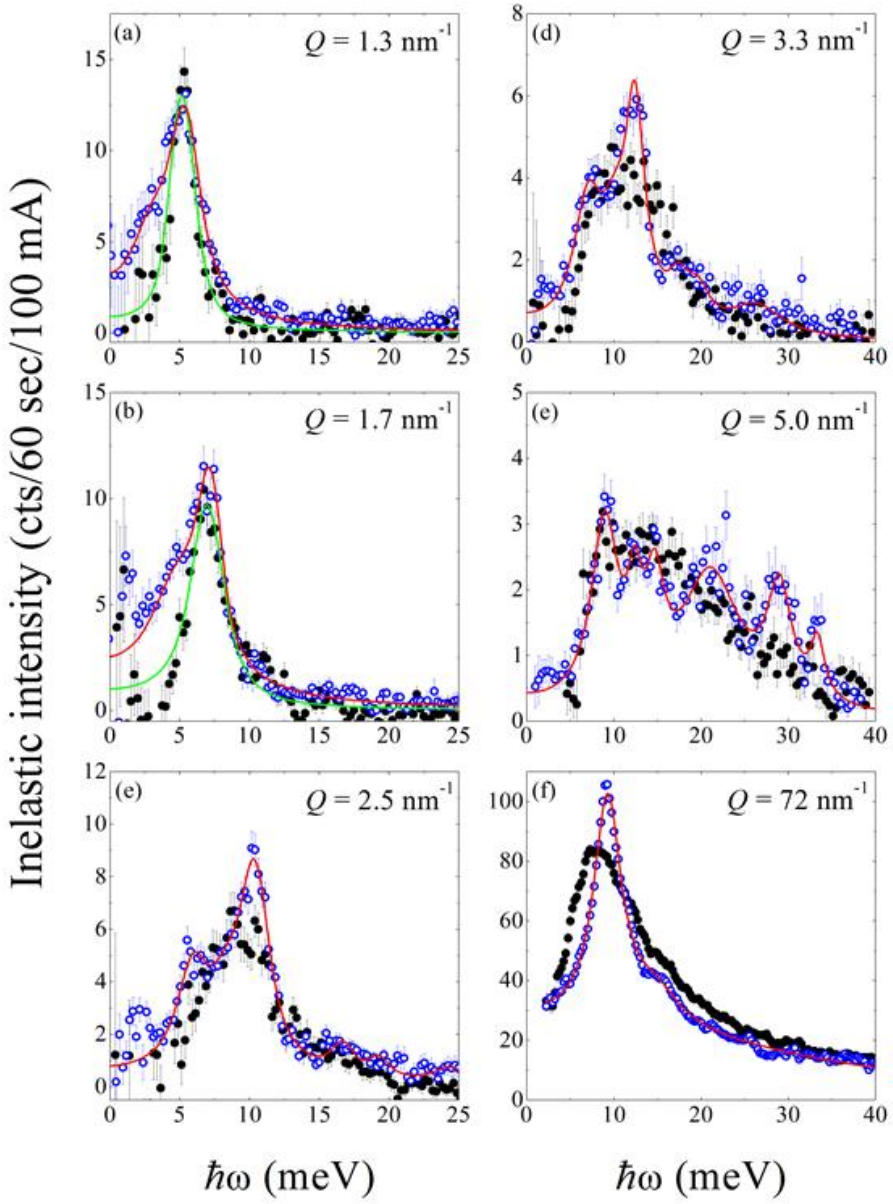

Figure 5.3: Comparison between IXS spectra of the polycrystalline α-quartz (blue open circles) and of the 8 GPa permanently densified silica sample (black dots). The Q values are reported in the insets. The red line results from a fit of the polycrystal data with one DHO (insets (a) and (b)) and with six lorentzian functions. The green lines are the fit with one DHO in the glass. The intensities are normalized to a 100 mA current in the storage ring and are reported as counts per 60 s.

are broader than the glass ones. As a matter of fact, in the large wavelength limit elastic waves in an isotropic solid have defined polarization, either longitudinal or transverse. In this case the dynamic structure factor $S(Q,\omega)$ shows only one peak which is associated with the longitudinal wave. Conversely, in crystals this holds only along few symmetry directions. The dynamic structure factor of a polycrystal can be approximated as the orientational average on the single crystal one, so a small transverse (or quasi transverse) component is expected [115]. Actually, polycrystal spectra in figure 5.3 show a relevant transverse component in the whole explored range. Figure 5.3(c) shows two transverse peaks.

In general, the glassy spectrum is smoother than the polycrystalline one. At high Q the glass spectrum also shows a transverse excitation. Furthermore, in this region optic excitations grow, being comparable to acoustic ones.

Increasing Q, polycrystal and glass spectra looks similar and above a certain value almost identical. The last inset, 5.3(f) refers to $Q = 72$ nm^{-1} where $S(Q,\omega) \propto g(\omega)/\omega^2$ [115]. The polycrystal shows a peak which is very close to the BP of the glass, even if the BP is broader.

It is worth to note that the precise nature of the glass vibrational modes cannot be extracted from this comparison. Due to the orientational average, we can only conclude that a glass mode at a given energy is a linear combination only of a limited subset of all the crystal eigenstates, with unknown coefficients.

5.2 The determination of Q_c

In order to determine the wavevector which marks the transition between the two regimes we have fitted the spectra using a simple single excitation model function, namely:

$$S(Q,\omega) = A_{el}(Q)\,\delta(\omega) + A_{inel}(Q)\,\frac{1}{\pi}\frac{\Omega(Q)^2\,\Gamma(Q)}{\left(\omega^2 - \Omega(Q)^2\right)^2 + \omega^2\Gamma(Q)^2}. \qquad (5.1)$$

where A_{el} describes the intensity of the elastic component whereas A_{inel}, Ω, and Γ refer to the inelastic propagating excitations and they respectively represent the intensity, position and attenuation. This analysis allows us to estimate the FWHM Γ of the inelastic part of the spectra.

As usual, the experimental intensity can be written as:

$$I(Q,\hbar\omega) = I_0(Q)\, R(\hbar\omega) \otimes \left\{ S(Q,\hbar\omega)\, \frac{\hbar\omega}{K_B T} \left[n(\hbar\omega, T) + 1 \right] \right\} + bkg, \quad (5.2)$$

$n(\hbar\omega)$ is the Bose factor, the term $[n(\omega)+1]\,\hbar\omega/K_B T$ account for the quantum nature of the interaction and fulfill the detailed balance principle. The baseline term is added in order to take into account the electronic background of the detector and the environmental background. Moreover, the overall intensity factor $I_0(Q)$ is a normalization factor which is influenced by the atomic form factors, the efficiency of the analyzers, and by all other angle-dependent instrumental correction factors. An example of the fit obtained using this model is reported in figure 5.2.

Neglecting a detailed description of the evolution of the spectral features, the main point highlighted by fig. 5.3 is that the two systems are very similar for Q greater than $Q_c \sim 2.5$ nm^{-1}. This value can be better defined by comparing the Γ of the polycrystal and that of the glass, as reported in figure 5.4.

For $Q > Q_c \simeq 2$ nm^{-1} both glass and polycrystal follow a $\sim Q^2$ law [25, 29, 86, 116]. For $Q < Q_c$ the broadening of the crystal spectrum has a linear Q dependence, as expected in the case of a linear dispersion curve. On the other hand the glass shows a lower Γ which follows a $\sim Q^4$, Rayleigh scattering law. This $Q^4 - Q^2$ regime has been already observed for normal silica [116, 117] and more fragile system like glycerol [86]. This finding highlights a situation more complex than the simple $\sim Q^2$ law observed in previous experiments [25, 29], deserving further studies.

The value $Q_c \simeq 2$ nm^{-1} can be associated to a length $\xi = 2\pi/Q_c \sim 30$ Å,

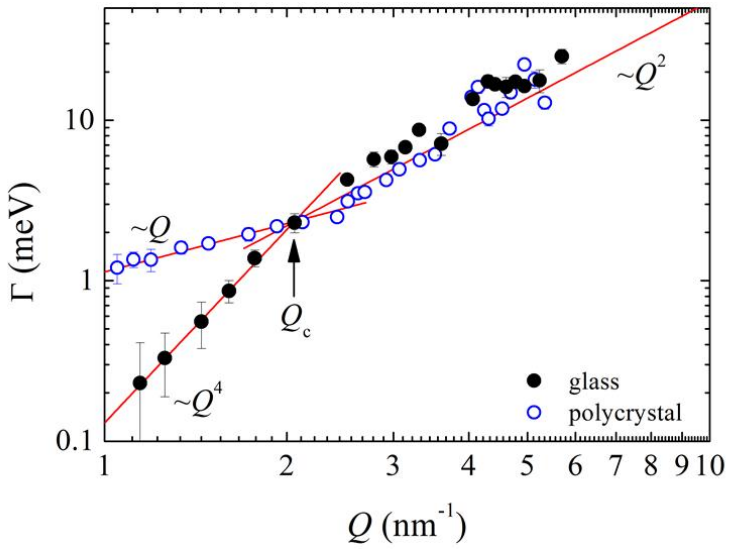

Figure 5.4: Comparison between Γ of the polycrystalline α-quartz (blue open circles) and 8 GPa permanently densified silica sample (black dots). The red lines highlight the behavior $\Gamma(Q)$ behavior marking the appearance of the crossover Q_c.

about 20 interatomic distances which marks the crossover between the two regimes. The static length ξ is in agreement with the size of the typical elastic heterogeneities observed in MD simulations of silica [118, 119]. These numerical works investigate the correlation length of large vortices related to the response of transversal motions of particles when they respond to an external deformation. These *non affine* displacement marks the transition between a region where the classical elastic theory holds to a region it is subject to strong limitations [119]. Present data suggest that the origin of the departure from classical behavior is related to the local anisotropy given by the ordered crystal like structure.

Chapter 6

A glass exhibiting a crystal-like behavior: the case of $SiSe_2$

Bene olet qui nihil olet.
Latin proverb

In the previous chapters we have already highlighted some of the most problematic points concerning the vibrational properties of glasses. In this chapter we will try to shed some new light on the nature of the high frequency collective dynamics, investigating the silicon diselenide.

Silicon-selenium glasses are strong covalently bounded glasses belonging to the chalcogenide family, which have a broad technological interest. Their semiconducting properties were revealed by Kolomiets [120] allowing a wide spectrum of technological applications, ranging from the optical fibers to the new phase-change memories (PRAM), which are expected to take over from the actual flash memory technology [121].

Also from a scientific point of view, chalcogenide systems such as $GeSe_2$ and $SiSe_2$ are of primary concern. As a matter of fact they are strong glasses exhibiting structures based on both corner and edge sharing tetrahedra. Conversely,

the prototypical strong glasses v-SiO_2 and v-GeO_2 are characterized by a corner sharing structure.

Vitreous $GeSe_2$ has been recently investigated by Orsingher and co-workers displaying the existence of a propagating mode and an optic-like excitation located at about the BP energy [122]. In this chapter we focus on the less studied vitreous $SiSe_2$ which displays very interesting features.

Silicon-selenium glasses Si_xSe_{1-x} can be prepared by melt quenching techniques over a wide interval of composition, ranging from $x = 0$, *i.e.* the pure selenium glass, to $x = 0.5$ [123]. The only note crystalline phase is the $SiSe_2$ whose structure at ambient pressure contains only edge-shared $Si\left(Se_{1/2}\right)_4$ tetrahedra. This arrangement leads to a connected molecular network with macroscopic extension only in one dimension. These chains are held together by van der Waals bonding at a distance of about 6-7 Å[124, 125] or via corner shearing tetrahedra [126, 127]. This arrangement is also retained by the $SiSe_2$ glass, which is reported of a high degree of medium range order [127]. Moreover, BLS measurements as a function of the composition show a minimum for $x = 0.333$ with a low sound velocity.

Inelastic neutron scattering measurements were performed at three instruments: BRISP and IN3 at the High Flux Reactor of the Institue Laue-Langevin in Grenoble; TOFTOF at the reactor *Heinz Maier-Leibnitz* FRMII in München. The combined use of these three datasets, spanning different portions of the (Q, E) plane, allows to produce a detailed picture of the vibrational dynamics in the THz. The aim of this study is to investigate the character of the excitations up to the first pseudo Brillouin zone and beyond. The ultimate challenge is to shed some new light on the low frequency mode (or modes) which originates the boson peak.

6.1 Sample preparation: vitreous Si_xSe_{1-x}

The preparation and the handling of silicon-selenium glasses require great attention to details and safety rules. As a matter of fact $SiSe_2$ is quite reactive and it hydrolyzes very quickly upon exposure to room environment. In air, it produces a very bad smell which warns that toxic selenium compounds are forming. Moreover, conventional melting largely results in a crystallization of the sample. For these region, following ref. [128], we used a non stoichiometric composition, Si_xSe_{1-x} with $x = 0.365$, implementing several tricks able to assure a successful standard production procedure.

The glass was prepared starting from silicon powder (Aldrich, purity greater than 99.999%, mesh-60) and selenium powder (Aldrich, purity greater than 99.995%, mesh-100).

To avoid air contamination the whole glass preparation procedure was carried out in sealed quartz ampules. Each ampule was obtained starting from a self-made quartz test-tube of 10 mm (external diameter) and about 20 cm long. Each test-tube was firstly outgassed in vacuum using a welding torch and the vacuum apparatus schematically depicted in figure 6.1.

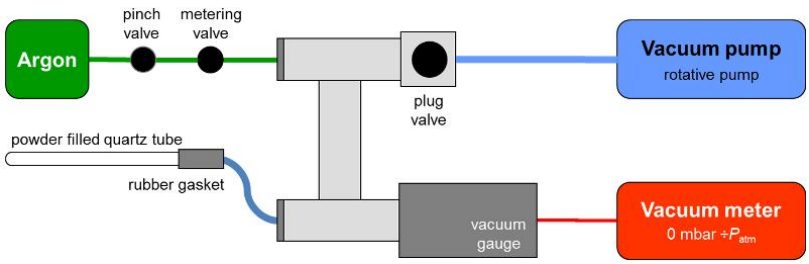

Figure 6.1: Schematic representation of the vacuum apparatus used in the production of the sample.

A small amount (5 g) of silicon and selenium powders, mixed in the selected composition, was put in the test-tube. After the filling, the test-tube was con-

nected to the vacuum apparatus in figure 6.1, evacuated to a pressure of $P = 10^0$ mbar and then refilled with argon. This *washing* procedure was repeated three times. After that, the tube was filled with argon ($P = 2 \div 4$ mbar) and sealed with the welding torch.

The powder was homogenized at 1100°C in a furnace for at least 96 hours. The ampules were heated in horizontal, carefully checking for an uniform distribution of the powder on the whole ampules length. Before the quenching the temperature was lowered to 1000°C for an hour. The ampules were quenched in room temperature water, paying attention in keeping the horizontal position of the tube.

A successful quenching produces an yellowish glass, figure 6.2(a). This colour characterizes the composition range $0.333 \div 0.365$ [123]. Sample were characterized by Raman scattering to verify the glassy nature, see section 6.2. However, the differences between the glass and the crystalline material can be appreciated also by a visual inspection, as shown in figure 6.2(b) and (c).

This preparation protocol allows the preparation of about 60 g of glassy sample.

In the following we will refer to the sample as $SiSe_2$ using the appropriate x-dependent data for every comparison.

6.2 Characterization of the v-$SiSe_2$

Figure 6.3 shows a Raman spectrum of one of the $SiSe_2$ samples produced as described in section 6.1. Raman measurements were performed with the same apparatus described in section 3.2, keeping the bulk sample inside its quartz ampule. A zoom of the BP region is reported in the inset. The peak position results $\omega_{BP}^{Raman} = 12.5 \pm 0.2$ cm^{-1}.

The Raman scattering spectra has been compared to the crystalline one by

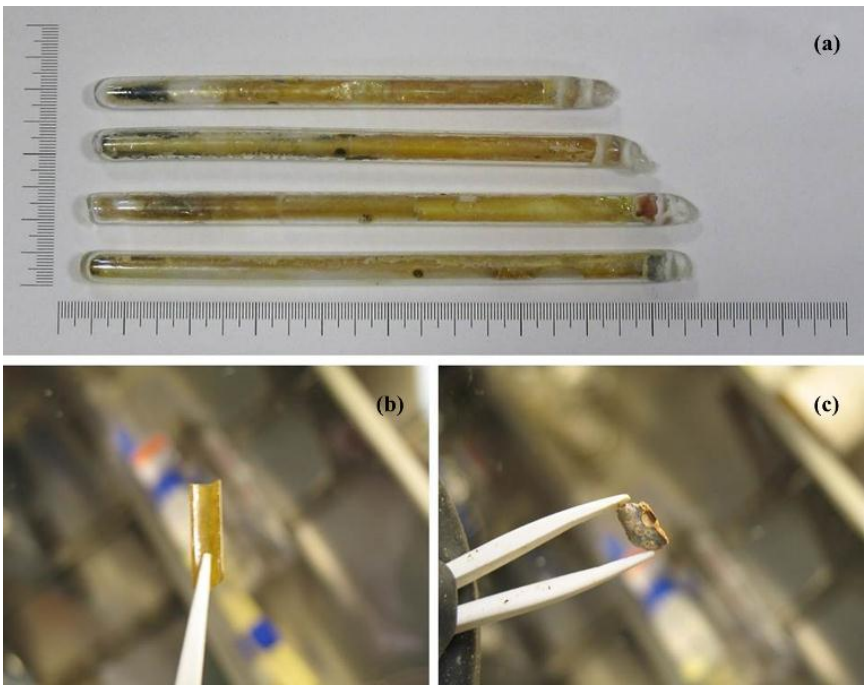

Figure 6.2: (a) Quartz ampules containing glassy silicon diselenide. Visual inspection of a glassy (b) and crystalline sample (c). This operation was performed inside a glove-box.

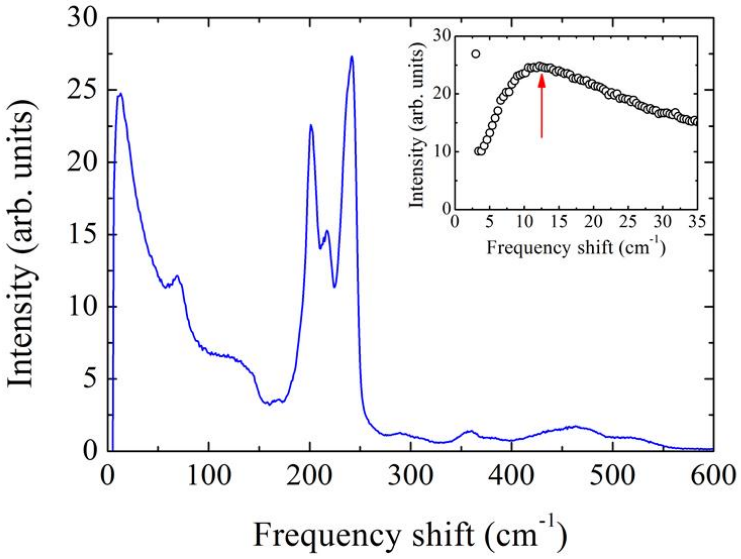

Figure 6.3: Raman scattering spectra of v-$SiSe_2$; the BP region is reported in the inset. The arrow marks the $\omega_{BP}^{Raman} = 12.5 \pm 0.5$ cm^{-1}. Spectra were measured in VV polarization.

Tenhover and co-workers in refs. [124, 125]. Spectra are very similar and the molecular modes are at about the same frequency. In particular the 216 cm^{-1} mode represents the symmetric vibration of the four outer chalcogens of the bitetrahedral unit and it retains the same relative intensity in crystals as well as in glasses. This is considered as an indication of the presence of medium range order in the form of edge sharing chains [124, 125].

A complete structural analysis of the system Si_xSe_{1-x} as a function of x has been done by Johnson and co-workers [129]. Neutron diffraction and EXAFS data indicate a significative chemical ordering in the glass supporting the idea of the edge sharing chains. As a matter of fact when the concentration is increased, the diffraction pattern shows a pre-peak which evolves as a function of x and a sharpening of the subsequent peak, see fig. 6.4. In the following we will refer to these peak as pre-peak Q_{pp} for the first peak and first sharp diffraction peak Q_1 for the second one. These names are after Johnson but are used only to

identify the peaks whose physical meaning will be discussed in the following. The composition $x = 0.37$ is the closest to our choice; for $x = 0.37$ we have $Q_pp = 0.96 \pm 0.02$ Å^{-1} and $Q_1 = 2.05 \pm 0.02$ Å^{-1}.

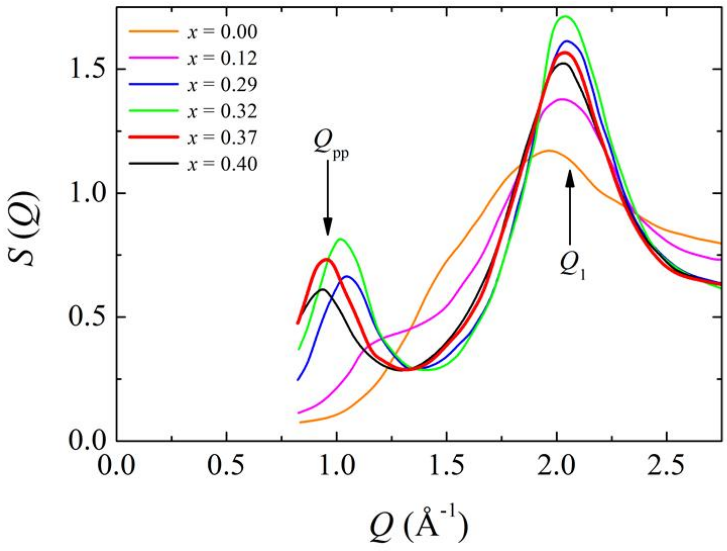

Figure 6.4: neutron diffraction spectra for vitreous Si_xSe_{1-x} as a function of x; colors as in the legend. The thick red line indicates the composition $x = 0.37$, the closest to our choice. Data are limited to the low Q region and are from ref. [129].

The sound velocity has also been measured as a function of the composition by Bhadra and co-workers [130]. Unfortunately their BLS work is strongly belittled by the absence of a clear determination of the refractive index. Their determination of $n = 2.5 \pm 0.5$ allows only a rough estimation of a velocity interval for the sound velocity. For $x = 0.365$ we expect $v_L^{max} \sim 2170$ m/s and $v_L^{min} \sim 1470$ m/s. These values will be used in the following as limit values.

6.3 Neutron scattering measurements

Silicon and Selenium are mainly coherent scatterers. Their scattering cross sections are reported in table 6.1. The incoherent cross section amount to about

$\sim 0.2\%$ (Si) and $\sim 4\%$ (Se) of the total. Since our sample is a coherent scatterer, it allows the study of the collective mode safely neglecting the incoherent contributions.

elements	σ_{coh} (barns)	σ_{inc} (barns)	σ_{abs} (barns)
Si	2.1699(10)	0.004(8)	0.231(3)
Se	7.98(2)	0.32(6)	11.7(2)

Table 6.1: Neutron coherent scattering cross section σ_{coh}, incoherent scattering cross section σ_{inc}, and absorption cross section σ_{abs} for Si and Se [131].

Neutron scattering experiments were performed using specially designed vacuum tight cells. To load the cells, the bulk glass was crushed in a mortar to obtain a fine powder. This operation was performed, both at ILL and FRMII, in a argon filled glove box. The density of the powder was estimated by weighting the sample and evaluating the filled volume inside the experimental cell. This leads to $\rho_p \sim 2.2$ g/cm^3 about 2/3 of the bulk density $\rho_b = 3.22 \pm 0.05$ g/cm^3 [123].

In the following we report a brief description of the used instruments as well as of the instrumental setups.

6.3.1 BRISP

BRISP (BRIllouin Spectrometer) is a time of flight (TOF) instrument, specifically built to perform small-angle spectroscopy with thermal neutrons [132, 133].

BRISP is placed at the exit of the 35° inclined thermal beam tube IH3, in the ILL reactor hall, and is located on a 4 m high seismic-proof steel platform. Its design is based on a hybrid configuration, conjugating a focusing crystal monochromator, to define the energy of the incident neutrons and a rapidly

rotating Fermi chopper, which enables a high-resolution TOF analysis of the scattered neutrons. The instrument scheme is reported in ref. [132].

The desired wavelength is extracted from the in-pile white beam via Bragg reflection at a multi-crystal focusing monochromator. The beam is chopped into broad neutron pulses by a first chopper. This device, named backround chopper, is designed to lower the incident beam background and, properly phased with the Fermi chopper, it minimizes the high orders contamination of the beam. The monochromatic neutron pulses are then collimated by an honeycomb converging collimator. This collimator provides both high transmission and convergence collimation in both the vertical and the horizontal scattering. However, if a high neutron flux on the sample is needed, the honeycomb can be opened and replaced with B_4C diaphragms. The collimated beam passes through a rapidly rotating Fermi chopper which provides the time reference for the TOF analysis. The neutron pulses are scattered by the sample and finally collected by a large-area two-dimensional detector. The detector is composed ^3He tubes, which can determine the position of the impinging neutrons within a precision of 1.3 cm in the horizontal direction and 1.1 cm in the vertical one. The detector array is mounted on a translation stage that allows variations of the sample-to detector distance in a 1.5-6 m range, to adapt accessible angular range, angular resolution and scattered intensity to the desired values The entire beam-line is set under vacuum and carefully shielded in order to obtain a low background noise.

In the present experiment we used an incident wavelength of 1 Å (reflection (0 0 4) of the PG monochromator) setting the detector at a distance of 4 m. The measurements were done at room temperature, keeping the sample under high vacuum. To increase the incident flux the honeycomb collimator was opened using some B_4C diaphragms to achieve a Q resolution better than $\Delta Q < 0.05$ Å^{-1}. The energy resolution was measured on a vanadium slab, obtaining $\Delta E = 3.2$ meV.

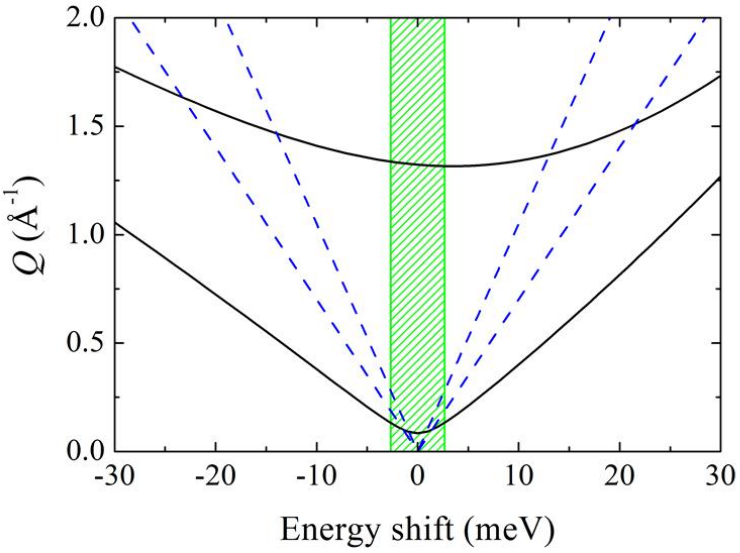

Figure 6.5: Kinematical range of BRISP in the configuration described in the text. The region filled with green slanted lines represents the experimental resolution. The blue lines are the extrapolation of the BLS longitudinal maximum and minimum sound velocities, [130].

The sample was loaded in a flat aluminum tight cell with a sample pit of $50 \times 30 \times 10$ mm^3 and wall thickness of 0.9 mm. The vacuum tight was ensured by a viton o-ring. A B_4C mask was designed to screen the o-ring and thickest part of the cell, thus selecting the scattering volume on the sample.

6.3.2 TOFTOF

TOFTOF is a direct geometry multi-chopper time-of-flight spectrometer, located at the research neutron source *Heinz Maier-Leibnitz* FRMII in München [134]. The instrument scheme is reported in ref. [134].

Neutrons, moderated by the cold source (D_2 at 25 K), are guided through an S-shaped curved neutron guide to the primary spectrometer. The guide also acts as a velocity filter for the neutrons with a cutting edge of 1.38 Å. In the primary spectrometer seven high speed neutron chopper discs are used to select

short monochromatic neutron pulses from the continuous neutron beam. The neutron pulses impinge on the sample and are scattered on the detectors which are arranged tangentially to the intersection lines of the Debye-Scherrer cones with the surface of a virtual sphere with a radius of 4m around the center of the sample. The remote position of the spectrometer, in combination with the S-shaped curved primary neutron guide, and an elaborate shielding concept results in an excellent signal-to-background ratio.

The incident neutron wavelength can be selected from a broad continuous neutron spectrum ranging from 1.4 to 12 Å. In the present experiment we chose $\lambda = 5$ Å, obtained with a chopper frequency of 12000 rpm , leading to a gaussian shaped resolution of $\Delta E \simeq 160$ μeV (FWHM), measured on a vanadium rod at $T = 13$ K.

The sample was loaded in a 50 mm high hollow cylinder container with internal and external diameter of 18 mm ad 25 mm, respectively, and wall thickness of 0.1 mm.

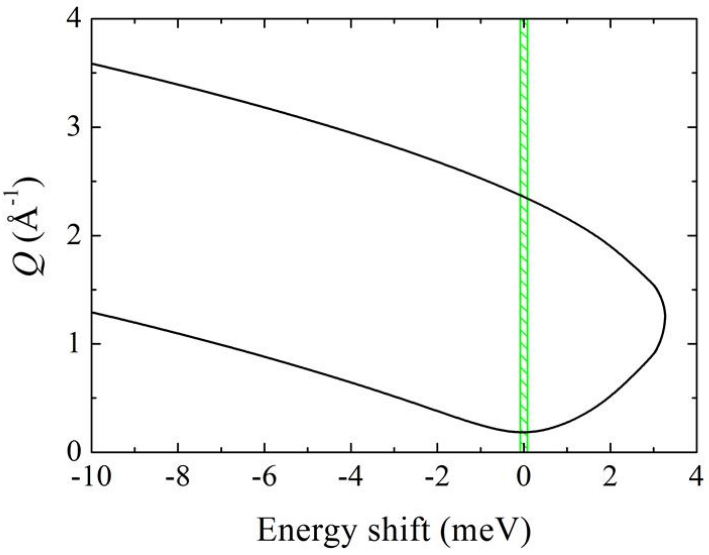

Figure 6.6: Kinematical range of TOFTOF in the configuration described in the text. The region filled with green slanted lines represents the experimental resolution.

6.3.3 IN3

IN3 is a classical three-axis spectrometer (TAS) located in the experimental hall of the High-Flux Reactor of the Institut Laue-Langevin in Grenoble. The schematic instrumental layout is reported in figure [133].

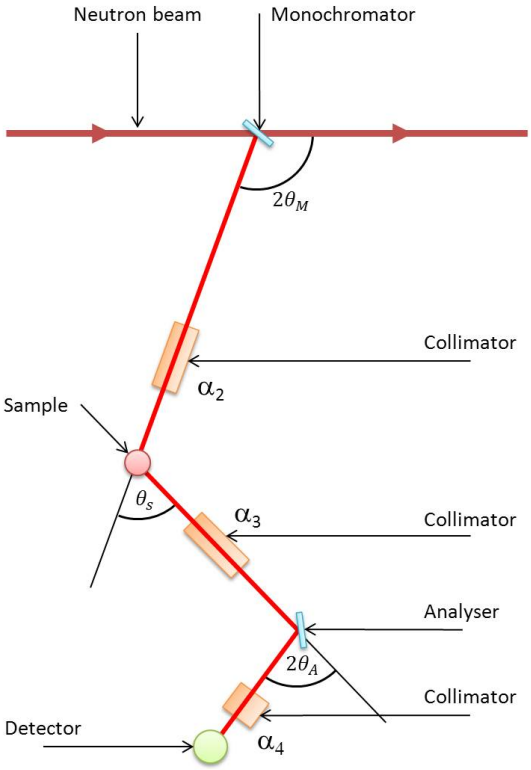

Figure 6.7: Schematic representation of the axes and angles involved in the triple axis operations.

IN3 operates on a through-going thermal neutron guide. The name TAS refers to the axes of the three components of the instrument: the monochromator, the sample and the analyzer, schematically reported in figure 6.7. IN3 is equipped with a double-faced monochromator with PG(0 0 2) and Cu(1 1 1) having variable curvature allows vertical focusing. The monochromator defines the incident wavevector $\mathbf{k}_i$ which can be varied by modifying the Bragg angle ϑ_M. The IN3 analyzer is an horizontally focusing PG(0 0 4) and it receives the

neutron scattered at ϑ. Those neutrons are reflected at $2\vartheta_A$ and those with a particular wavevector $\mathbf{k}_f$ are counted by the detector, which is an ^{3}He tube.

The measurements were performed using the PG(0 0 2) monochromator, performing constant Q scans with $k_f = 2.6625$ Å^{-1}. The scattered and the analyzed beam was collimated using $\alpha_2 = 60'$ and $\alpha_3 = 40'$. In this experiment was used the same sample and sample holder as for BRISP.

6.4 Neutron data analysis

In this section we will briefly discuss the analysis of neutron inelastic scattering data. Our target is the determination of the dynamic structure factor $S(Q, E)$ which is proportional to the double differential cross section. We will focus on the case of TOF instruments, adding some remarks for TAS data reduction.

Time of flight instruments record the number of scattered neutron as a function of the position (the scattering angle ϑ for TOFTOF; the pixel position (x, y) for BRISP) and as a function of the time between the scattering event and the detection. The first step of the data analysis is the conversion of the data to obtain the intensity $I(Q, E)$. Moreover, to compare different datasets the intensities are normalized to their monitor counts. The monitor is a low efficiency detector which is placed on the beam, in front of the sample. The normalization to the monitor counts leads to data independent from the measuring time Δt and from the fluctuation in time of the incident flux.

The measured scattered intensity of the sample inside the cell I^{exp}_{s+c} can be written as:

$$I^{exp}_{s+c} = I_s + I_{ss} + I_{cs} + I_{sc} + I^s_c + I^s_{cc} + I^B_{s+c}; \tag{6.1}$$

where I_{ss} is the intensity due to multiple (double) scattering events involving the sample, I_{sc} and I_{cs} are multiple (double) scattering events between cell and

sample; I_c^s and I_{cc}^s are single and multiple scattering events involving the filled cell, and I_{s+c}^B is the background intensity for the sample plus cell measurement. To obtain the sought quantity, namely the single scattering sample intensity I_s, all these contributes have to be subtracted.

To account for all these factors, in addition to I_{s+c}^{exp} ancillary measurements are needed. These generally are:

- I_s^{exp}, scattering from the empty cell;
- I_{abs}^{exp} scattering from a full absorber (cadmium or B_4C) having the same dimensions of the sample plus container system;
- I_{eb}^{exp}scattering from the environment obtained without any scatterer;
- I_v^{exp}scattering from an elastic incoherent scatterer (Vanadium) to account for instrumental effects and to determine the instrumental resolution.

In the present experiments, together with I_{s+c}^{exp} we have always performed the measure of the empty cell and of the vanadium standard. In general, the background affects all the measurements so it has to be subtracted from I_{s+c}^{exp}, I_c^{exp}, and I_v^{exp}. The background measurement were carried out only at BRISP and IN3 measuring I_{abs} on a B_4C slab. Thanks to the shielding and its peculiar design, I^B (TOFTOF) can be safely neglected [134].

In order to properly subtract the contribution of the cell, we have to account for the attenuating effects due to the sample. The proper transmission coefficient as well as the multiple scattering corrections can be calculated by performing *ad-hoc* MonteCarlo simulations [135, 136].

The single scattering intensity I_s is proportional to the sample double differential cross section but it depends also on the incident flux Φ_0, on some detectors parameter ($\Delta\Omega$, ΔE and the efficiency η) and on the number of scattering cen-

ters N. Therefore I_s reads

$$I_s = \Phi_0 \Delta E \Delta \Omega N \frac{d^2\sigma}{d\Omega dE'} T_s(\vartheta, \omega); \tag{6.2}$$

The scattering transmission $T_s(Q, E)$, which accounts for the attenuation during the scattering processes, can be computed via MC simulations [135, 136]. The vanadium measure (once efficiently corrected by the spurious effects) provides a tool to normalize the data.

Finally, in the case of a coherent scatterer the dynamic structure factor $S(Q, E)$ can be written as:

$$\begin{aligned} \frac{d^2\sigma}{d\Omega dE'} &= \frac{k_f}{k_i}\left[\frac{\sigma_{coh}}{4\pi} S(Q,E) + \frac{\sigma_{inc}}{4\pi} S_s(Q,E)\right] \\ &= \frac{k_f}{k_i}\left[\frac{\sigma_{coh}}{4\pi} S(Q,E)\right] \end{aligned} \tag{6.3}$$

However, these quantities are convoluted with the instrumental resolution. The instrumental resolution $R(Q, E)$ is given by the vanadium spectrum.

In the case of TAS measurements, the scattered intensity is directly proportional to the $S(Q, E)$ and immediately accessible during the experiment without the necessity of mapping between different spaces. The standard data analysis for a TAS instrument is detailed in ref. [137]. The resolution function is described in the quadri-dimensional reciprocal space [138]. The constant-amplitude contours for the resolution function form a set of nested ellipsoids in $(\mathbf{Q}, E)$ space and for a particular spectrometer configuration the details of these ellipsoids depend only on the particular $(\mathbf{Q}_0, E_0)$ point. Therefore, the instrumental resolution function has to be calculated using the know instrument parameters and checked against the measured experimental one [138].

6.5 Experimental results

The use of three different instrument allows to cover broad region of the (Q, E) plane with different resolutions. Where instruments overlap we can obtain com-

plementary information overcoming the limitations of the single data set. Table 6.2 shows the available Qs for each instrument and the overlap regions.

BRISP	$\left(\text{Å}^{-1}\right)$	0.2	0.3	0.4	0.5	0.6	0.7	0.8	0.9	1.0	1.1	1.2	1.3	1.4	1.5
TOFTOF	$\left(\text{Å}^{-1}\right)$	0.2	0.3	0.4	0.5	0.6	0.7	0.8	0.9	1.0	1.1	1.2	1.3	1.4	1.5
IN3	$\left(\text{Å}^{-1}\right)$	0.2	0.3	0.4	0.5										

Table 6.2: Q ranges spanned by the three instruments.

Figure 6.8 reports a selection of spectra obtained with the three instruments at two different wave vectors; figure 6.9 shows a selection of spectra obtained in the high Q region where only TOFTOF and BRISP are available.

The measured intensity can be written as

$$I(Q,\omega) = I_0(Q)\, R(\omega) \otimes \left\{ S(Q,\omega)\, \frac{\hbar\omega}{K_B T} \left[n(\omega,T) + 1 \right] \right\}, \tag{6.4}$$

where $S(Q,\omega)$ is the classic dynamical structure factor, multiplied for the $\frac{\hbar\omega}{K_B T}\left[n(\omega,T)+1\right]$ in order to fulfill the detailed balance condition, with $n(\omega,T)$ the Bose-Einstein factor. $R(\omega)$ is the proper instrumental resolution. The parameter $I_0(Q)$ is a scale parameter which depends on the instrument.

A first guess for the model function $S(Q,\omega)$ could be the usual sum of a delta function for the elastic component plus two inelastic components modeled with two damped harmonic oscillators, namely

$$\begin{aligned} S(Q,\omega) = \quad & A_{el}\delta(\omega) \\ & + \frac{A_1}{\pi} \frac{\Omega_1^2(Q)\,\Gamma_1(Q)}{\left[\omega^2 - \Omega_1^2(Q)\right]^2 + \omega^2 \Gamma_1^2(Q)} \\ & + \frac{A_2}{\pi} \frac{\Omega_2^2(Q)\,\Gamma_2(Q)}{\left[\omega^2 - \Omega_2^2(Q)\right]^2 + \omega^2 \Gamma_2^2(Q)}. \end{aligned} \tag{6.5}$$

The subscripts 1 and 2 label the inelastic modes, respectively the highest energy one and the lowest energy one. The model function eq. 6.5 comprises seven

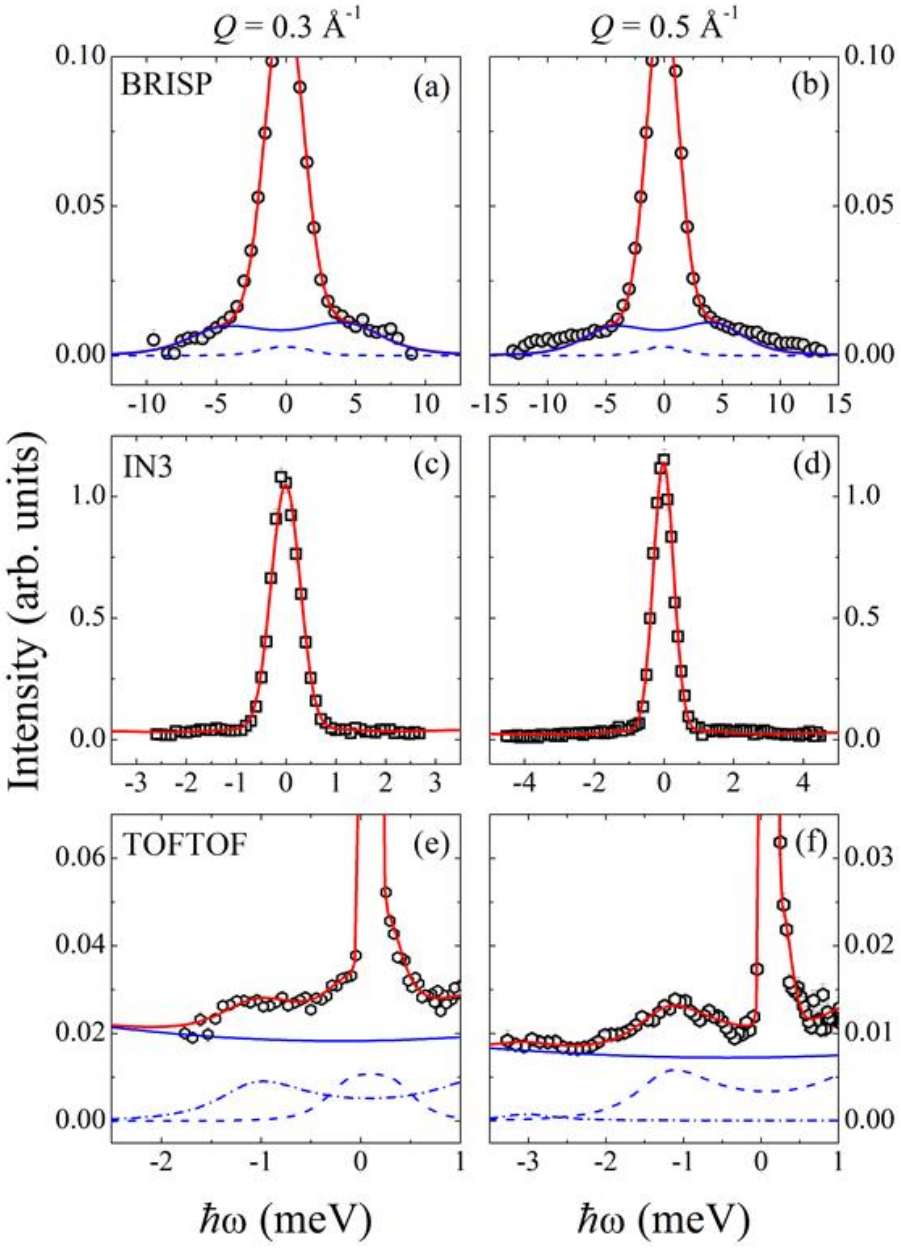

Figure 6.8: Inelastic neutron scattering spectra measured at two selected Q; Q = 0.3 Å^{-1}, left panels ((a), (c), and (e)); $Q = 0.5$ Å^{-1}, right panels ((b), (d), and (f)); (a) and (b) are measured on BRISP; (c) and (d) on IN3; (e) and (f) on TOFTOF. The red line is the best fit whereas the blue line are the inelastic component described in the text: 1 (solid line), 2 (dashed line) 3 (dash-dotted line).

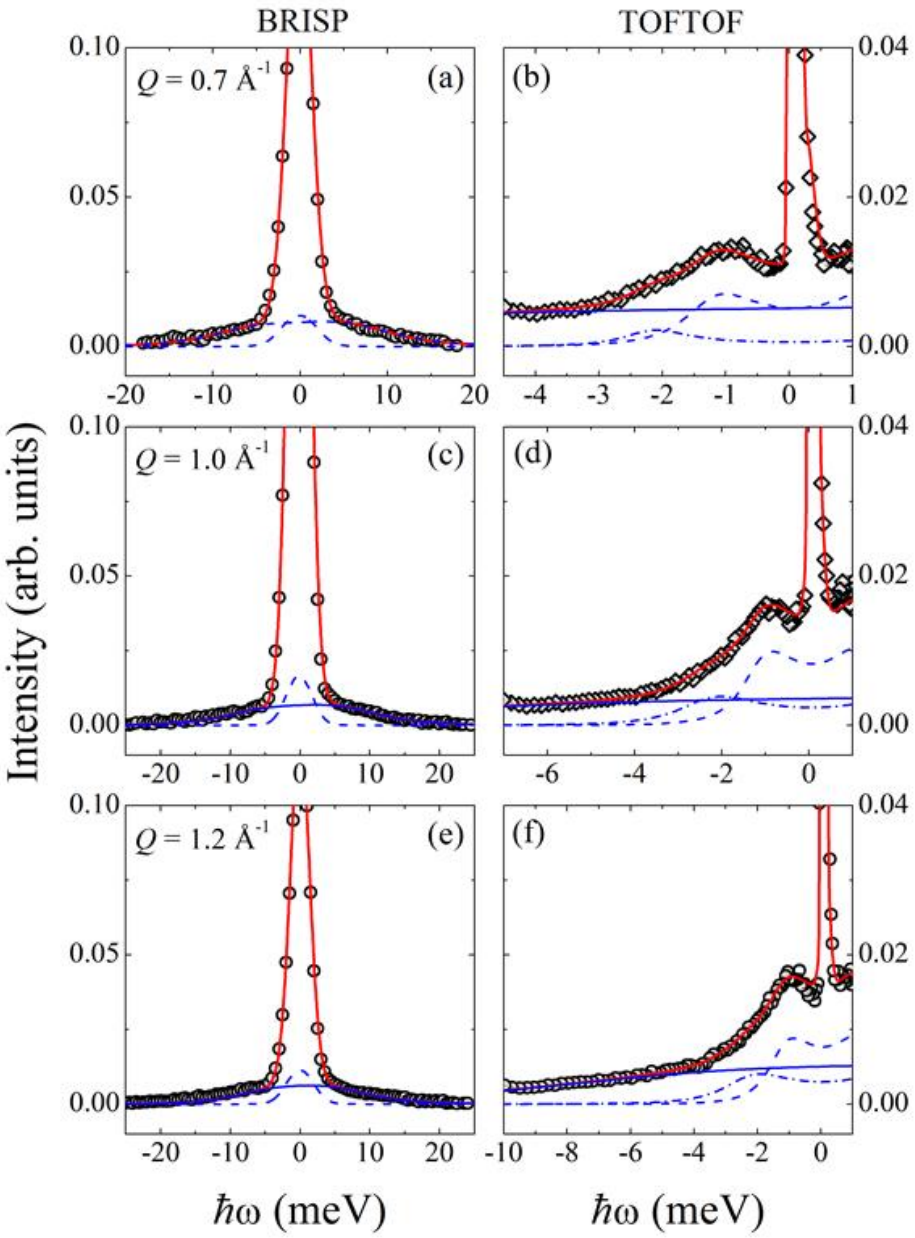

Figure 6.9: Inelastic neutron scattering spectra measured with two different instruments: (a), (c), and (e) are measured on BRISP whereas (b), (d), and (f) are measured on TOFTOF. Spectra reported in (a) and (b) are measured at $Q = 0.7$ Å^{-1}; (c) and (d) at $Q = 1.0$ Å^{-1}; (e) and (f) at $Q = 1.3$ Å^{-1}. The red line is the best fit whereas the blue line are the inelastic component described in the text: 1 (solid line), 2 (dashed line) 3 (dash-dotted line).

parameters: the intensity of the elastic line A_{el}, the intensity A_i, position Ω_i, and damping parameter Γ_i of the inelastic components, $i = 1, 2$. The scale factor $I_0(Q)$ depends on the instrument. Conversely the intensity $A_{el}(Q)$, $A_1(Q)$ and $A_2(Q)$ are equal for the three instruments. As a matter of fact, since the static structure factor $S(Q)$ is the energy integral of the total intensity, they are not independent.

Despite the large numbers of parameters, the availability of data with different resolutions and different kinematic ranges allows an accurate determination of the free parameters from an overall fitting procedure. As it can be seen from table 6.2, in the Q range $0.2 \div 0.5$ all the three instruments are available. For Q in the range $0.6 \div 1.5$ only BRISP and TOFTOF data are present.

When data measured with more than one instrument are available they are fitted using the same set of parameters, apart from the scale factor I_0. In this way each parameter is accurately determined by a fit as much as possible independent on the starting values and with a reduced number of free parameters. Doing this, the high-resolution TOFTOF data provide an accurate determination of the frequency and width of the low energy DHO whereas BRISP and IN3 spectra are more sensitive to the high energy component. This combined use of the data allows for a safe determination also of the inelastic intensities.

The model introduced with eq. 6.5 is a rather common assumption for glasses, and it has been successfully applied to several systems, *e.g.* [122, 113, 139, 112]. In this case it does not work properly. The first DHO is easily modeled using BRISP data whereas the second one is more problematic. As a matter of fact the clear inelastic peak visible in TOFTOF data cannot be reproduced by the model function, see figure 6.10.

A complete analysis of TOFTOF spectra suggests the existence of an intensity excess on the tail of the inelastic peak, approximately between -2 and -3 meV. To take into account this feature, we decide to introduce a third DHO

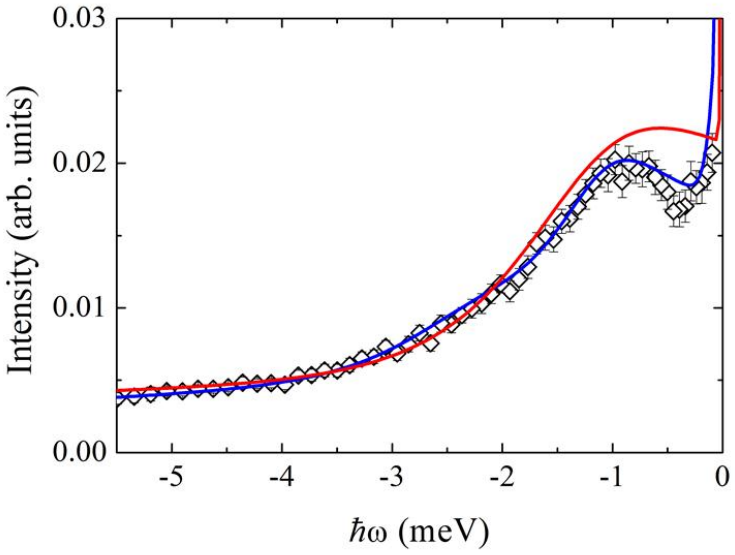

Figure 6.10: Fit of TOFTOF data at $Q = 1.0$ (black diamonds) using the $S(Q,\omega)$ described in eq. 6.5 (red line). It can be seen that the model cannot reproduce the low energy feature of the spectrum. The fit obtained using the model of eq. 6.6 is also reported (blue line).

function and thus performing a new overall fit procedure.

The new model function is:

$$\begin{aligned} S(Q,\omega) = \quad & A_{el}\delta(\omega) \\ & + \frac{A_1}{\pi} \frac{\Omega_1^2(Q)\,\Gamma_1(Q)}{\left[\omega^2 - \Omega_1^2(Q)\right]^2 + \omega^2\Gamma_1^2(Q)} \\ & + \frac{A_2}{\pi} \frac{\Omega_2^2(Q)\,\Gamma_2(Q)}{\left[\omega^2 - \Omega_2^2(Q)\right]^2 + \omega^2\Gamma_2^2(Q)} \\ & + \frac{A_3}{\pi} \frac{\Omega_3^2(Q)\,\Gamma_3(Q)}{\left[\omega^2 - \Omega_3^2(Q)\right]^2 + \omega^2\Gamma_2^3(Q)}. \end{aligned} \tag{6.6}$$

where the parameters are defined as for eq. 6.5.

The results of this fit are reported in figure 6.8 using data from all the instruments and in figure 6.9 where only BRISP and TOFTOF data are available. In both cases there is a good agreement between the model. The meaning of these three DHOs will be discussed in the following sections.

6.6 Nature of the modes in vitreous $SiSe_2$

The dispersion relation for the three modes is reported in in figure 6.11.

The high frequency mode $\Omega_1(Q)$ shows all the typical features of a longitudinal acoustic mode. The maximum of the dispersion curve occurs around $Q_m^{(1)} \simeq 1$ Å^{-1}, which is about $Q_1/2$, where Q_1 is the position of the first sharp diffraction peak in $S(Q)$, see figure 6.4. Above $Q_m^{(1)}$ the dispersion curve decrease. The slope of the low Q rise is compatible with the maximum valuee of the BLS sound velocity [130]. The low Q slope of the mode dispersion, determined by a linear fit of the first four points gives a velocity of $v_1 = 2590 \pm 80$ m/s, which is $\sim 20\%$ higher than 2170 m/s, the maximum extimated value by BLS [130]. Figure 6.12 shows the generalized sound velocity v_1 calculated as

$$v_1 = \frac{\Omega_1(Q)}{Q} \tag{6.7}$$

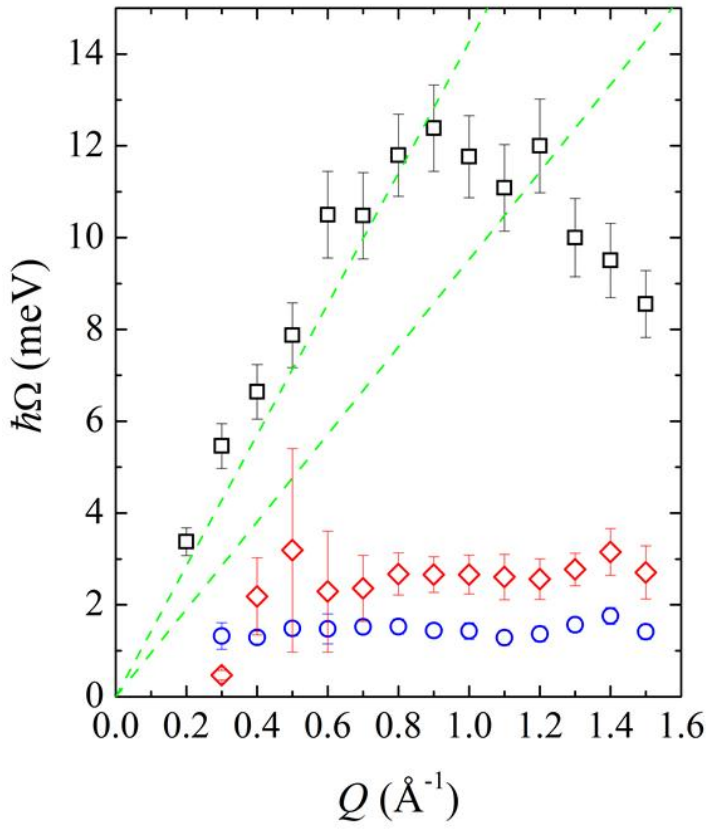

Figure 6.11: Dispersion curves for the three excitation of eq. 6.6; Ω_1 (black open squares), Ω_2 (red open diamonds), Ω_3 (blue open circles). The green dashed lines are the maximum and minimum BLS sound velocity reported in section 6.2.

The sound velocity is almost constant for $Q \leq 0.6$ Å^{-1} then it starts to decrease. This high frequency mode $\Omega_1(Q)$ can be associated to the high Q evolution of the longitudinal acoustic mode.

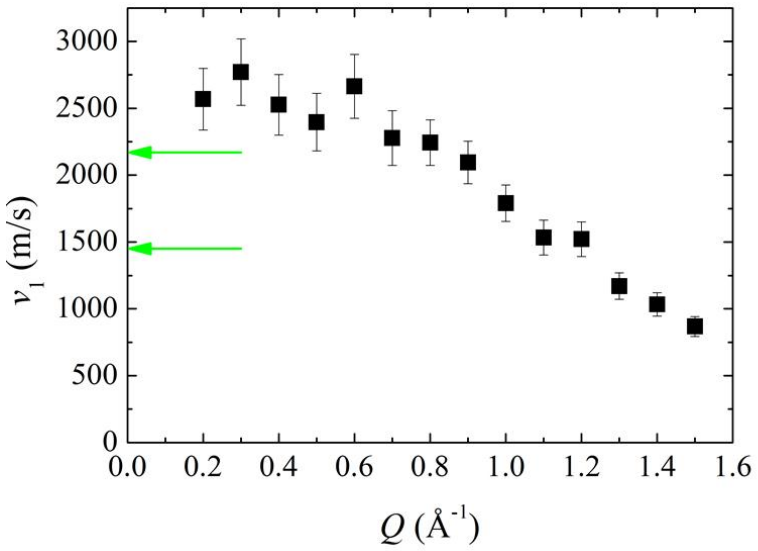

Figure 6.12: Generalized sound velocity calculated as described in the text. The green arrows mark the maximum and the minimum sound velocity obtained by BLS, [130], representing the continuum limit.

The lowest energy excitation $\Omega_3(Q)$ displays an oscillating behavior. Figure 6.13(a) shows the behavior of $\Omega_3(Q)$. The oscillation is highlighted with the red dashed line. The Q evolution of this feature is clearly visible also in the experimental data, as reported in figure 6.13(b).Increasing Q from 0.6 to 1.3 Å^{-1} the peak oscillates with a maximum around 1.0 Å^{-1}. The minimum of the oscillation is located at about $Q \sim 1.0$ Å^{-1}, and it seems related to the first peak in the diffraction pattern, namely the concentration pre-peak at $Q_{pp} = 0.96$ Å^{-1}.

The intermediate frequency excitation $\Omega_2(Q)$ has a more evident optic-like behavior with an almost constant energy $E_2 \simeq 2.6$ meV, see fig. 6.14(a). The existence of this third excitation is highlighted in figure 6.14(b), where the TOFTOF spectrum is presented after the subtraction of the longitudinal in-

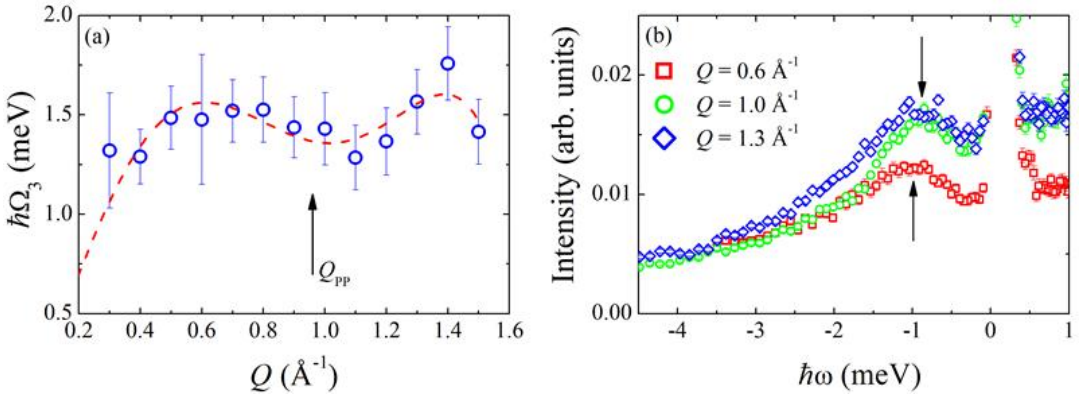

Figure 6.13: (a) Dispersion relation for $\Omega_2(Q)$; the black arrow marks the position of Q_{pp}, the pre-peak in the structure factor. The red dashed line is a guide for the eye which highlights the oscillating behavior $\Omega_2(Q)$. In (b) we report three selected TOFTOF spectra displaying the evident oscillation of the peak associated to $\Omega_2(Q)$. The peak position is marked by two black arrows.

elastic component, which is fitted using BRISP data. The low energy side of the inelastic peak associated to $\Omega_3(Q)$ is characterized by a bump corresponding to $\Omega_2(Q)$.

The damping parameters of the presented modes are reported in figure 6.15(a). At low Q, up to about 0.6 Å^{-1}, $\Gamma_1(Q)$ follows a Q^2 behavior. Figure 6.15(b), (c), and (d) show the ration between the damping parameter and the branch frequency. The first mode appears to be overdamped for $Q > 0.6$. In general, Γ/Ω rise to a constant value above 0.6 Å^{-1}, then $\Gamma(Q)$ follows the same periodicity of $\Omega(Q)$, *i.e.* there are no structural effects on the damping.

The natural question which can rise at this point is: *what kind of excitation are* $\Omega_2(Q)$ *and* $\Omega_3(Q)$*?*

As a matter of fact we are dealing with a system which exhibits three excitations, among which two show a propagating behavior, even if with different periodicities.

Neutron scattering experiments performed in the first Brillouin zone can

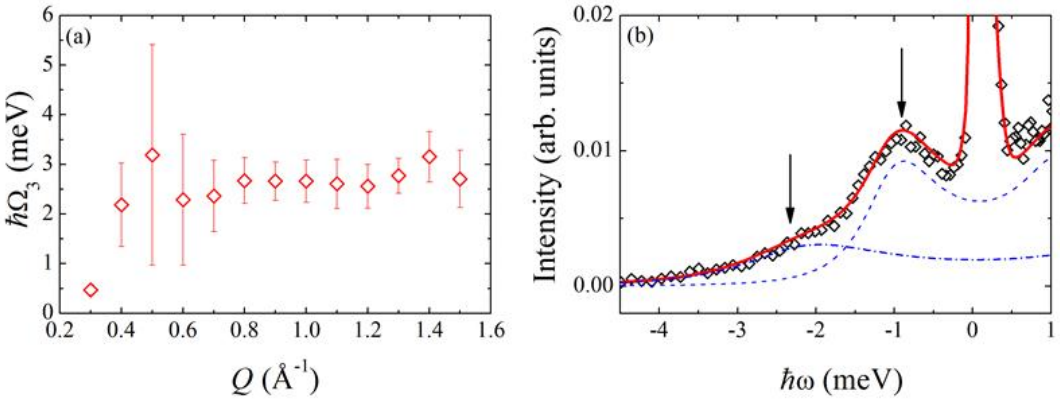

Figure 6.14: (a) Dispersion relation for $\Omega_3(Q)$ (a). In (b) we report a TOFTOF spectrum after the subtraction of the longitudinal contribution. The red line is the best fit whereas the blue dashed and dash dotted line are the second and the third excitations; the two corresponding peaks are marked with black arrows.

probe only the longitudinal dynamics. However, as the wavevector is increased, topologically disordered system can lose their symmetry so that *longitudinal* and *transverse* lose their precise meaning. The visibility of a transverse excitation in the neutron spectra can thus be justified by the mixing phenomenon [140, 69]. The high frequency transverse dynamics acquire also a longitudinal component which is thus visible in the scattering signal.

A further clue on the character of second and third excitations can be inferred considering the intensity Q-behavior, as proposed by Leadbetter [24]. As a matter of fact the scattering intensity in the case of one phonon scattering is modulated by a polarization factor $\mathbf{Q} \cdot \mathbf{e}^j$, where $\mathbf{e}^j$ is the polarization vector of the mode. In general, for purely transverse mode and purely longitudinal mode it displays an antiphase behavior:

$$I(Q,\omega) \propto \begin{cases} cos^2\phi & \text{purely longitudinal modes} \\ sin^2\phi & \text{purely transverse modes} \end{cases}, \tag{6.8}$$

where ϕ is the angle between $\mathbf{Q}$ and $\mathbf{e}^j$. In polycrystals this leads to a maximum of the longitudinal intensity for $Q = \tau \pm q$ where τ is a vector of the reciprocal

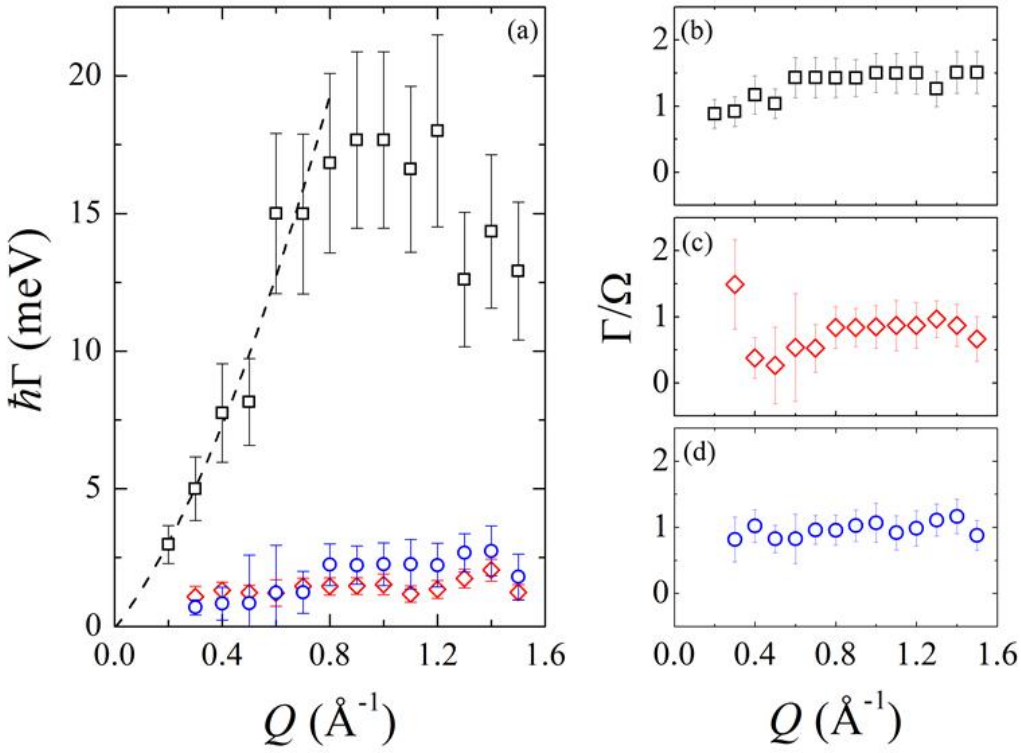

Figure 6.15: The damping parameter $\Gamma(Q)$ is reported in (a) for the first mode (black open squares), the second (red open diamonds), and the third (blue open circles); the black dashed line represent the Q^2 behavior of the first mode. In (b) (c) (d) we report the ratio $\Gamma(Q)/\Omega(Q)$ for the three excitations; symbols are as in (a).

lattice and q the phonon wavector ($q \in 1BZ$). On the other hand, for a purely transverse phonon the intensity will be maximum at $Q = \tau$ [24].

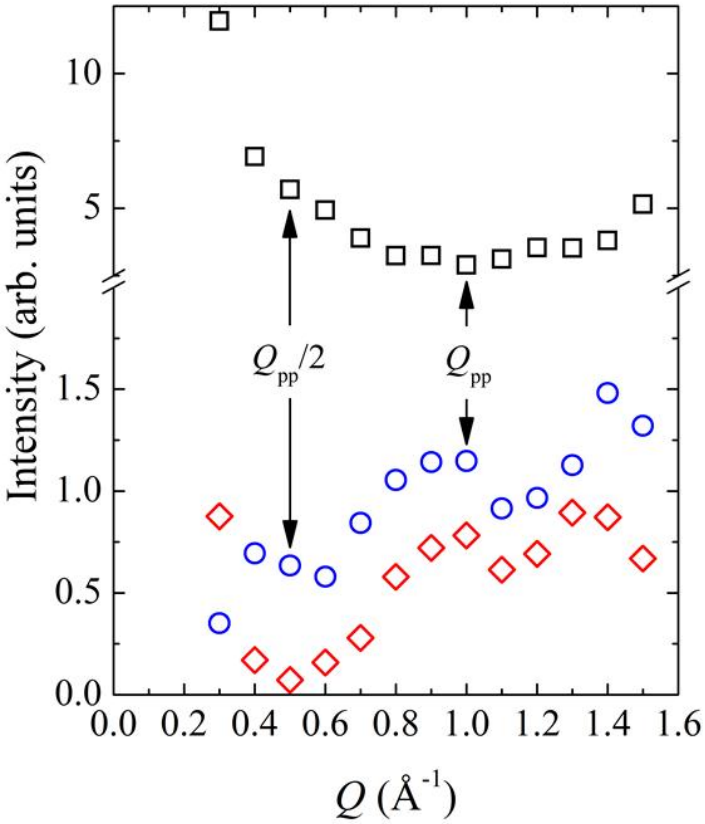

Figure 6.16: Intensities of the three components; the first is reported with open black squares, the second with open red diamonds and the third with open magenta circles. The arrows mark the position of the prepeak in the static structure factor Q_{pp} and of $Q_{pp}/2$.

Figure 6.16 shows a comparison between the intensity of the three modes. The second and the third excitation have the same Q behavior and they are both in anti-phase with respect to the first mode. Any further consideration have to account for the different periodicity of the branches. Anyway this findings could suggest the idea of a transverse acoustic nature for both $\Omega_2(Q)$ and $\Omega_3(Q)$.

Summarizing we have presented a glass which displays a crystal-like behavior

having three acoustic branches. However: *is it still a glass?*

Figure 6.17 shows the static structure factor $S(Q)$ measured by neutron diffraction in ref. [129] compared to $\alpha S_T(Q)$, where α is an instrument dependent normalization factor and

$$S_T(Q) = \int_{E_T^{min}(Q)}^{E_T^{max}(Q)} dE I_s^T(Q,E)\,. \tag{6.9}$$

The patterns are in good agreement; furthermore, the integrated intensity does not present any trace of Bragg peaks ruling out the crystallization as origin of the third sound. In the same figure we report also the total intensity $I_{el}+I_1+I_2+I_3$ multiplied for a normalization factor which also shows the same behavior of the static structure factor.

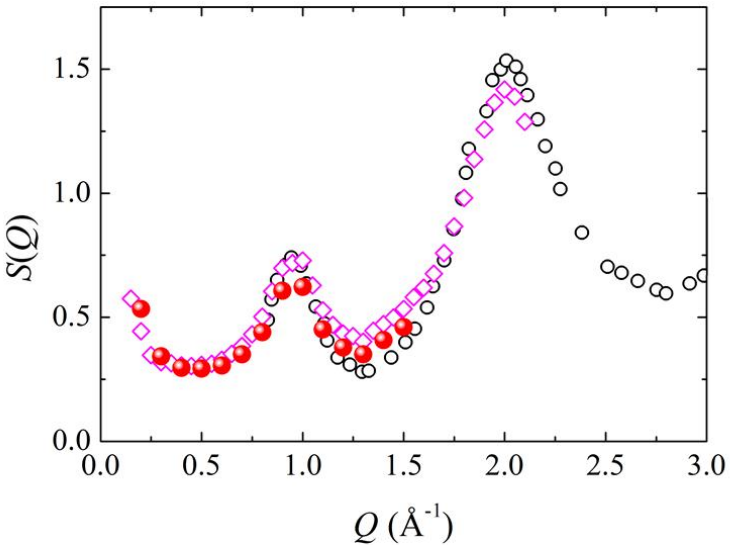

Figure 6.17: Comparison between the total integrated intensity (red bullets) and the static structure factor from ref. [129]. The blue open diamond reports the integrated intensity of the TOFTOF spectra, 6.9. It is worth to note that no Bragg peaks are visible.

A possible explanation of this quite astonishing crystal-like behavior could be tracked in the structure of v-$SiSe_2$. As a matter of fact the silicon diselenide is

formed by edge sharing covalently bounded tetrahedra. This atomic linkage leads to the formation of rather long monodimensional chains. These chains are joined by corner sharing tetrahedra [126, 127] or van der Waals bounds [124, 125]. The final structure is considered an example of a glass which exhibiting a strong medium range order [127] and this is supported by the very similar Raman spectrum of both glass and crystal [125, 125]. The explanation of the different periodicity felt by the longitudinal excitation and that exhibits by Ω_3 is still pending. As a matter of fact they seems affected by two different peaks in the $S(Q)$.

6.7 Transverse branches and the boson peak

To conclude this discussion about the dynamical properties of vitreous $SiSe_2$ we can compute the generalized vibrational density of states to have a look to the boson peak in this system.

The *generalized* vibrational density of states of a coherent scatterer can be calculated in the framework of the incoherent approximation. The incoherent approximation assumes that the interference term in the coherent scattering function averages to zero at relatively high Q, hence the $S(Q,\omega)$ can be described in terms of an average atom, which scatters only incoherently. In this case, even using the highest available Q, the incoherent approximation is not strictly fulfilled. Nonetheless we can calculate an approximated generalized VDOS. It is worth to note that the term generalized is used to emphasize that this is not the true density of states, but its reflection in the scattering, weighted by the cross sections and masses of the atoms in the sample.

Figure 6.18(a) shows the measured dispersion relation for the three branches whereas in figure 6.18(b) is reported the vibrational density of states $g(\hbar\omega)$. The main contribute to the vibrational mode excess is clearly given by the lowest

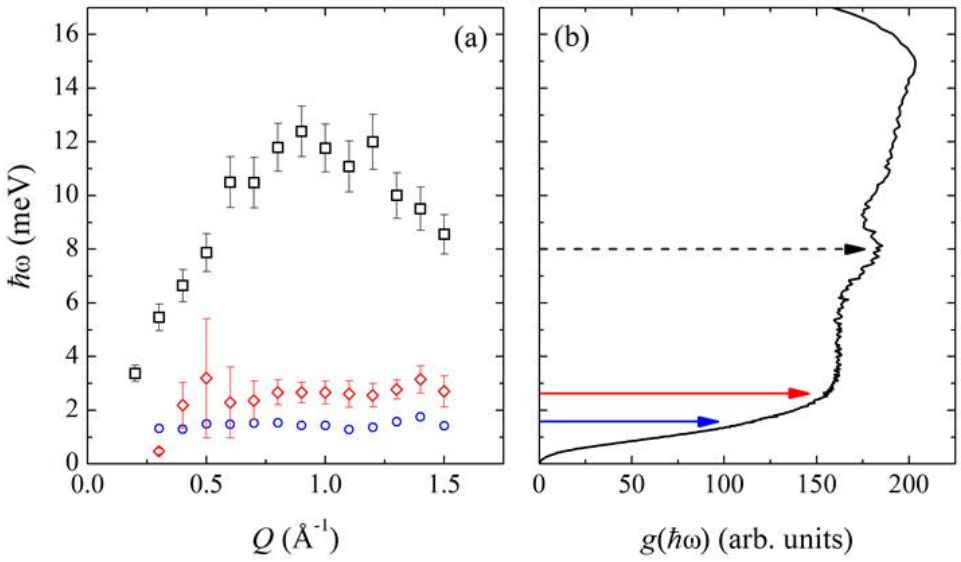

Figure 6.18: (a) Dispersion relation compared to the vibrational density of states as obtained by neutron scattering (b). The red and blue lines represent the mean energies of the two transverse branches. The black dashed line suggest a connection between the bump in the vibrational density of states and the minimum of the longitudinal branch.

transverse branch. The bump visible around 8 meV could be due to the minimum of the longitudinal branch at $Q = 1.5$ Å^{-1}.

The reduced VDOS $g(\omega)/\omega^2$ is reported in figure 6.19. The peak position is $E_{BP} = 0.78 \pm 0.01$ meV.

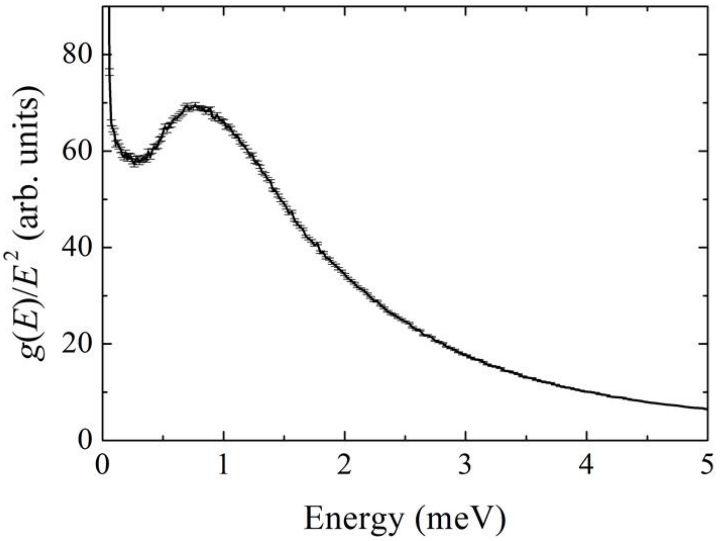

Figure 6.19: The reduced density of states in $g(\omega)/\omega^2$.

6.7.1 The Raman light-vibration coupling function

According to the approach by Galeener and Sen [75], the experimental intensity in the case of first-order Raman scattering on a disordered system for a Stokes process it is given by eq. 3.1, namely:

$$I^{Raman}(\omega) = C(\omega)g(\omega)\frac{[n(\omega,T)+1]}{\omega}. \tag{6.10}$$

Dividing by the Bose-Einstein population factor $[n(\omega,T)+1]$ and by ω we obtain the so-called reduced density of states which is proportional to the reduced density of states $g(\omega)/\omega^2$ through the coupling function $C(\omega)$. Neutron scattering data allows the determination of a generalized VDOS, thus the coupling function $C(\omega)$ could be determined by the ratio between Raman and neutron

data. The result of this division is reported in figure 6.20. As highlighted by the fit, the coupling function results linear in the boson peak region. This finding further confirms the general results of $C(\omega) \sim \omega$ in the BP region already found in many systems [78, 79, 80, 81].

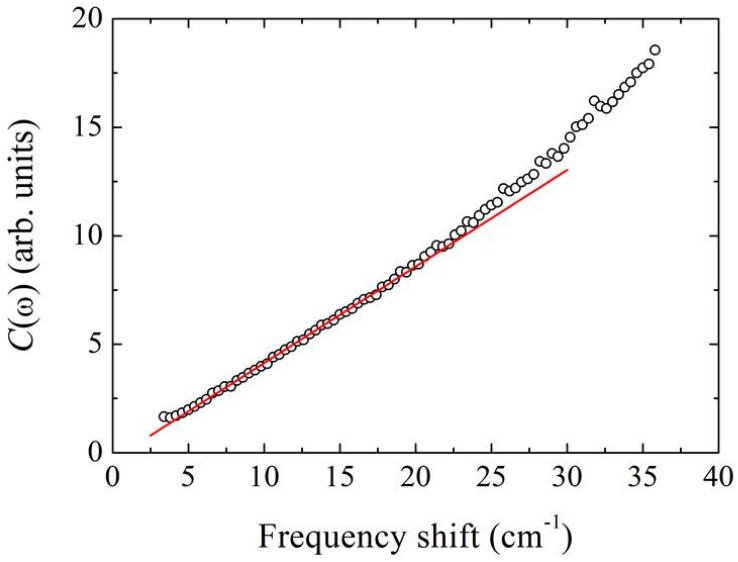

Figure 6.20: Light to vibration coupling function obtained as described in the text. The red line is a linear fit in the BP region.

Chapter 7

Conclusions

Non si può cavare il sangue da una rapa.

Italian proverb

In this work we have analyzed the dynamics and structural properties of two glasses: permanently densified silica and silicon diselenide.

Permanently densified v-SiO_2 samples have been obtained by using a high pressure high temperature apparatus achieving a densification up to the 22%. The vibrational density of states has been measured by means of Raman scattering. We have found that the peak shifts upwards in frequency and it decreases in intensity however, at least in a 10% of densification range, the BP shape is invariant and its evolution is only due to the peak shift. The peak shift has been thus compared to the modification of the elastic medium described by the Debye frequency ω_D showing a stronger than Debye behavior. The structural modifications induced by the densification have been investigated by means of positron annihilation lifetime spectroscopy (PALS). This gives us a *in-situ* information on the dimensions of the interstitial voids in the glassy network. PALS and neutron diffraction data support the idea that the densification does not act on the short range order, *i.e.* the $Si\left(O_{1/2}\right)_4$ tetrahedra, but on the medium

range region. As a matter of fact, tetrahedera rotate to fill the void spaces thus explaining the heavy shrink observed. The voids' radii have also been used to reproduce the position and evolution of the first sharp diffraction peak, pointing out their importance within the organization of the medium range order.

The evolution of the boson peak in v-SiO_2 has been qualitatively explained in terms of transverse acoustic modes which pile up at the maximum of the dispersion curve. This corresponds to an effective Brillouin zone border which is intimately related to the structure.

A similar relation has also been directly observed by comparing the α-quartz polycrystal with the permanently densified glass at the same density. We have observed the appearance of a peak in the vibrational density of states of the polycrystal which corresponds to the BP in glasses.

Moreover this comparison have also highlighted the existence of a length ξ marking the crossover between a long wavelength elastic regime and a short wavelength microscopic dynamics. In this domain α-quartz polycrystal and glass shows the same behavior.

The finding on v-$SiSe_2$ show the existence of a glass with crystal-like behavior. Its rather low sound velocity allows a low Q investigation of the dynamics by means of neutron inelastic scattering. Silicon diselenide shows three low energy excitations: a longitudinal acoustic mode and two transverse-like excitations. This crystal-like behavior can be qualitatively explained considering the peculiar edge sharing structure which exhibits a relevant medium range order. The comparison of the vibrational density of states to the dispersion curves shows that the main contribution in the BP region arises from the transverse excitations.

In conclusion we have add some new proofs able to shed some new light on the long standing questions of the origin of the boson peak. In any case many aspects of this work require further investigations. In particular, the existence

of glasses exhibiting a crystal-like behavior as well as the existence of the correlation length ξ have to be clarified even in the more fundamental scenario of the glass transition.

References

1. S. Caponi, M. Zanatta, A. Fontana, L. E. Bove, L. Orsingher, F. Natali, C. Petrillo e F. Sacchetti; Ergodicity breaking in strong and network-forming glassy systems, Phys. Rev. B **79**, 172201 (2009).

2. M. Zanatta, G. Baldi, S. Caponi, A. Fontana, E. Gilioli, M. Krisch, C. Masciovecchio, G. Monaco, L. Orsingher, F. Rossi, G. Ruocco, and R. Verbeni; Elastic properties of permanently densified silica: a Raman, Brillouin light, and x-ray scattering study, Phys. Rev. B **81**, 212201 (2010).

3. M. Zanatta, A. Fontana, F. Rossi and E. Gilioli; Effects of permanent densification on the vibrational density of states of vitreous silica, J. of Non Cryst. Solids **357**, 1892 (2011).

4. S. Caponi, A. Fontana, F. Rossi and M. Zanatta; Influence of temperature on the quasi-elastic scattering in v-GeO2 glass, Phil. Mag. **91**, 1887 (2011).

5. F. Rossi, G. Baldi, S. Caponi, R. Dal Maschio, A. Fontana, L. Orsingher and M. Zanatta; The vibrational dynamics of v-GeO2 at the glass transition: a Raman and Brillouin scattering study, Phil. Mag. **91**, 1910 (2011).

6. M. Zanatta, C. Armellini, A. Fontana and F. Rossi; Temperature evolution of the boson peak and Debye scaling in vitreous B_2O_3, Phil. Mag. **91**, 2028 (2011).

7. M. Zanatta, G. Baldi, S. Caponi, A. Fontana, C. Petrillo, F. Rossi, and F. Sacchetti; Debye to non-Debye scaling of the Boson Peak dynamics: critical behavior and local disorder in vitreous Germania, J. Chem. Phys. **135**, 174506 (2011).

Bibliography

[1] C.A. Angell, P.H. Poole, and J. Shao. Glass-forming liquids, anomalous liquids and polyamorphism in liquids and biopolymers. *Nuovo Cimento D*, 16:993, 1994.

[2] C.A. Angell. The old problem of glass and the glass transition, and many new twist. *Proc. Natl. Acad. Sci. USA*, 92:6675, 1995.

[3] A. Cavagna. Supercooled liquids for pedestrians. *Phys. Rep.*, 476:51, 2009.

[4] P.G. Debenedetti and F.H. Stillinger. Supercooled liquids and the glass transition. *Nature*, 410:259, 2001.

[5] K. Binder and W. Kob. *Glassy materials and disordered solids - An introduction to their statistical mechanics.* World Scientific, revised edition, 2011.

[6] S.R. Elliott. *Physics of amorphous materials.* Longman Scientific & Technical, second edition, 1990.

[7] J.C. Dyre. Colloquium: the glass transition and elastic models of glass-forming liquids. *Rev. Mod. Phys.*, 78:953, 2006.

[8] M.D. Ediger, C.A. Angell and S.R Nagel. Supercooled liquids and glasses. *J. Phys. Chem.*, 100:13200, 1996.

[9] T. Scopigno, G. Ruocco, F. Sette, and G. Monaco. Is the Fragility of a liquid embedded in the properties of its glass? *Science*, 302:849, 2003.

[10] R. Böhmer, K.L. Ngai, C.A. Angell, and J. Plazek. Nonexponential relaxations in strong and fragile glass formers. *J. Chem. Phys.*, 99:4201–4209, 1993.

[11] W.H. Zachariasen. The atomic arrangement in glasses. *J. Am. Chem. Soc.*, 54:3841, 1932.

[12] S.R. Elliott. Medium range structural order in covalent amorphous solids. *Nature*, 354:445, 1991.

[13] P.S. Salmon, R.A. Martin, P.E. Mason, and G.J. Cuello. Topological versus chemical ordering in network glasses at intermediate and extended length scales. *Nature*, 435:75, 2005.

[14] P.S. Salmon. The structure of tetrahedral network glass forming systems at intermediate and extended length scales. *J. Phys.: Condens. Matter*, 19:455208, 2007.

[15] S. Caponi, M. Zanatta, A. Fontana, L. E. Bove, L. Orsingher, F. Natali, C. Petrillo, and F. Sacchetti. Ergodicity breaking in strong and network-forming glassy systems. *Phys. Rev. B*, 79:172201, 2009.

[16] L. Berthier and G. Biroli. Theoretical perspective on the glass transition and amorphous materials. *Rev. Mod. Phys.*, 78:953–972, 2006.

[17] A.C. Wright. Neutron scattering from vitreous silica. V. The structure of vitreous silica: What have we learned from 60 years of diffraction studies? *J. Non-Cryst. Solids*, 179:84, 1994.

[18] S.R. Elliott. The origin of the first sharp diffraction peak in the structure factor of covalent glasses and liquids. *J. Phys. Condens. Matter*, 4:7661, 1992.

[19] J. Du and L.R. Corrales. First sharp diffraction peak in silicate glasses: Structure and scattering length dependence. *Phys. Rev. B*, 72:092201, 2005.

[20] Q. Mei, C.J. Benmore, S. Sen, R. Sharma, and J.L. Yarger. Intermediate range order in vitreous silica from a partial structure factor analysis. *Phys. Rev. B*, 78:144204, 2008.

[21] S.R. Elliott. Origin of the first sharp diffraction peak in the structure factor of covalent glasses. *Phys. Rev. Lett.*, 67:711, 1991.

[22] A.A. Maraudin, E.W. Montroll, G.H. Weiss, and I.P. Ipatova. *Theory of lattice dynamics in the harmonic approximation.* Academic press, second edition, 1971.

[23] O. Madelung. *Introduction to solid state physics.* Springer Berlin Heidelberg, third edition, 2008.

[24] A.J. Leadbetter. Structure and atomic motion in glasses. In B.T.M. Willis, editor, *Chemical Applications of Thermal Neutron Scattering*, chapter 7. Oxford University Press, 1973.

[25] F. Sette, M.H. Krisch, C. Masciovecchio, G. Ruocco, and G. Monaco. Dynamics of glasses and glass-forming liquids studied by inelastic X-ray scattering. *Science*, 280:1550, 1998.

[26] S. Takeno and M. Goda. A theory of phonons in amorphous solids and its implication to collective motion in simple liquids. *Prog. Theor. Phys.*, 45:331, 1971.

[27] S. Takeno and M. Goda. A theory of phonon-like excitations in non-crystalline solids and liquids. *Prog. Theor. Phys.*, 47:790, 1972.

[28] R. Vacher, E. Courtens, and M. Foret. Anharmonic versus relaxational sound damping in glasses. II. Vitreous silica. *Phys. Rev. B*, 72:214205, 2005.

[29] C. Masciovecchio, G. Baldi, S. Caponi, L. Comez, S. Di Fonzo, D. Fioretto, A. Fontana, A. Gessini, S.C. Santucci, F. Sette, G. Viliani, P. Vilmercati, and G. Ruocco. Evidence for a crossover in the frequency dependence of the acoustic attenuation in vitreous silica. *Phys. Rev. Lett.*, 97:035501, 2006.

[30] T. Tohei, A. Kuwabara, F. Oba, and I. Tanaka. Debye temperature and stiffness of carbon and boron nitride polymorphs from first principles calculations. *PhyS. rev. B*, 73:064304, 2006.

[31] K. Huang. *Statistical Mecchanics*. John Wiley & Sons, second edition, 1987.

[32] N.W. Ashcroft and N.D. Mermin. *Solid State Physics*. Harcourt College Publishers, 1976.

[33] R.C. Zeller and R.O. Pohl. Thermal conductivity and specific heat of noncrystalline solids. *Phys. Rev. B*, 4:2029, 1971.

[34] E. Fabiani, A. Fontana, and U. Buchenau. Neutron scattering study of the vibrations in vitreous silica and germania. *J. Chem. Phys.*, 128:244507, 2008.

[35] W. Doster, S. Cusack and W. Petry. Dynamical transition of myoglobin revealed by inelastic neutron scattering. *Nature*, 337:205106, 1989.

[36] L. Hong, B. Begen, A. Kisliuk, C. Alba-Simionesco, V.N. Novikov, and A.P. Sokolov. Pressure and density dependence of the boson peak in polymers. *Phys. Rev. B*, 78:134201, 2008.

[37] S.N. Taraskin, Y. L. Loh, G. Natarajan, and S.R. Elliott. Origin of the boson peak in systems with lattice disorder. *Phys. Rev. Lett.*, 86:1255, 2001.

[38] W. Schirmacher. Thermal conductivity of glassy materials and the boson peak. *Europhys. Lett.*, 73:892, 2006.

[39] W. Schirmacher, G. Ruocco, and T. Scopigno. Acoustic attenuation in glasses and its relation with the boson peak. *Phys. Rev. Lett.*, 98:025501, 2007.

[40] W. Schirmacher, B. Schmid, C. Tomaras, G. Viliani, G. Baldi, G. Ruocco, T. Scopigno. Vibrational excitations in systems with correlated disorder. *Phys. Stat. Sol.*, 5:862, 2008.

[41] T.S. Grigera, V. Martin-Mayor, G. Parisi, and P. Verrocchio. Phonon interpretation of the boson peak in supercooled liquids. *Nature*, 422:289, 2003.

[42] B. Rufflé, D.A. Parshin, E. Courtens, and R. Vacher. Boson peak and its relation to acoustic attenuation in glasses. *Phys. Rev. Lett.*, 100:015501, 2008.

[43] D.A. Parshin, H.R. Schober, and V.L. Gurevich. Vibrational instability, two-level systems, and the boson peak in glasses. *Phys. Rev. B*, 76:064206, 2007.

[44] V.L. Gurevich, D.A. Parshin, and H.R. Schober. Anharmonicity, vibrational instability, and the Boson peak in glasses. *Phys. Rev. B*, 67:094203, 2003.

[45] E. Duval, A. Mermet, and L. Saviot. Boson peak and hybridization of acoustic modes with vibrations of nanometric heterogeneities in glasses. *Phys. Rev. B.*, 75:024201, 2007.

[46] A.P. Sokolov, A. Kisliuk, M. Soltwisch, and D. Quitmann. Medium-range order in glasses: Comparison of Raman and diffraction measurements. *Phys. Rev. Lett.*, 69:1540, 1992.

[47] L. Börjesson, A.K. Hassan, J. Swenson, L.M. Torrel, and A. Fontana. Is there a correlation between the first sharp diffraction peak and the low frequency vibrational behavior in glasses? *Phys. Rev. Lett.*, 70:1275, 1993.

[48] S.W. Lovesey. *Theory of neutron scattering from condensed matter.* Clarendon press Oxford, first edition, 1984.

[49] F. Sette and M. Krisch. Inelastic X-rat scattering from collective atom dynamics. In F. Hippert, E. Geissler, J.L. Hodeau, E. Lelièvre-Berna, and J. Regnard, editor, *Neutron and X-ray Spectroscopy.* Springer, 2006.

[50] T. Scopigno, G. Ruocco, and F. Sette. Microscopic dynamics in liquid metals: The experimental point of view. *Rev. Mod. Phys.*, 77:901, 2005.

[51] G. Ruocco and F. Sette. High-frequency vibrational dynamics in glasses. *J. Phys. Condens. Matter*, 13:9141, 2001.

[52] E. Burkel. Phonon spectroscopy by inelastic x-ray scattering. *Rep. Prog. Phys.*, 63:171, 2000.

[53] J.M. Carpenter and D.L. Price. Correlated motions in glasses studied by coherent inelastic neutron scattering. *Phys. Rev. B*, 54:441, 1985.

[54] D.L. Price and J.M. Carpenter. Correlated motions in glasses studied by coherent inelastic neutron scattering. *Phys. Rev. B*, 54:441, 1985.

[55] A. Messiah. *Quantum Mechanics*. Dover Publications, 1999.

[56] U. Balucani and M. Zoppi. *Dynamics of the liquid state*. Oxford University Press, first edition, 1994.

[57] J.P. Hansen and I.R. McDonald. *Theory of simple liquids*. Academic Press, first edition, 1976.

[58] S. Caponi, A. Fontana, F. Rossi, G. Baldi, and E. Fabiani. Effect of temperature on the vibrational density of states in vitreous SiO_2: a Raman study. *Phys. Rev. B*, 76:092201, 2007.

[59] G. Baldi, A. Fontana, G. Monaco, L. Orsingher, S. Rols, F. Rossi, and B. Ruta. Connection between boson peak and elastic properties in silicate glasses. *Phys. Rev. Lett.*, 102:195502, 2009.

[60] B. Rufflé, S. Ayrinhac, E. Courtens, R. Vacher, M. Foret, A. Wischnewski, and U. Buchenau. Scaling the temperature-dependent boson peak of vitreous silica with the high-frequency bulk modulus derived from Brillouin scattering data. *Phys. Rev. Lett.*, 104:067402, 2010.

[61] M. Zanatta, G. Baldi, S. Caponi, A. Fontana, C. Petrillo, F. Rossi and F. Sacchetti. Debye to non Debye scaling of the boson peak dynamics: Critical behavior and local disorder in v-GeO_2. *J. Chem. Phys.*, 135:174506, 2011.

[62] K. Niss, B. Begen, B. Frick, J. Ollivier, A. Beraud, A.P. Sokolov, V.N. Novikov, and C. Alba-Simionesco. Influence of pressure on the boson peak: Stronger than elastic medium transformation. *Phys. Rev. Lett.*, 99:055502, 2007.

[63] T. Deschamps, C. Martinet, D. de Ligny, J. L. Bruneel, and B. Champagnon. Correlation between boson peak and anomalous elastic behavior in GeO_2 glass: An in situ Raman scattering study under high-pressure. *J. Chem. Phys.*, 134:224503, 2011.

[64] A. Monaco, A. I. Chumakov, G. Monaco, W.A. Crichton, A. Meyer, L. Comez, D. Fioretto, J. Korecki, and R. Rüffer. Effect of densification on the density of vibrational states of glasses. *Phys. Rev. Lett.*, 97:135501, 2006.

[65] L. Orsingher, A. Fontana, E. Gilioli, G. Carini Jr., G. Carini, G. Tripodo, T. Unruh, and U. Buchenau. Vibrational dynamics of permanently densified GeO_2 glasses: Densification-induced changes in the boson peak. *J. Chem. Phys.*, 132:124508, 2010.

[66] A.I. Chumakov, G. Monaco, A. Monaco, W.A. Crichton, A. Bosak, R. Rüffer, A. Mayer, F. Kargl, L. Comez, D. Fioretto, H. Giefers, S. Roitsch, G. Wortmann, M.H. Manghnani, A. Hashur, Q. Williams, J. Balogh, K. Parliński, P. Jochym, and P. Piekarz. Equivalence of the Boson Peak in Glasses to the Transverse Acoustic van Hove Singularity in Crystals. *Phys. Rev. Lett.*, 106:225501, 2011.

[67] S. Caponi, S. Corezzi, D. Fioretto, A. Fontana, G. Monaco, and F. Rossi. Raman-scattering measurements of the vibrational density of states of a reactive mixture during polymerization: effect on the boson peak. *Phys. Rev. Lett.*, 102:027402, 2009.

[68] M. Zanatta, A. Fontana, F. Rossi, and E. Gilioli. Effects of permanent densification on the vibrational density of states of vitreous silica. *J. Phys. Condens. Matter*, 357:1892, 2011.

[69] O. Pilla, S. Caponi, A. Fontana, J.R. Gonsalves, M. Montagna, F. Rossi, G. Viliani, L. Angelani, G. Ruocco, G. Monaco, and F. Sette. The low energy excess of vibrational states in v-SiO2: The role of transverse dynamics. *J. Phys.: Condens. Matter*, 105:025501, 2010.

[70] O. Pilla, L. Angelani, A. Fontana, J.R. Gonsalves, and G. Ruocco. Structural and dynamical consequences of density variation in vitreous silica. *J. Phys.: Condens. Matter*, 105:025501, 2010.

[71] N.V. Surovtsev, V.K. Malinovsky, Y.N. Palýanov, A.A. Kalinin, and A.P. Shebanin. Suppression of fast relaxation and the Raman coupling coefficient in densified silica. *J. Phys. Condens. Matter*, 16:3035, 2004.

[72] Y. Inamura, M. Arai, T. Otomo, N. Kitamura, and U. Buchenau. Density dependence of the boson peak of vitreous silica. *Physica B*, 284:1157, 2000.

[73] S. Sugai and A. Onodera. Medium-Range Order in Permanently Densified SiO2 and GeO2 Glass. *Phys. Rev. Lett.*, 77:4210, 1996.

[74] R. Shuker and R. Gammon. Raman-scattering selection-rule breaking and the density of states in amorphous materials. *Phys. Rev. Lett.*, 25:22, 1970.

[75] F.L. Galeener and P.N. Sen. Theory for the first-order vibrational spectra of disordered solids. *Phys. Rev. Lett.*, 17:1928, 1978.

[76] V.K. Malinovsky, V.N. Novikov, and A.P. Sokolov. Log-normal spectrum of low-energy vibrational excitations in glasses. *Phys. Lett. A*, 153:63, 1991.

[77] G. E. Walrafen, Y. C. Chu, and M. S. Hokmabadi. Raman spectroscopic investigation of irreversibly compacted vitreous silica. *J. Chem. Phys.*, 92:6987, 1990.

[78] A. P. Sokolov, U. Buchenau, W. Steffen, B. Frick, and A. Wischnewski. Comparison of Raman-and neutron-scattering data for glass-forming systems. *Phys. Rev. B*, 52:R9815, 1995.

[79] A. Fontana, R. DellÁnna, M. Montagna, F. Rossi, G. Viliani, G. Ruocco, M. Sampoli, U. Buchenau, A. Wischnewski. The Raman coupling function in amorphous silica and the nature of the long-wavelength excitations in disordered systems. *Europhys. Lett.*, 47:56, 1999.

[80] N.V. Surovtsev and A.P. Sokolov. Frequency behavior of Raman coupling coefficient in glasses. *Phys. Rev. B*, 66:054205, 2002.

[81] A. Fontana, F. Rossi, G. Viliani, S. Caponi, E. Fabiani, G. Baldi, G. Ruocco, and R. Dal Maschio. The Raman coupling function in disordered solids: A light and neutron scattering study on glasses of different fragility. *J. Phys.: Condens. Matter*, 19:205145, 2007.

[82] L. Orsingher, G. Baldi, A. Fontana, and F. Rossi. The Raman coupling function in permanently densified GeO_2 glasses. *Phil. Mag.*, 91:1857, 2011.

[83] C. Zha, R.J. Hemley, H. Mao, T.S. Duffy, and C. Meade. Acoustic velocities and refractive index of SiO_2 glass to 57.5 GPa by Brillouin scattering. *Phys. Rev. B*, 50:3907, 1994.

[84] T. Deschamps, C. Martinet, D.R. Neuville, D. de Ligny, C. Coussa-Simon, and B. Champagnon. Silica under hydrostatic pressure: A non continuous medium behavior. *J. Non-Cryst. Solids*, 355:2422, 2009.

[85] T. Scopigno, U. Balucani, G. Ruocco, and F. Sette. Density fluctuations in molten lithium: Inelastic x-ray scattering study. *J. Phys. Condens. Matter*, 12:8009, 2000.

[86] G. Monaco and V.M. Giordano. Breakdown of the Debye approximation for the acoustic modes with nanometric wavelengths in glasses. *Proc. Natl. Acad. Sci. USA*, 106:3659, 2009.

[87] D. Fioretto, S. Corezzi, S. Caponi, F. Scarponi, G. Monaco, A. Fontana, and L. Palmieri. Cauchy relation in relaxing liquids. *J. Chem. Phys.*, 128:214502, 2008.

[88] P.J. Schultz, K.G.Lynn. Theory of positrons in solids an on solid surfaces. *Rev. Mod. Phys.*, 66:1994, 1990.

[89] P.J. Schultz, K.G.Lynn. Interaction of positron beams with surfaces, thin films, and interfaces. *Rev. Mod. Phys.*, 60:701, 1988.

[90] R.A. Ferrel. Theory of positron annihilation in solids. *Rev. Mod. Phys.*, 28:308, 1956.

[91] S. Berko, F.L. Hereford. Experimental studies of positron interactions in solids and liquids. *Rev. Mod. Phys.*, 28:299, 1956.

[92] S. Sampath, C.J. Benmore, K.M. Lantzky, J. Neuefeind, K. Leinenweber, D.L. Price and J.L. Yarger. Intermediate-range order in permanently densified GeO_2 glass. *Phys. Rev. Lett.*, 90:115502, 2003.

[93] J. Blétry. Sphere and distance models for binary disordered systems. *Phil. Mag. B*, 62:469, 1990.

[94] P.J. Mohr, B.N. Taylor, and D.B. Newell. The 2010 CODATA Recommended Values of the Fundamental Physical Constants, 2011.

[95] S. Berko and H.N. Pendleton. Positronium. *Ann. Rev. Nucl. Part. Sci.*, 30:543, 1980.

[96] C. Hugenschmidt. Positron sources and positron beams. In A. Dupasquier, A.P. Mills jr. and R.S. Brusa, editor, *Proceedings of the International School of Physics Enrico Fermi - Course CLXXIV*. IOS Press, 2010.

[97] W. Egger, P. Sperr, G. Kögel, and G. Dollinger. Pulsed low energy positron system (PLEPS) at the Munich research reactor FRMII. *Phys. Stat. Sol.*, 4:3969, 2007.

[98] W. Egger. Pulsed low-energy positron beams in materials sciences. In A. Dupasquier, A.P. Mills jr. and R.S. Brusa, editor, *Proceedings of the International School of Physics Enrico Fermi - Course CLXXIV*. IOS Press, 2010.

[99] P. Kirkegaard, M. Eldrup. POSITRONFIT EXTENDED: a new version of a program for analysing positron lifetime spectra. *Comput. Phys. Commun.*, 7:401, 1974.

[100] Y. Sasaki, Y Nagai, H. Ohkubo, K. Inoue, Z. Tang, and M. Hasegawa. Positronium in silica-based glasses. *Rad. Phys. Chem.*, 68:569, 2003.

[101] R.S. Brusa, S. Mariazzi, L. Ravelli, P. Mazzoldi, G. Mattei, W. Egger, C. Hugenschmidt, B. Löwe, P. Pikart, C. Macchi, and A. Somoza. Study of defects in implanted silica glass by depth profiling positron annihilation spectroscopy. *Nucl. Instrum. Meth. B*, 268:3186, 2010.

[102] Y.C. Jean. Positron annihilation spectroscopy for chemical analysis: A novel probe for microstructural analysis of polymers. *Microchem. J.*, 42:72, 1990.

[103] S.J. Tao. Positronium annihilation in molecular substances. *J. Chem. Phys.*, 56:5499, 1972.

[104] M. Eldrup, D. Lightbody, and J.N. Sherwood. The temperature dependence of positron lifetimes in solid pivalic acid. *Chem. Phys.*, 63:52, 1981.

[105] D.W. Gidley, W.E. Frieze, T.L. Dull, A.F. Yee, E.T. Ryan, and H.M. Ho. Positronium annihilation in mesoporous thin films. *Phys. Rev. B*, 60:R5157, 1999.

[106] J.P. Rino, I. Ebbsjö, R.K. Kalia, A. Nakano, and P. Vashishta. Structure of rings in vitreous SiO_2. *Phys. Rev. B*, 47:3053, 1993.

[107] N.T. Nhan, P.K. Hung D.M. Nghiep, and H.S. Kim. Molecular dynamics investigation on microstructure and void in amorphous SiO_2. *Mat. Trans.*, 49:1212, 2008.

[108] A.B. Bhatia and T.E. Thornton. Structural aspects of the electrical resistivity of binary alloys. *Phys. Rev. B*, 2:3004, 1970.

[109] R.D. Shannon. Revised effective ionic radii and systematic studies of interatomic distances in halides and chalcogenides. *Acta. Cryst. A*, 32:751, 1976.

[110] G.S. Grest, S.R. Nagel, and A. Rahman. Zone boundaries in glasses. *Phys. Rev. B*, 29:5968, 1984.

[111] T. Scopigno, M. DÁstuto, M. Krisch, G. Ruocco, and F. Sette. Observation of Umklapp processes in noncrystalline materials. *Phys. Rev. B*, 64:012301, 2001.

[112] B. Ruzicka, T. Scopigno, S. Caponi, A. Fontana, O. Pilla, P. Giura, G. Monaco, E. Pontecorvo, G. Ruocco, and F. Sette. Evidence of anomalous

dispersion of the generalized sound velocity in glasses. *Phys. Rev. B*, 69:100201, 2004.

[113] G. Baldi, V. M. Giordano, G. Monaco, F. Sette, E. Fabiani, A. Fontana, and G. Ruocco. Thermal conductivity and terahertz vibrational dynamics of vitreous silica. *Phys. Rev. B*, 77:214309, 2008.

[114] A.I. Chumakov, A. Bosak, and R. Rüffer. Contribution of acoustic modes to the density of vibrational states measured by inelastic scattering techniques. *Phys. Rev. B*, 80:094303, 2009.

[115] A. Bosak, M. Krisch, I. Fischer, S. Huotari, and G. Monaco. Inelastic x-ray scattering from polycrystalline materials at low momentum transfer. *Phys. Rev. B*, 75:064106, 2007.

[116] G. Baldi, V.M. Giordano, G. Monaco, and B. Ruta. Sound attenuation at terahertz frequencies and the boson peak of vitreous silica. *Phys. Rev. Lett.*, 104:195501, 2010.

[117] G. Baldi, V.M. Giordano, and G. Monaco. Elastic anomalies at terahertz frequencies and excess density of vibrational states in silica glass. *Phys. Rev. B*, 83:174203, 2011.

[118] F. Léonforte, A. Tanguy, J.P. Wittmer, and J.L. Barrat. Inhomogeneous Elastic Response of Silica Glass. *Phys. Rev. Lett.*, 97:055501, 2006.

[119] F. Léonforte. Vibrational states and disorder in continuously compressed model glasses. *J. Non-Cryst. Solids*, 357:552, 2011.

[120] B. T. Kolomiets. Vitreous Semiconductors. *Phys. Stat. Sol.*, 7:359, 1964.

[121] A.L. Greer and N. Mathur. Materials science: Changing face of the chameleon. *Nature*, 437:1246, 2005.

[122] L. Orsingher, G. Baldi, A. Fontana, L. Bove, T. Unruh, A. Orecchini, N. Violini, C. Petrillo, and F. Sacchetti. High-frequency dynamics of vitreous $GeSe_2$. *Phys. Rev. B*, 82:115201, 2010.

[123] R.W. Johnson, S. Susman, J. McMillan, and K.J. Volin. Preparation and characterization of Si_xSe_{1-x} glasses and determination of the equilibrium phase diagram. *Mat. Res. Bull.*, 21:41, 1986.

[124] M. Tenhover, M.A. Hazle, and R.K. Grasselli. Atomic structure of SiS_2 and $SiSe_2$ Glasses. *Phys. Rev. Lett.*, 51:404, 1983.

[125] M. Tenhover, M.A. Hazle, R.K. Grasselli, and C.W. Thompson. Chemical bonding and the atomic structure of Si_xSe_{1-x} glasses. *Phys. Rev. B*, 28:4602, 1983.

[126] J.E. Griffiths, M. Malyj, G.P. Espinosa, and J.P. Remeika. Crystalline $SiSe_2$ and Si_xSe_{1-x} glasses: syntheses, glass formation, structure, phase separation and Raman spectra. *Phys. Rev. B*, 30:6978, 1984.

[127] L.F. Gladden and S.R. Eliott. Computer-generated models of a-$SiSe_2$: evidence for a glass exhibiting medium-range order. *Phys. Rev. Lett.*, 59:908, 1987.

[128] M. Arai, D.L. Price, S. Susman, K.J. Volin, and U. Walter. Network dynamics of chalcogenide glasses. II. Silicon diselenide. *Phys. Rev. B*, 37:4240, 1988.

[129] R.W. Johnson, D.L. Price, S.Susman, M. Arai, T.J. Morrison, and G.K. Shenoy. The structure of silicon-selenium glasses. I. Short-range order. *J. Non-Cryst. Solids*, 83:251, 1986.

[130] R. Bhadra, S. Susman, K.J. Volin, and M. Grimsditch. Elastic properties of Si_xSe_{1-x} glasses. *Phys. Rev. B*, 39:1378, 1989.

[131] A.J. Dianoux and G. Lander. Neutron Data Booklet, 2003.

[132] D. Aisa, S. Aisa, E. Babucci, F. Barocchi, A. Cunsolo, A. De Francesco, F. Formisano, T. Gahl, E. Guarini, A. Laloni, H. Mutka, A. Orecchini, C. Petrillo, W.C. Pilgrim, A. Piluso, F. Sacchetti, J.B. Suck, and G. Venturi. BRISP: A new thermal-neutron spectrometer for small-angle studies of disordered matter. *J. Non-Cryst. Solids*, 352:5130, 2006.

[133] Institut Laue Langevin. The Yellow Book 2005 - Guide to neutron research Facilities, 2005.

[134] Tobias Unruh, Jürgen Neuhaus, Winfried Petry. The high-resolution time-of-flight spectrometer TOFTOF. *Nucl. Instrum. Meth. A*, 580:1414, 2007.

[135] C. Petrillo and F. Sacchetti. Analysis of neutron diffraction data in the case of high-scattering cells. *Acta Crystallogr., Sect. A: Found. Crystallogr.*, 46:440, 1992.

[136] C. Petrillo and F. Sacchetti. Analysis of neutron diffraction data in the case of high-scattering cells. II. Complex cylindrical cells. *Acta Crystallogr., Sect. A: Found. Crystallogr.*, 48:508, 1992.

[137] C. Petrillo, F. Sacchetti, B. Dorner, J.B. Suck. High-resolution neutron scattering measurement of the dynamic structure factor of heavy water. *Phys Rev E*, 62:3611, 2000.

[138] M.J. Cooper and R. Nathans. The resolution function in neutron diffractometry. I. The resolution function of a neutron diffractometer and its application to phonon measurements. *Acta Cryst.*, 23:357, 1967.

[139] L.E. Bove, E. Fabiani, A. Fontana, F. Paoletti, C. Petrillo, O. Pilla, and I.C.V. Bento. Brillouin neutron scattering of v-GeO_2. *Europhys. Lett.*, 71:563, 2005.

[140] M. Sampoli, G. Ruocco, and F. Sette. Mixing of Longitudinal and Transverse Dynamics in Liquid Water. *Phys. Rev. Lett.*, 79:1678, 1997.